3/20/96

SANDIA REPORT

SAND92–0985 • UC–703
Unlimited Release
Printed February 1996

Measuring Hugoniot, Reshock and Release Properties of Natural Snow and Simulants

RECEIVED

APR 0 3 1996

O S T I

Michael D. Furnish, Mark B. Boslough

Approved for public release; distribution is unlimited.

SF2900Q(8-81)

MASTER

Measuring Hugoniot, Reshock and Release Properties of Natural Snow and Simulants

Michael D. Furnish and Mark B. Boslough
Experimental Impact Physics Department

Sandia National Laboratories

Albuquerque NM 87185

Abstract

We describe methods for measuring dynamical properties for underdense materials (e.g. snow) over a stress range of roughly 0.1 - 4 GPa. Particular material properties measured by the present methods include Hugoniot states, reshock states and release paths. The underdense materials may pose three primary experimental difficulties. Snow in particular is perishable; it can melt or sublime during storage, preparation and testing. Many of these materials are brittle and crushable; they cannot withstand such treatment as traditional machining or launch in a gun system. Finally, with increasing porosity the calculated Hugoniot density becomes rapidly more sensitive to errors in wave time-of-arrival measurements. A family of 36 impact tests was conducted on snow and six proposed snow simulants at Sandia, yielding reliable Hugoniot states, somewhat less reliable reshock states, and limited release property information. Natural snow of density ~0.5 gm/cm^3, a lightweight concrete of density ~0.7 gm/cm^3 and a "snow-matching grout" of density ~0.28 gm/cm^3 were the subjects of the majority of the tests. Hydrocode calculations using CTH were performed to elucidate sensitivities to edge effects as well as to assess the applicability of SESAME 2-state models to these materials. Simulations modeling snow as porous water provided good agreement for Hugoniot stresses to 1 GPa; a porous ice model was preferred for higher Hugoniot stresses. On the other hand, simulations of tests on snow, lightweight concrete and the snow-matching grout based on (respectively) porous ice, tuff and polyethylene showed a too-stiff response. Other methods for characterizing these materials are discussed. Based on the Hugoniot properties, the snow-matching grout appears to be a better snow simulant than does the lightweight concrete.

Acknowledgments

Table of Contents

Figures

Tables

Measuring Hugoniot, Reshock and Release Properties of Natural Snow and Simulants

1.0 Introduction

1.1 Motivation

Several problems of interest require a knowledge of the shock properties of natural snow. Consider the case of an airshock coupling into ground through a layer of snow. Figure 1-1 illustrates the situation for a normally incident airshock (plotted here as position vs. time).
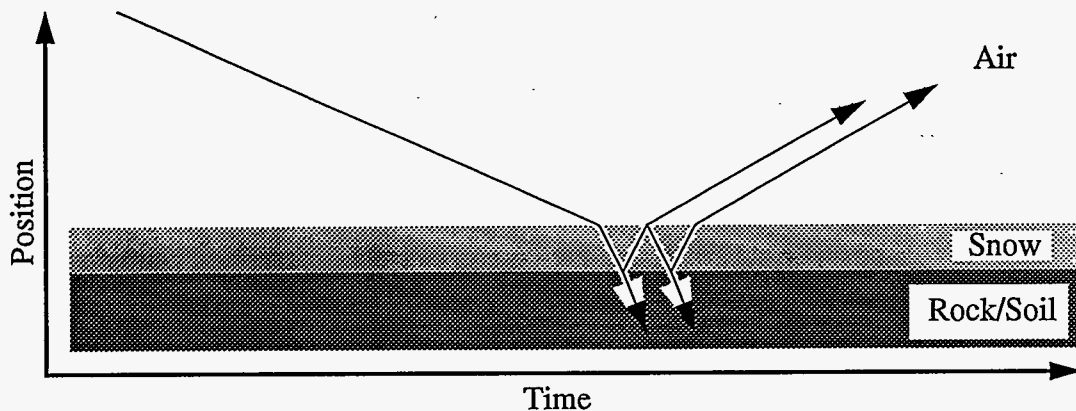
Figure 1-1. Time-position diagram of shock interactions (airshock impinging on snow cover over ground). A question to be answered by modeling studies is how the groundshock amplitude is affected by the snow layer.

A layer of snow is presumed to be capable of significantly perturbing airshock coupling to ground. The nature of this perturbation is to be determined by theoretical studies benchmarked by experimental data.

Similarly, a snowfield containing mines to discourage traversing may in principal be cleared by delivering an airshock sufficient to detonate the mines. A question is what the required airshock amplitude is, and how to deliver it.

The present study is designed to produce experimental data on natural snow to aid in benchmarking computational and thermodynamic models for use in calculations of shock interactions in snow. As well, it is designed to provide similar properties information for several materials under consideration as simulants of natural snow. Here, a "simulant" is a material chosen to provide mechanical responses to airshock similar to those provided by

natural snow, while avoiding the logistics problems of working with large amounts of natural snow in a controlled laboratory setting. Various candidate materials will be discussed later.

1.2 Previous and contemporaneous work

The present study provides data in an important intermediate-stress region (0.1 - 4 GPa) for snow and several simulants. Several complementary studies are mentioned for reference.

Bakanova et al. [1976] conducted several very-high stress tests on artificial snow of densities of 0.915, 0.60 and 0.35 gm/cm^3, using high-explosive drivers and electrical contact time measurement methods to measure Hugoniot states. The maximum Hugoniot stresses achieved were 50.3, 35.4 and 22.2 GPa (respectively), while minimum stresses were 3.4, 6.8 and 3.8 GPa (respectively).

Johnson et al. [1992, 1993] achieved low stresses (to 0.04 GPa) in snow of various densities with an eight-inch gas gun, instrumenting the sample with embedded carbon gauges. For this stress range, they found that (1) the Rankine-Hugoniot jump conditions, although not strictly applicable in this stress region, produced errors in calculated shock velocity of only 5 - 20%), and (2) there was little temperature or stress history dependence of the Hugoniot state of the sample, although there was significant rate dependence.

Work by Solie et al. [1994] and Erlich and Curran [1994] was performed contemporaneously with the present study. Solie et al. [1994] detonated sheet explosives at the surface of a snowpack (relatively dry; $\rho_0 \approx 0.25$ gm/cm^3) instrumented with carbon and PVDF gauges. They observed extremely high attenuation. Experimental difficulties included major corrections for the impedance mismatch between the gauges and the snow, giving large error bars for their inferred in-situ states (also a problem for Johnson et al. [1992, 1993]) and rapid attenuation (88% in 0.2 m for shock velocity). Adding a sheet to prevent entry of the blast gases into the snow increased the stress observed at 10 cm by a factor of two. Input stresses ranged to 0.9 GPa. Erlich and Curran [1994] combined yttrium stress gauges and particle velocity gauges to measure the response of artificial snow samples and highly porous grout samples (intended to be of identical material to those used in the present study) to a shock introduced by dilute explosives tiles (DET). Again, rapid attenuation was observed; for example, stresses decreased from 0.1 GPa to 0.025 GPa in 6 cm.

These studies taken together suggest that water snow gives rapid attenuation where impulsive loading provides stresses of ~0.1 GPa and that the Rankine-Hugoniot wave equations are of restricted value except at very high stress levels ($\geq$ 1 kb) or where a nonattenuating wave is indicated.

2.0 Experimental Technique

2.1 Basic description

Highly distended materials (such as snow and foams) require a specialized experimental geometry due to the large impedance mismatch existing between the sample and any adjacent components. Consider the configuration shown in Fig. 2-1 (see Appendix A for assembly details).

In most of the present experiments, a thick 6061-T6 aluminum impactor impacts the base
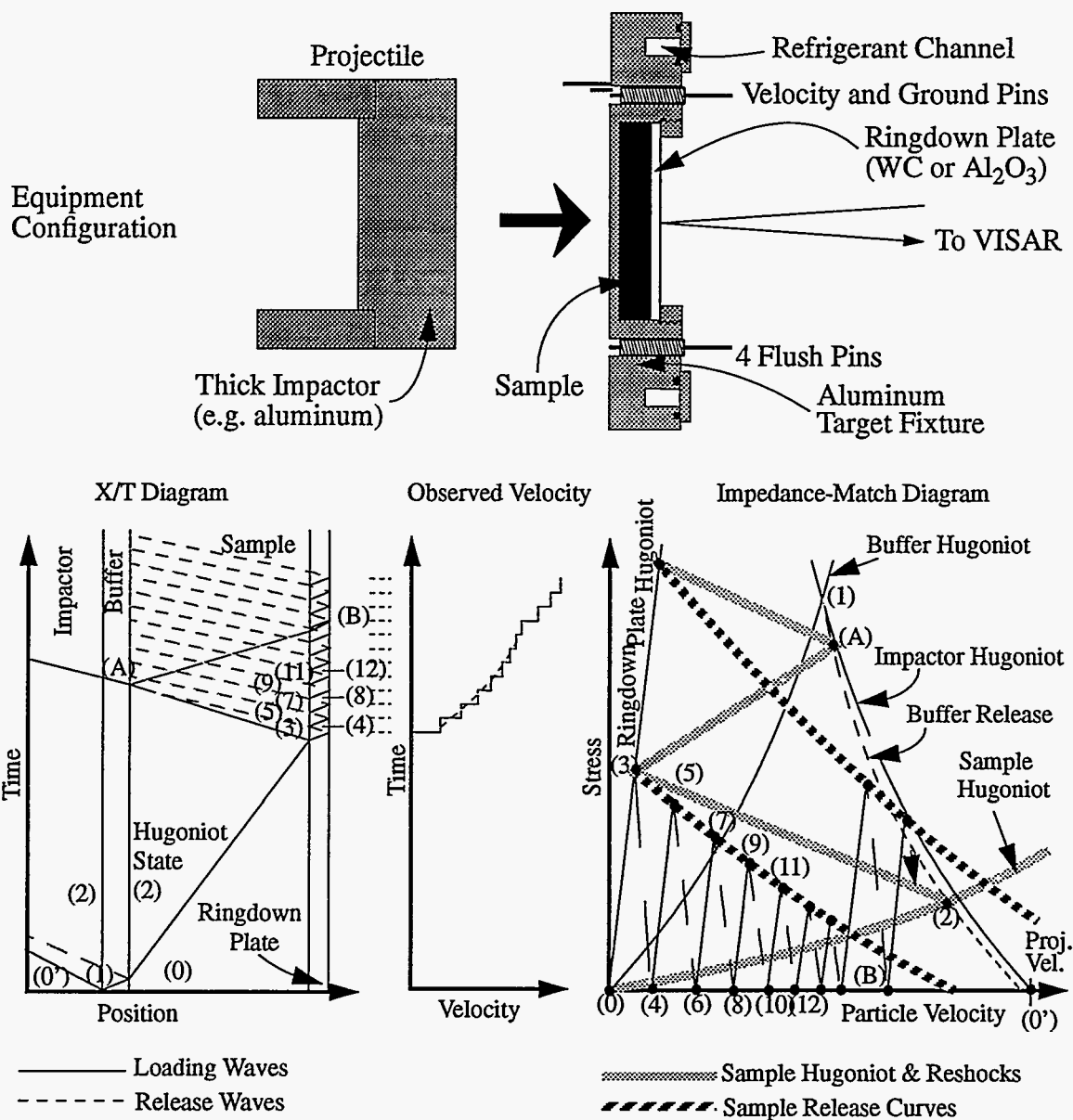
Figure 2-1. Ringdown Configuration (Gas gun adaptation shown)

of an aluminum (6061-T6) cup containing the sample. A shock is transmitted into the sample. This shock passes through the sample and into a thin tungsten carbide plate (the ringdown plate), which is bounded on the other side by a free surface. A reshock passes back into the sample because the tungsten carbide has a higher shock impedance than does the snow or simulant. The plate accelerates downrange (this may also be interpreted as a ringdown). As the plate accelerates, a release wave is sent back into the sample. Velocity interferometry (VISAR) [Barker and Hollenbach, 1972] measures the velocity of the free surface of the tungsten carbide plate. Observed free-surface velocities correspond to particle velocities for the states numbered $(4+2n)$ $(n = 0, 1, 2, ...)$ in Fig. 2-1. Wave profiles are timed relative to impact through the use of a fiducial generated by a flush pin. Corrections applied to this timing include impact planarity, relative travel times of the fiducial and the data from the target to the acquisition instrumentation, and elevation of the flush pin above the impact surface of the target. Details are presented in Appendix A.

Additional information may be gathered if the tests are instrumented with thin-film stress gauges such as PVDF (Polyvinylidene Difluoride) gauges. For the present materials, time-of-arrival of the shock at both sides of the sample is the principle benefit of such instrumentation. With more homogeneous materials, high-quality stress histories may be obtained as well. Appendix C presents a discussion of these issues as they pertain to the 13 tests in this series which used such instrumentation to compliment the VISAR.

It is worth discussing whether the propagating wave can be treated as steady. For experiments conducted with brief impulsive loading, it apparently cannot (see §1.2). The work of Johnson et al. [1992, 1993] suggested that gas gun results can be interpreted with only minor error as steady-wave. Since the present experiments were conducted at much higher stress levels than were theirs, the error should be yet less important. Therefore, in our analysis, we make the standard assumption that the compression wave is steady.

Equation-of-state information is deduced as follows. The impedance-match diagram in Figure 2-1 is intended as a reference for this discussion. Hugoniot states are determined from the shock transit time in the sample, which is calculated from the shock arrival time at the free surface. The Hugoniot state lies at the intercept of the buffer release curve and the line $\sigma = \rho_0 U_S U_P$. The reshocked stress of the sample is determined from the acceleration of the tungsten carbide plate after the initial ringing has damped. In an experiment with homogeneous samples the velocity increment to the first plateau in the observed velocity history provides the same information, but we have not found such an analysis to be of use with such heterogenous samples as snow, lightweight concretes and grouts. Finally, the stress-volume release trajectory of the sample from the reshock state may be determined from the acceleration history of the free surface according to Eq. 2.1.

$$\dot{P}_m = P_m \cdot \frac{\sqrt{-\left.\frac{\partial P}{\partial V}\right|_{P_M}}}{\sigma} \quad \text{where} \quad \ddot{x} = \frac{P_m(t)}{\rho_{RP} T_{RP}}$$

P_m = stress in sample at boundary with ringdown plate

$\rho_{RP} T_{RP}$ = areal density of ringdown plate = σ

V = specific volume of sample

t = time

(Eq. 2.1)

The ringdown plate is chosen as a high-impedance material exhibiting a simple wave structure in the stress region of interest. Tungsten carbide (<5% Co binder; density > 14.9 gm/cm^3) may be used at stresses up to about 4.5 GPa (its HEL). This material has a wave velocity of 7.05 km/s [D. J. Steinberg, personal communication]. Z-cut sapphire may be used up to about 12 GPa [Graham and Brooks, 1971].

For highly distended materials, the loading wave may be taken as a single wave. Multi-wave structures do not normally occur except at extremely low stress levels because the volume change is dominated by porosity collapse. Inhomogeneities in this process, however, may render the wave propagation unsteady at low to moderate stress levels.

If cooling is required, liquefied or cold gaseous nitrogen may be passed through the refrigerant channel or acetone chilled by dry ice may be used [Miller and Chhabildas, 1985]. Normally a thermostatic switch is required to avoid large temperature fluctuations. We have previously used these systems successfully in the ranges of -10°C, -40°C and -90°C [Miller and Chhabildas, 1985]. In the present study, the perishability of the sample requires target assembly in a cold room, storage in a freezer and transfer with dry ice in a cooler, as well as target cooling during the experiment.

Fractional uncertainties for the Hugoniot density have been shown by Holmes [1991, 1994] to be nearly proportional to $(\eta-1) \equiv (\rho_0/\rho - 1)$ times the fractional error in shock speed for large compressions. Other important errors are the initial density (which may vary from point to point on the sample) and errors in the release strength of the cup material.

This configuration bears close analogies to the ringdown configuration described by Chhabildas and Miller [1985] for measuring the release behavior of crystalline quartz. In their configuration, however, the sample was launched into the ringdown plate. The release measured was from a simple Hugoniot state. Unfortunately, their configuration required that the sample withstand exposure to vacuum, and hence could not be applied for the present study.

2.2 CTH simulations of experimental setup

These experiments were designed to provide a uniaxial strain environment to the sample for a finite period of time, after which the waves would inevitably be affected by waves propagating radially from the boundaries of the target fixture and the projectile (edge effects). In an attempt to estimate the role of these edge effects, we performed a series of one- and two-dimensional calculations with the multi-dimensional finite-element CTH wavecode [McGlaun et al., 1990]. A variety of combinations of zones sizes, dimensions, material strengths and material models were tried. In the present section we present those results pertinent to an evaluation of the experimental design.

A simplified geometry was used for the two-dimensional simulations, and is shown in Figure 2-2. Zone sizes were chosen as 0.4 mm (axial and radial dimension), allowing calculations to be run on HP workstations in approximately 30 minutes. One-dimensional simulations were performed with zone sizes of 0.4 and 0.044 mm.
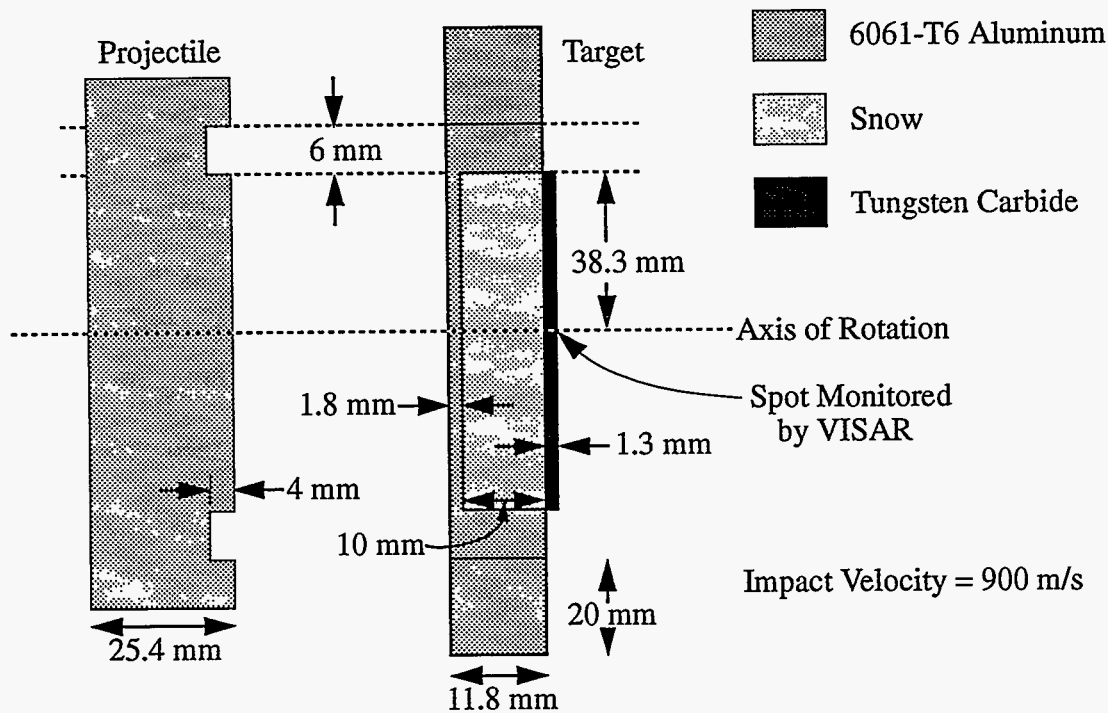
Figure 2-2. Simplified test configuration for two-dimensional CTH modeling of snow experiments.

The effects of inwardly-propagating radial waves on the waveform monitored by VISAR were determined in several ways. The following were calculated for comparison with the corresponding on-axis waveforms from the two-dimensional calculation: (1) a waveform calculated for 6 mm from the center; (2) a waveform calculated for a one-dimensional geometry; and (3) a waveform calculated for a geometry with a greatly extended lateral dimension (10×). The results of these calculations are shown in Figures 2-3 and 2-4.

All of these runs were performed modeling snow using a two-phase SESAME tabular model of water with porosity added. Dimensions and sample densities were chosen to agree with those for test SNW-2 (see §4); results will be compared with the experimental data in Section 5.

The results shown in Figures 2-3 and 2-4 suggest that edge effects do not influence the initial arrival time for test SNW-2 (at approximately 6 μs after impact). From 8 μs to 10.5 μs after impact, however, the two-dimensional calculations predict a VISAR velocity about 10% below that predicted by the one-dimensional calculations. At 10.5 to 11 μs, however, the 2-dimensional calculations predict surface accelerations remaining nearly constant, while the one-dimensional calculations predict a significant dropoff in acceleration. This is also the time at which the free surface velocity exceeds the projectile velocity.

Calculational zone sizes do not have a major effect on the wave profile except in the initial step structure, which is probably an artifact of the calculation.
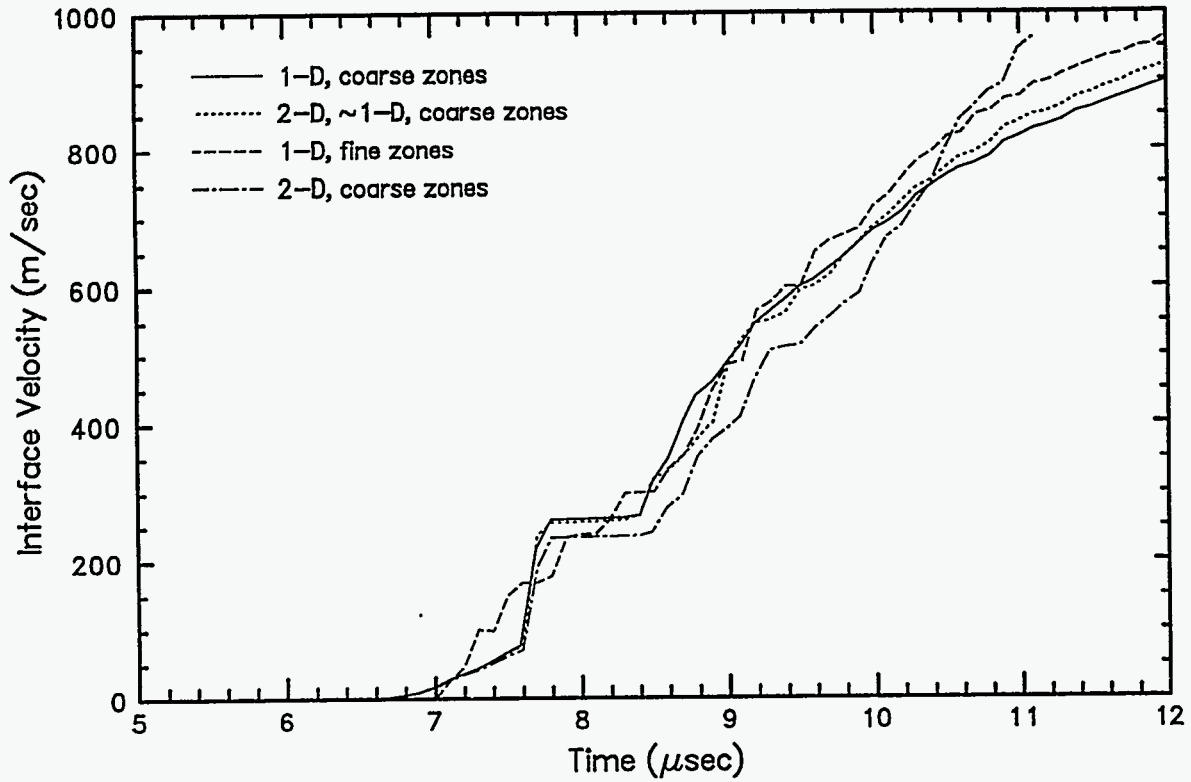
Figure 2-3. Sensitivity of CTH simulations to dimensionality (0.9 km/s, snow)
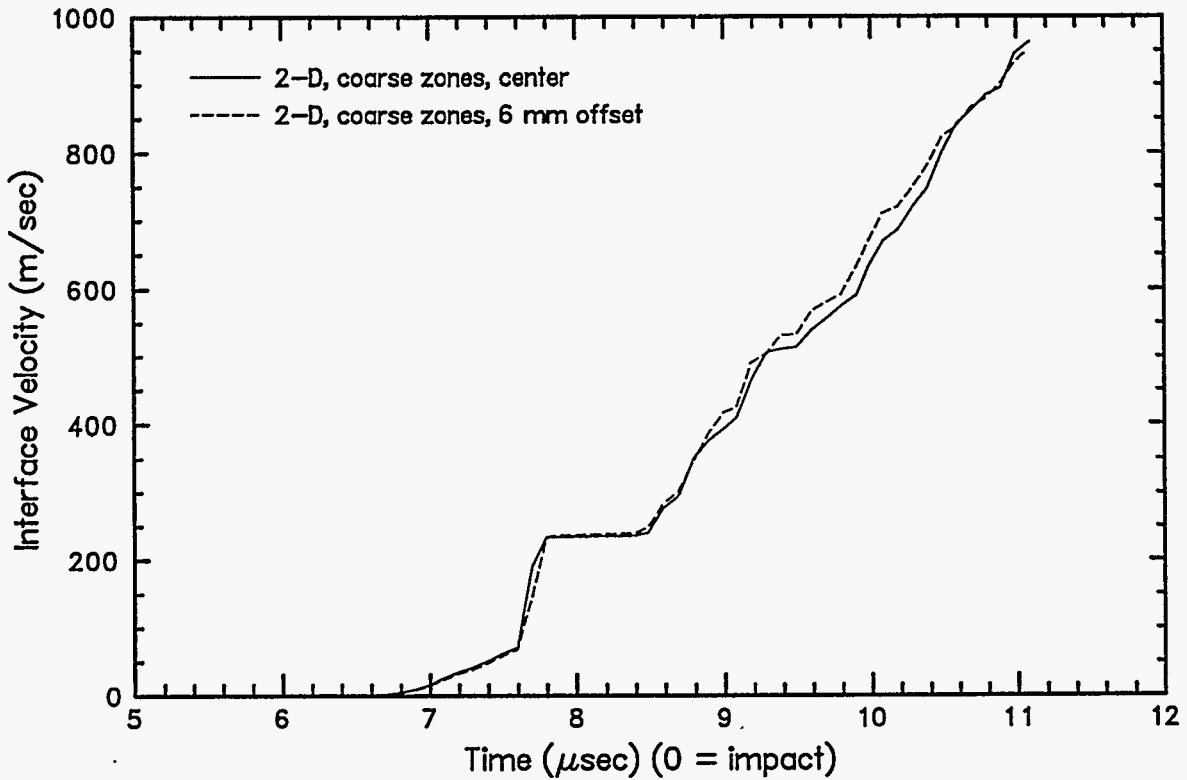
Figure 2-4. Sensitivity of 2-D CTH simulations to 6 mm displace-
ment of waveform sampling site from center (0.9 km/s, snow)

3.0 Nature of Samples

3.1 Collection and characterization of the snow

The portion of the present experiments performed on snow used natural snow collected at elevations of between 8,000 and 11,000 feet in the Sandia mountains adjacent to Albuquerque. These samples were collected in mid-morning on two days in February and March, under conditions of relatively dry air near freezing, from forested (shaded) areas which sloped gently to the north. The snow collected was granular and somewhat recrystallized. Densities were measured as 0.21 - 0.25 gm/cm^3 at collection time.

Densities were measured by weighing a sheet metal container of approximately 6 liter capacity (cookie tin) with and without unpacked snow. The snow was gently poured into the container, then levelled with a meter stick, prior to weighing. A spring-based kitchen scale was used for weight measurement, with calibration checks interleaved with sample weighings. The scale was found to be accurate to ±0.5 ounce (0.6%) under field conditions.

Snow for samples was gently placed in a large plastic bag lining a picnic cooler, flanked with dry ice chunks wrapped in newspaper, and transported to environmental test chambers at Sandia which were held at -40°C. Vibration during transportation was minimized, as were transportation delays. The distance between the collection site and the Sandia facilities was approximately 30 km over good road.

Aging effects were minimized by storing the snow at -40°C in airtight bags. Nonetheless, aging effects are inevitable, and we note Mellor's [1975] statement that "there is no {other} material of engineering significance that displays the bewildering complexities of snow." The time interval between sample collection and testing was significant, ranging up to seven months for the final snow tests. Reassuringly, densities and gross textures of the snow were similar through all of the impact testing series, so the tests can be reasonably interpreted as representing the behavior of a consistent material.

Final characterization was done during target loading. The textures observed are shown in Figure 3-1. Typical grains are millimeter sized and angular. Shapes in some cases suggest constructive metamorphosis, perhaps including hopper growth, although careful morphological analyses were not conducted. No intergranular binding was found. Densities ranged from 0.49 to 0.51 gm/cm^3, representing a significant increase over the collection density of 0.3 - 0.4 gm/cm^3. How much of this compaction occurred during sample collection and transportation and how much occurred during storage is unclear.

It is unlikely that the present results depended on details of the structure of the snow inasmuch as stress levels significantly above the yield strength were imposed. Hence these results may be compared with those of tests using artificial snow, such as those of Erlich and Curran [1994] and Bakanova [1976].

Figure 3-1. Photograph of snow used in present experiments. Fine divisions on scale are mm. Ruler was flipped to allow scale to be photographed clearly.

3.2 Characterization of the non-snow samples

A variety of snow simulants were tested in the present program. These were selected by the Defense Nuclear Agency on the basis of criteria including the following:

- Density similar to that of common varieties of natural snows (this was actually not a very restrictive condition),
- Porosity similar to that of common varieties of natural snows,
- Consistency and repeatability,
- Cost (applicable for constructing larger testbeds); and
- Non flammability.

A total of six simulant candidates were selected for evaluation (two impact tests). Two of these simulants were selected for further study. Brief descriptions of these simulant candidates follow. The three letter abbreviations in capital letters correspond to the test names in Section 4.

Kaowool (KAW) is an expanded aluminosilicate manufactured by Thermal Ceramics Corp, with a density approximately 0.22 - 0.25 gm/cm^3. It is generally used as a refractor ceramic insulator. The composition is 42% Al_2O_3, 56% SiO_2 and 2% other.

Fibrex FBX 2300 ceramic fiber block (FIB) is mostly vitreous mineral wool, with minor amounts of starch, ball clay and ceramic fiber. It has a density of approximately 0.23 gm/cm^3.

17   Nature of Samples
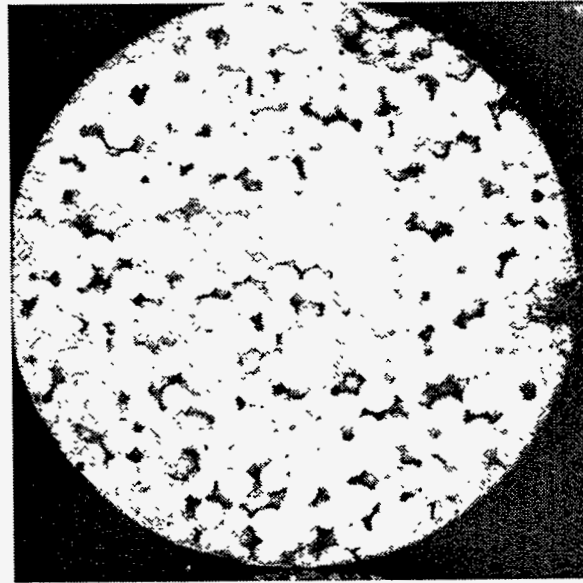
Figure 3-2. Photograph of snow-matching grout
II (SGR) sample. Sample diameter was 7.5 cm.

Snow-matching grout I (SMG) was fabricated at the Army Corps of Engineers Waterways Experiment Station (WES). It is uniform, although very weak, fine-grained grout composed of 42 wt% Hydrostone Super "X" (a gypsum cement), 35 wt% Eccospheres "R" (5 - 120 μm glass microspheres, with 1.75 mm walls, composed of 70% SiO_2, 25% Na_2O and 5% B_2O_3), 13 wt% foam (WF-304 foam concentrate) and 10 wt% water [J. Boa, personal communication]. Densities of this material were measured as 0.192 gm/cm^3, measured on a cast cylinder.

Temperlite 1200^0 (TEM), by Innova, is primarily composed of "mineral silicates", with up to 5% amorphous silica, up to 0.5% polyester fiber, <1% silicon oil and <0.1% crystalline quartz. It has a density of approximately 0.21 gm/cm^3.

Snow-matching grout II (SGR), also fabricated by WES, is much stronger than snow-matching grout I, although distinctly more heterogeneous. It is composed of polystyrene spheres 1 - 5 mm in diameter encased in a thin crust of Portland cement mixed with glass microspheres. A typical sample is shown in Figure 3-2.

A lightweight concrete (LWC), manufactured locally by Jewel Industries, is physically a concrete including Portland cement, perlite and water. The precise recipe is proprietary. Voids (bubbles) are a difficulty with this material, and samples must be visually inspected to minimize the likelihood of a major void in the central regions. Figure 3-3 presents a poor sample of lightweight concrete (excessive bubbles).

Other materials considered were excluded on bases of cost (aerogel), flammability (polystyrene foams) or other criteria.

Nature of Samples   18
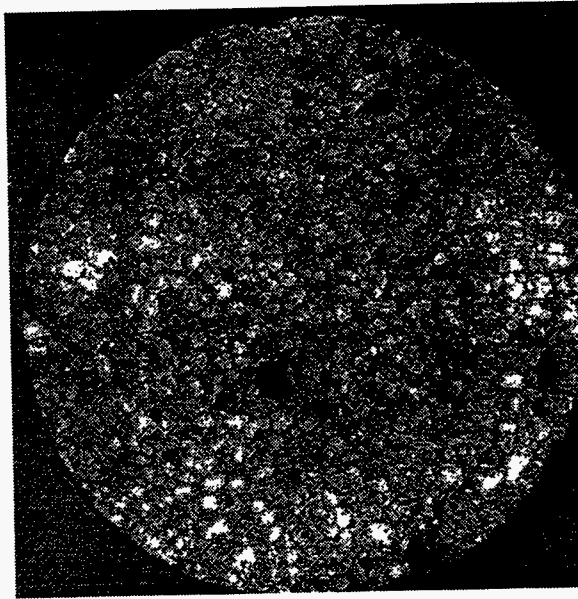
Figure 3-3. Photograph of lightweight concrete
(LWC) sample. Sample diameter was 7.5 cm.

4.0 Experimental Results

4.1 Parameters of experiments

A total of 36 successful impact tests were conducted in this program, including 14 on the 4" compressed gas gun system at the Sandia STAR Facility, 11 at the 89 mm powder gun system, also at the STAR Facility, and 11 in the Building 808 64 mm compressed gas gun system. Tests were initially divided between the two STAR Facility gun systems based on required impact velocity. The Building 808 gun system was added to the project when it became apparent PVDF instrumentation could be more readily employed there for certain tests. The pertinent capabilities of the three gun facilities used are outlined in Table 4.1.

Table 4.1: Gun facility capabilities.			
Gun System	Compressed Gas	Powder	Compressed Gas
Site	STAR	STAR	Building 808
Bore Diameter (mm)	101.6	89	64
Minimum Velocity	~0	~0.4	~0
Maximum Velocity (km/s)	1.0	2.3	1.3
Handles Cryogenic Tgts?	Y	Y	Y
VISAR*	A/GPP	G/GPP	GPP
PVDF Instrumentation	No	Not for present series	Yes
Timing‡	Fid/FPs	Fid/FPs	PVDF
* A = Air delay leg; G= Conventional Glass-etalon, GPP = glass-etalon Push/Pull ‡Timing methods: Fid/FPs = via fiducial and flush pins; PVDF = via PVDF gauges			

The series proceeded as follows. An initial scoping series of two tests per sample was performed on the six simulant materials and on natural snow, with nominal impact velocities of 600 and 900 m/s. These tests utilized the STAR compressed gas gun. Next, three tests were performed on each of two preferred simulants (lightweight concrete and the second version of the snow matching grout) and on natural snow utilizing the STAR powder gun at higher impact velocities. Then three tests each were performed on these same three materials with the Building 808 compressed gas gun, utilizing both VISAR and PVDF stress sensors. Four additional tests completed the series: two on the second version of the snow matching grout on the powder gun and two on Kel-F on the Building 808 compressed gas gun. Kel-F, a polymer very close in shock properties to the PVDF sensors, was tested to provide a verification of the expected operation of the test configuration.

A detailed matrix of the tests conducted at the STAR Facility is presented in Table 4.2, and of the tests conducted at the Building 808 Facility, in Table 4.3.

The primary data obtained from the STAR Facility tests (gas gun and powder gun) were velocity profiles timed relative to impact. The time-of-arrival data allowed the calculation of the Hugoniot, while the slope of the velocity profile allowed the calculation of the reshock and release paths.

<td colspan="12" align="center">**Table 4.2 Snow and simulant tests at the STAR Facility**</td>
Test Name	Gun Facility	Impact Velocity km/s	Flyer Thick. mm	Cup Thick. mm	Sample ID	Sample Density gm/cm³	Sample Space Thick.[1] mm	Sample Thick.[2] mm	WC Thick. mm	VPF m/s	Comments
KAW-1a	Gas	0.610	30.0	1.991	Kaowool	0.2411	10.049		1.274	71.67335	Replacement. for KAW-1
KAW-2	Gas	0.5801	25.4?	1.879	Kaowool	0.2511	9.528		1.300	71.67335	Dat2, BIM lost
FIB-1	Gas	0.602	30.0	2.002	Fibrex	0.2308	9.824		1.305	71.67335	
FIB-2	Gas	1.026	25.4	1.960	Fibrex	0.2248	9.831		1.315	71.67335	Dat1 lost
SMG-1	Gas	0.609	30.0	1.993	Snow-Match Grout 1		9.485		1.293	71.67335	V. Friable sample
SMG-2	Gas	0.9038	25.4	1.982	Snow-Match Grout 1		9.484		1.302	71.67335	V. Friable sample
TEM-1a	Gas	0.622	30.0	2.010	Temperlite	0.2106	10.024		1.286	71.67335	Replacement. for TEM-1
TEM-2	Gas	0.9175	25.4	2.007	Temperlite	0.2144	10.025		1.298	71.67335	
LWC-1	Gas	0.598	30.0	1.946	Lightweight Concrete	0.767	9.946	9.958	1.290	71.67335	ρ from unconfined vol.
LWC-2	Gas	0.972	25.4	1.9704	Lightweight Concrete	0.749	9.9812	9.994	1.290	71.67335	ρ from unconfined vol.
LWC-3	Pwd	1.232	25.35	2.301	Lightweight Concrete	0.761	9.999	10.001	1.307	139.37877	
LWC-4	Pwd	1.653	25.331	2.260	Lightweight Concrete	0.734	9.989	9.990	1.330	139.37877	
LWC-5	Pwd	2.126	12.689	2.236	Lightweight Concrete	0.772	9.999	9.999	1.359	139.37877	
SGR-1	Gas	0.595	30.0	1.985	Snow-Match Grout 2	0.228		10.668	1.281	71.67335	
SGR-2	Gas	0.910	25.4	1.991	Snow-Match Grout 2	0.236		10.241	1.284	71.67335	
SGR-3	Pwd	1.230	25.09	2.229	Snow-Match Grout 2	0.244	9.995	9.952	1.3666	139.37877	
SGR-4	Pwd	1.620	18.892	2.238	Snow-Match Grout 2	0.257	10.006	9.944	1.341	139.37877	
SGR-5	Pwd	2.170	12.670	2.251	Snow-Match Grout 2	0.231	9.985	9.940	1.366	139.37877	
SGR-11	Pwd	1.453	25.336	2.223	Snow-Match Grout 2	0.201	10.014	9.896	1.340	139.37877	
SGR-12	Pwd	1.918	22.169	2.008	Snow-Match Grout 2	0.250	10.096	9.880	1.317	139.37877	
SNW-1	Gas	0.6063	30.0	1.802	Snow	0.51	9.983		1.286	71.67335	-18°C was warmest; ~4 hrs
SNW-2	Gas	0.8994	25.4	1.869	Snow	0.51	9.981		1.284	71.67335	15 min -6°C; 94 min -23°C (-13°C in cooler)
SNW-3	Pwd	1.218	25.33	2.010	Snow	~0.51	10.062		1.3214	139.37877	-9°C cooler; -30°C tgt
SNW-4	Pwd	1.636	18.933?	1.931	Snow	~0.51	10.007		1.351	139.37877	-18°C = warmest; -26 - -36 (4 hrs)
SNW-5	Pwd	2.155	12.493	1.926	Snow	~0.51	10.060		1.369	139.37877	

1. Depth of sample compartment in target. Sample may be very slightly compressed to fit into this volume.
2. Thickness of sample (unconfined)

Table 4.3 Snow and simulant tests at the Building 808 Facility						
Test Name	Impact Velocity km/s	Sample ID	Sample Density gm/cm^3	Sample Thick.[1] mm	WC Thick. mm	Comments
LWC-6	0.413	Lightweight Concrete	0.76	5.03	1.37	
LWC-7	0.793	Lightweight Concrete	0.79	5.02	1.37	
LWC-8	1.244	Lightweight Concrete	0.82	5.02	1.37	
SGR-6	0.412	Snow Match Grout II	0.273	6.36	1.31	No VISAR data
SGR-7	0.796	Snow Match Grout II	0.274	6.35	1.37	No VISAR data
SGR-8	1.239	Snow Match Grout II	0.274	6.34	1.37	No input PVDF data
SGR-9	0.818	Snow Match Grout II	0.236	6.96	1.35	
SGR-10	0.404	Snow Match Grout II	0.238	6.96	1.36	
SNW-6	0.407	Snow	0.47	5.85	1.37	
SNW-7	0.756	Snow	0.47	5.84	1.36	
SNW-8	1.199	Snow	0.47	5.86	1.35	
KEL-1	0.410	Kel-F	2.122	4.808	1.344	X-cut quartz flyer
and driver (6.342 and 4.727 mm, resp.) Sample thick includes 0.038 mm gauge pkg.						
KEL-2	1.200	Kel-F	2.122	4.696	~1.34	X-cut quartz flyer
and driver (6.359 and 4.722 mm, resp.) WC probably pushed past 40 kb yield						

1. Thickness of sample (unconfined) for lightweight concrete and snow match grout II tests; depth of sample cup for snow tests

For the Building 808 gas gun tests, PVDF stress sensors were emplaced on the surfaces of the sample, as shown in Figure 4-1. Due to the locally heterogeneous nature of these samples, the gauges did not provide quantitative stress data. They were useful, however, for providing timing information which could be related to the VISAR velocity histories. For more detail, see Appendix C.
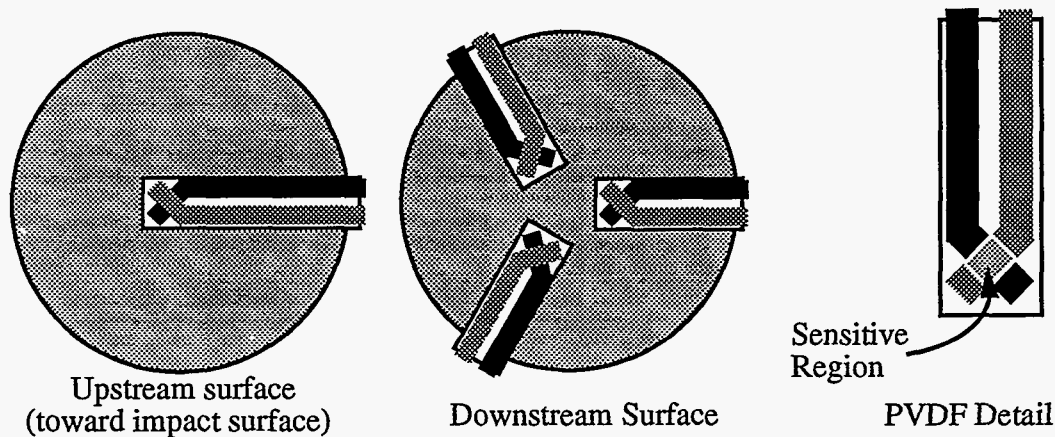

Upstream surface
(toward impact surface)　　　Downstream Surface　　　PVDF Detail

Figure 4-1. PVDF stress gauge configuration for Building 808 tests. Leads and associated electronics not shown for clarity.

4.2 Observed waveforms

In the present section waveforms are presented with general interpretation. Detailed test-by-test interpretation for many of these tests may be found in Appendix B. For ease of comparison between the waveforms acquired at the STAR Facility and those acquired at the Building 808 gas gun facility, timing is relative to shock entry into sample for Figures 4-2 through 4-8. This is because the 808 tests were timed relative to input PVDF stress gauges at the sample/cup interface. Wave profiles from tests conducted at the STAR Facility have been translated according to Table 4.4 (shifts are toward negative time).

Table 4.4. Time shifts used in plots of velocity histories for STAR tests to account for aluminum transit time

Test	Al Transit (μs)	Test	Al Transit (μs)	Test	Al Transit (μs)
SNW 1	0.3120	SGR 1	0.3441	LWC 1	0.3398
SNW 2	0.3129	SGR 2	0.3330	LWC 2	0.3272
SNW 3	0.3249	SGR 3	0.3599	LWC 3	0.3714
SNW 4	0.2986	SGR 4	0.3467	LWC 4	0.3489
SNW 5	0.2827	SGR 5	0.3299	LWC 5	0.3291
		SGR 11	0.3505		
		SGR 12	0.3018		

Results for natural snow (SNW) are presented in Figures 4-2 and 4-3. Figures 4-4 and 4-5 present wave profiles for lightweight concrete (LWC), and Figures 4-6 and 4-7, for the second version of the snow-matching grout (snow-matching grout II, or SGR). Finally, Figure 4-8 presents the wave profiles for Kel-F.

In addition, three other materials were tested at 600 m/s and 900 m/s impact velocities and monitored with VISAR. The waveforms observed in these tests are presented in Figures 4-9 and 4-10, together with the corresponding waveforms for snow, lightweight concrete and snow-matching grout II. Due to data acquisition system malfunctions, the timing of traces for fibrex (900 m/s) and kaowool (earlier 600 m/s trace) should be considered tentative.

Several fairly general observations can be made upon an inspection of these velocity profiles. First, with the exception of Kel-F, they do not present clean, consistent steps in velocity. Such steps are caused when a single shock is input to the tungsten carbide ringdown plate, allowing wave interactions as shown in Figure 2-1. Many profiles do exhibit some steps, such as SNW5 and 8, LWC2, 3, 5, and 7, Kaowool, and the snow-matching grout I (not II). The lack of more consistent, well-defined steps is likely a consequence of the nonuniformity of these materials. Snow-matching grout II, in particular, is nonuniform on a scale of 3 - 5 mm; this material presents almost no step structure. The Kel-F test material, on the other hand, is quite uniform and does show a very well-developed step structure which will be seen later to be quite consistent with computational results.
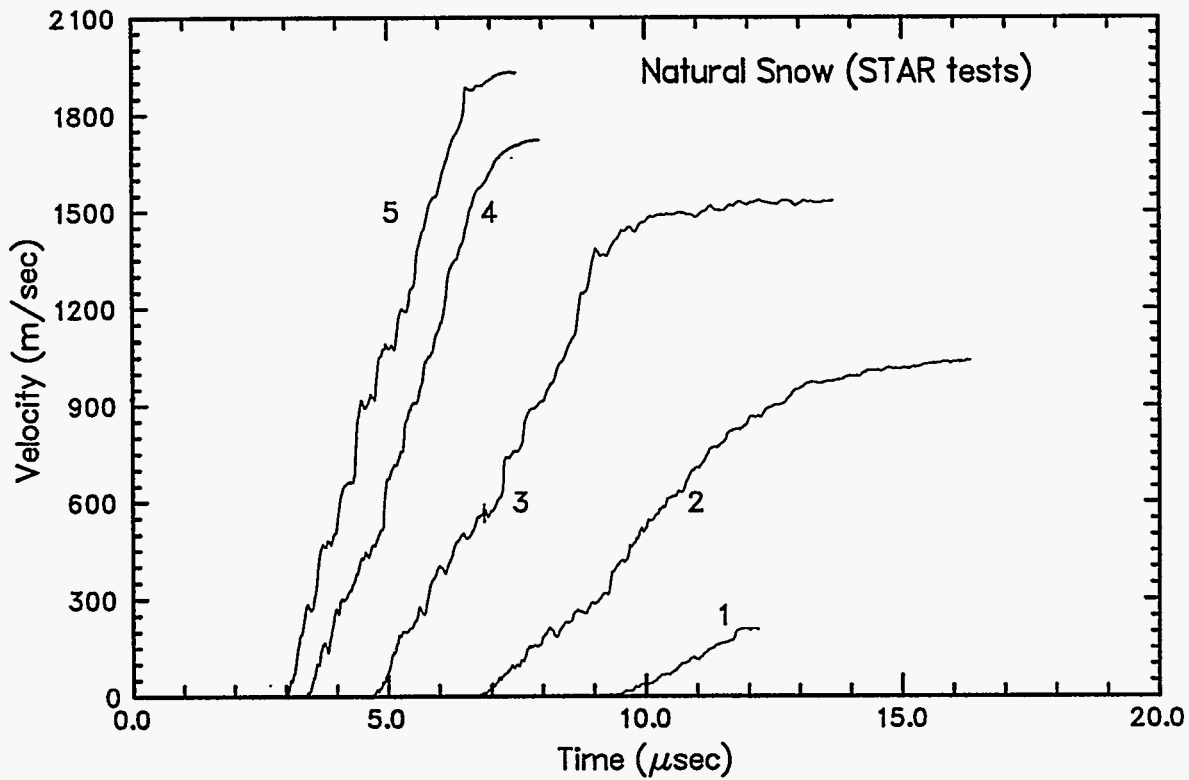
Figure 4-2. Velocity profiles for natural snow, from tests conducted at the STAR Facility. Zero time corresponds to shock entry into sample.
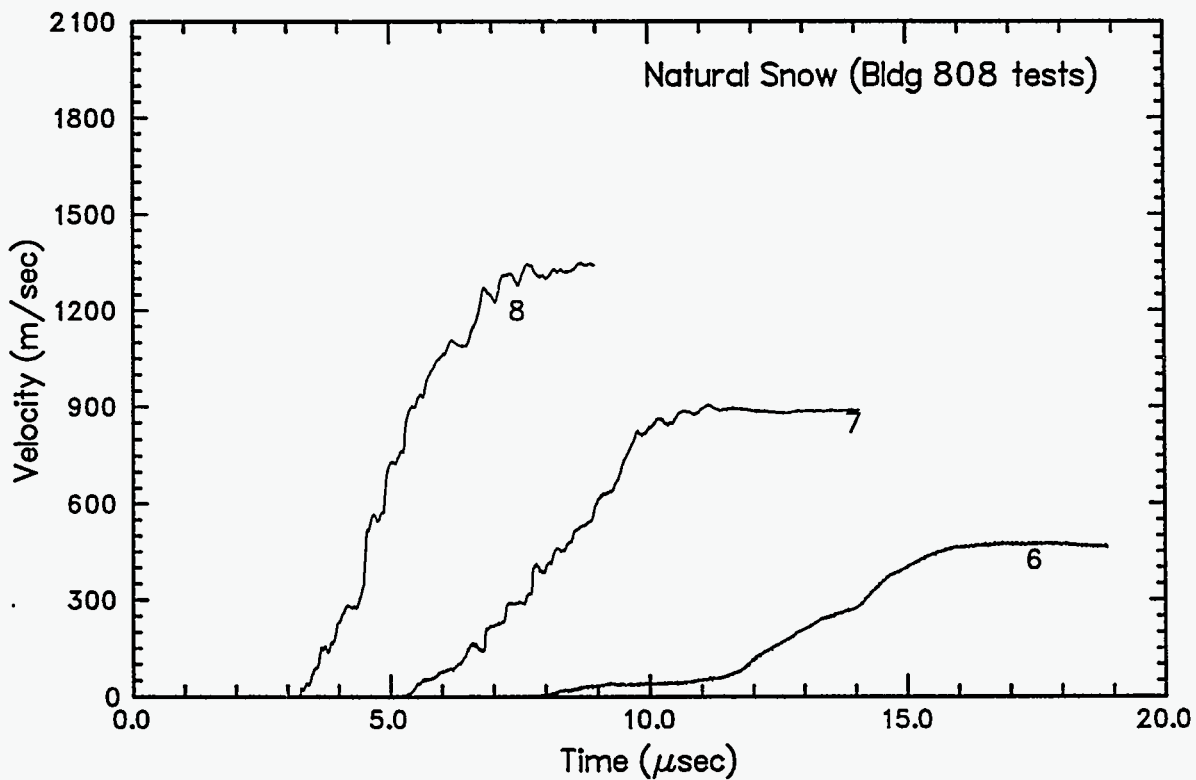
Figure 4-3. Velocity profiles for natural snow, from tests conducted at the Building 808 gas gun facility. Zero time corresponds to shock entry into sample.

Experimental Results   24
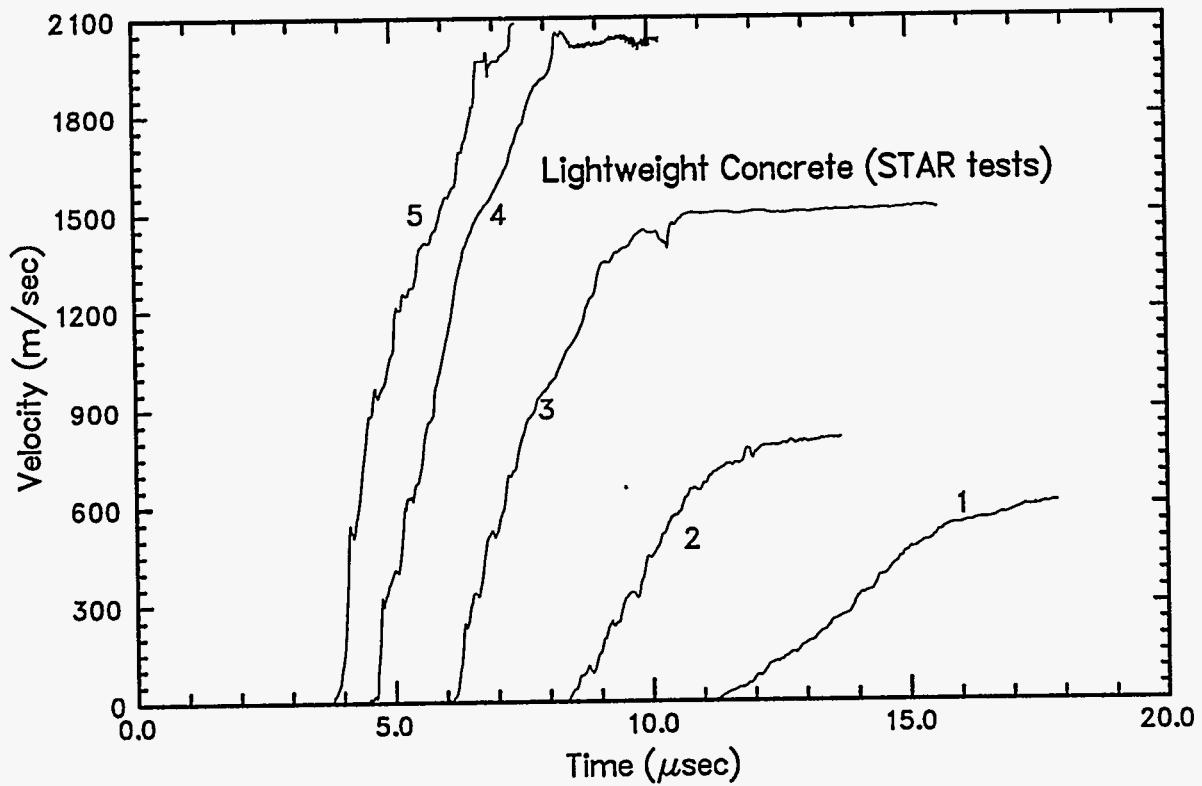
Figure 4-4. Velocity profiles for lightweight concrete, from tests conducted at the STAR Facility. Zero time corresponds to shock entry into sample.
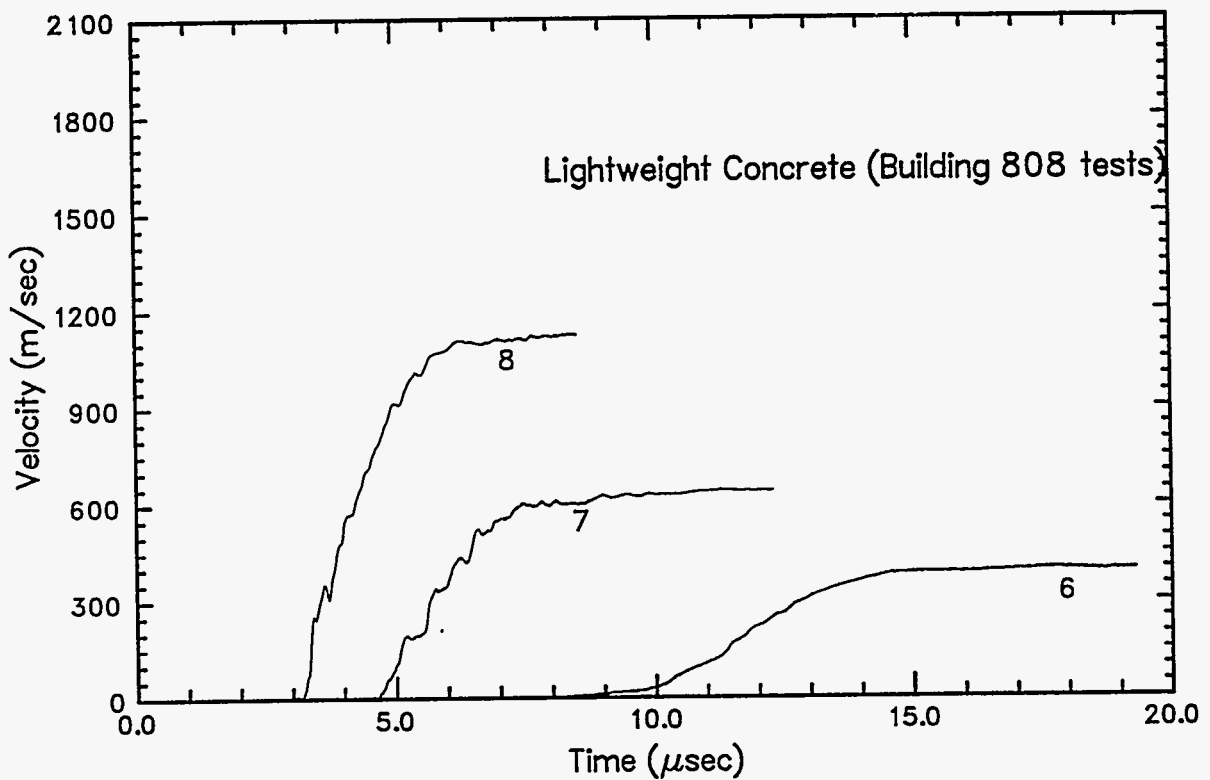
Figure 4-5. Velocity profiles for lightweight concrete, from tests conducted at the Building 808 gas gun facility. Zero time corresponds to shock entry into sample.

Experimental Results
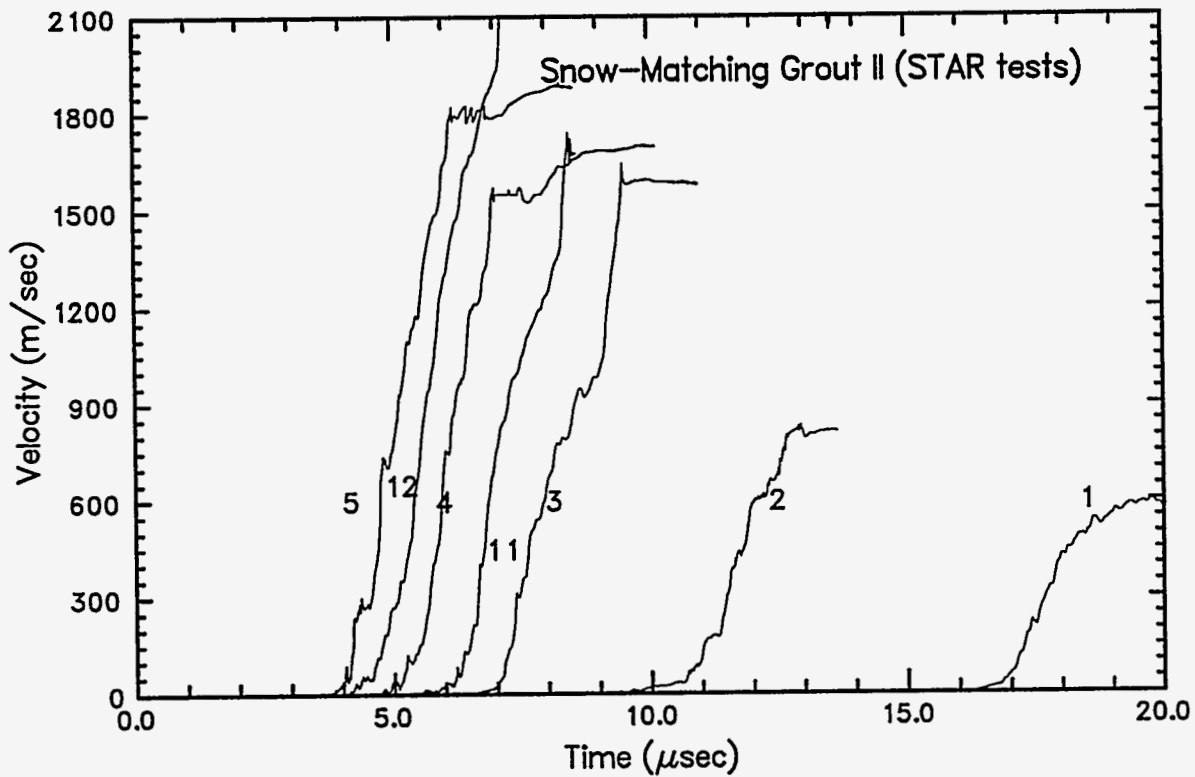
Figure 4-6. Velocity profiles for snow-matching grout II, from tests conducted at the STAR Facility. Zero time corresponds to shock entry into sample.
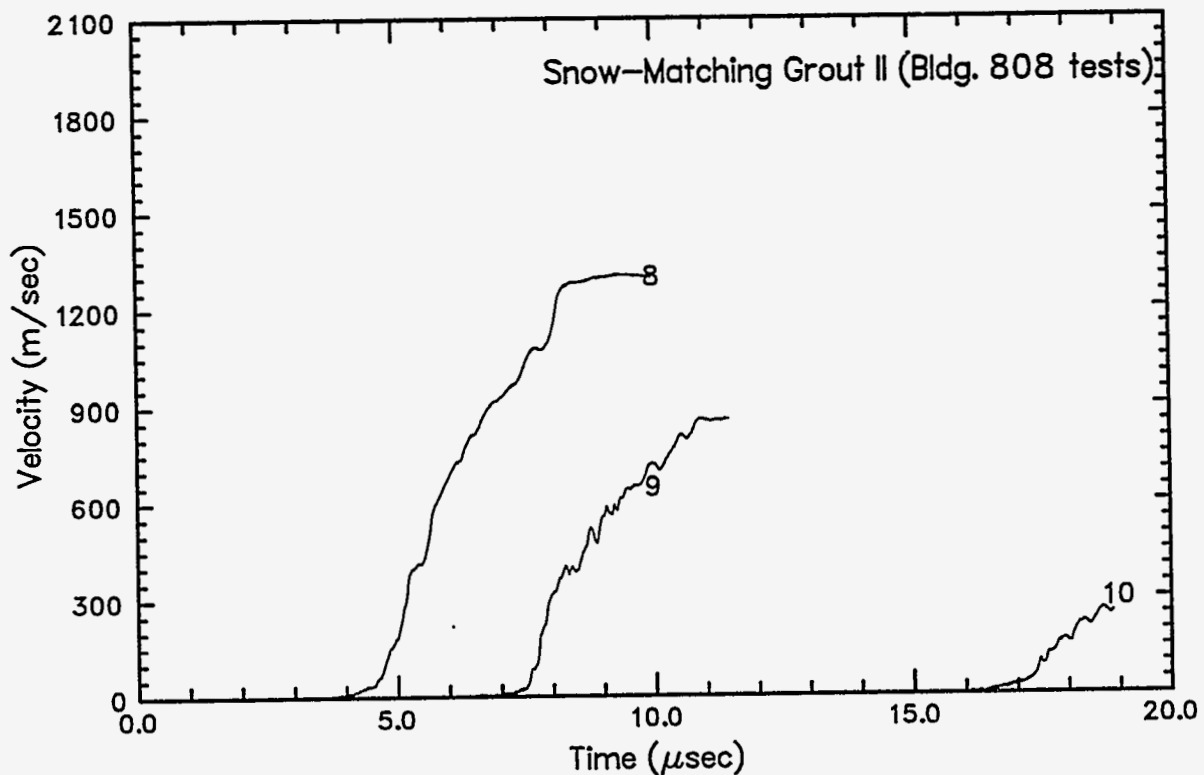
Figure 4-7. Velocity profiles for snow-matching grout II, from tests conducted at the Building 808 gas gun facility. Zero time corresponds to shock entry into sample.
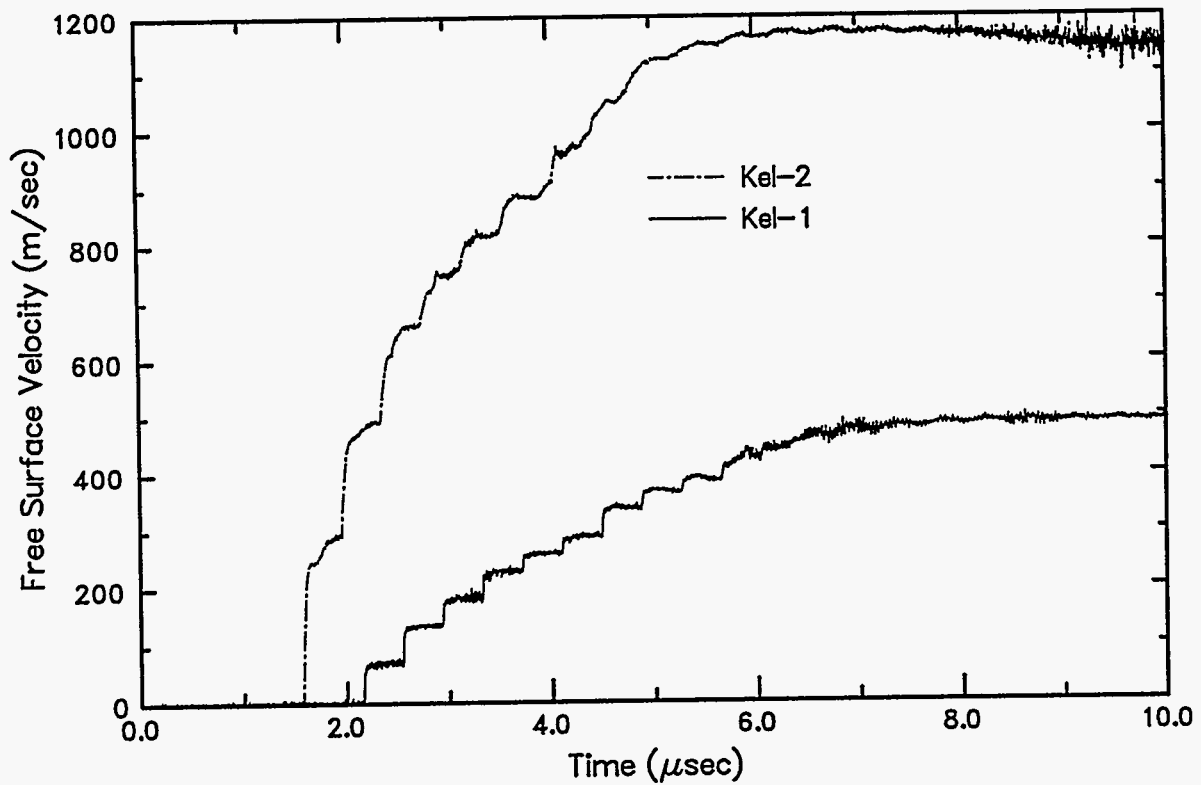
Figure 4-8. Velocity profiles for Kel-F test shots, from tests conducted at the Building 808 gas gun facility. Zero time corresponds to shock entry into sample.
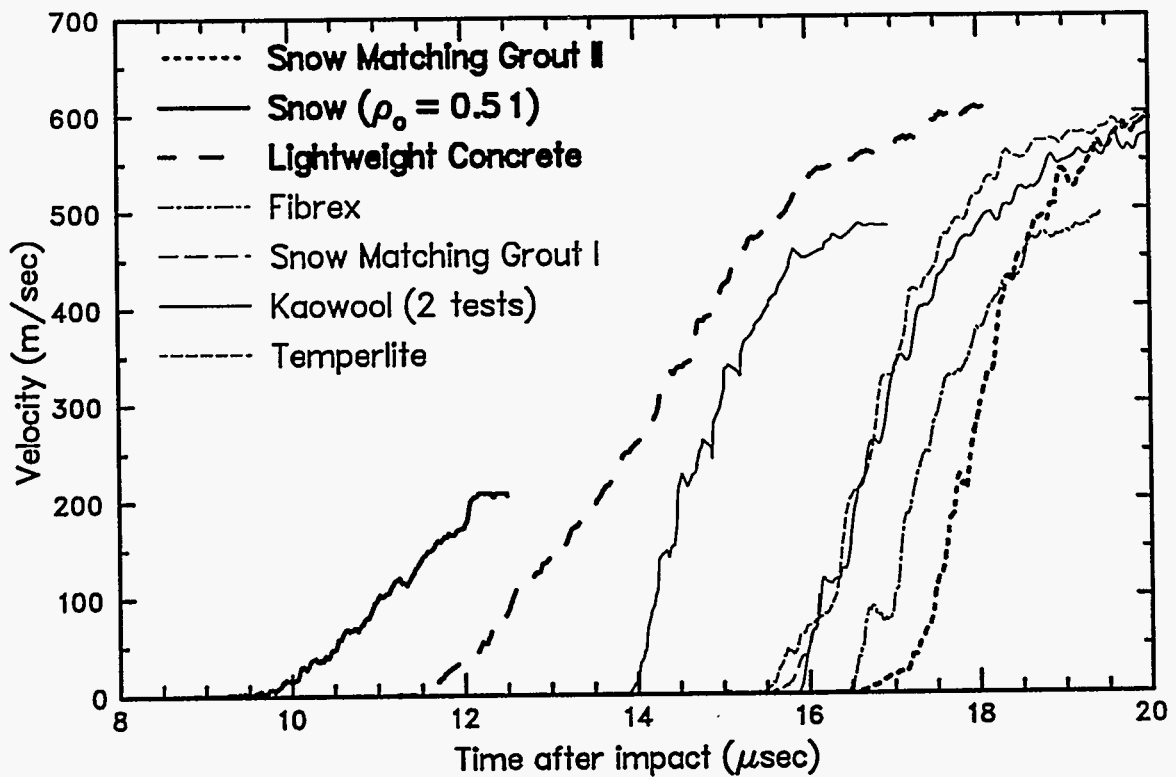

Figure 4-9. Velocity profiles for ~600 m/sec impacts, from tests conducted at the STAR Facility. Note that zero time corresponds to *impact* in this plot.
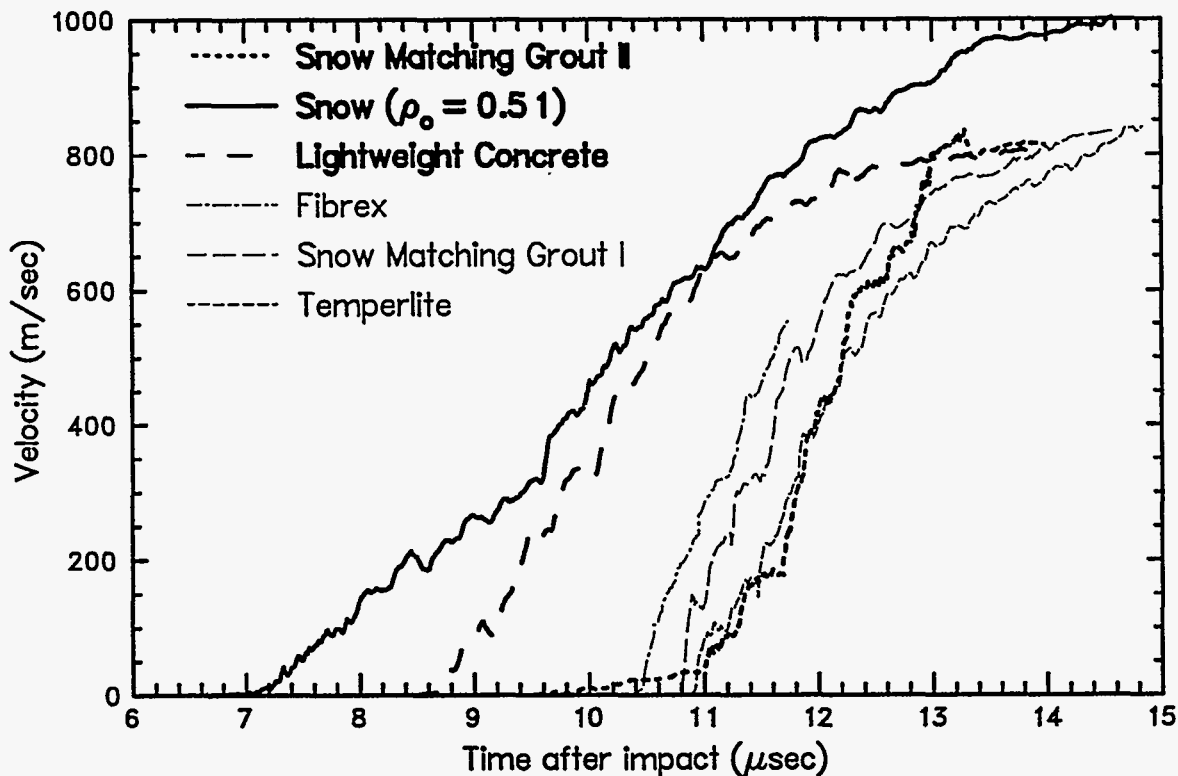
Figure 4-10. Velocity profiles for ~900 m/sec impacts, from tests conducted at the STAR Facility. Note that zero time corresponds to *impact* in this plot.

Velocity histories for the tests on natural snow show a rise of relatively constant slope. By contrast, those for lightweight concrete and snow matching grout II show a gradually decreasing slope. The lightweight concrete shows a far more dispersive unloading signature than do the other two materials, indicating a concave-upward release in pressure-density or pressure-volume space.

The velocity histories for snow matching grout II also tend to exhibit a toe. There are several possible explanations for this. A few examples are: (1) Local non-planarities in the shock cause a slowing of the primary shock; (2) A shock propagating through the gas precedes the primary shock; and (3) An elastic phenomenon is occurring in the toe.

The Building 808 gas gun facility tests tend to show a more marked leveling-off than do the STAR Facility tests for the natural snow and the lightweight concrete. This is likely an artifact of what might be considered a flaw in the experimental design. For those tests, the laser beam is delivered to the target by fiber-optics, and conducted to the VISAR similarly. The clamping fixture for the optical head is only about 1 - 1.5 mm from the free surface of the tungsten carbide except in the central region; this introduces another element to the system after the free surface has moved 1 - 1.5 mm. The calculated translation of the free surface is consistent with this explanation for these test results.

Historically, the collections of traces shown in Figures 4-9 and 4-10 were acquired first, with the intent of facilitating a selection of likely snow simulants for further study. Selec-

tion criteria were not limited to shock loading behavior alone, but also included vaporization properties under high shock conditions (blowoff), flammability properties, cost (a reason aerogel was not considered) and handling properties.

From these two figures (4-9 and 4-10), we see that arrival times tend to correlate well with initial distension; i.e. that more porous materials gave arrivals closer to the zero-density sample times of 17.2 μs (600 m/s impact, 10 mm thick sample) or 11.6 μs (900 m/s impact). This is consistent with a snowplow model of shock propagation for these materials, and will be treated more quantitatively below for the three materials selected for further study.

Perhaps the cleanest step structures among these waveforms are exhibited by the snow matching grout I. This material was relatively uniform and possessed very little strength. The profiles showed no evidence of the toe so pronounced for snow-matching grout II.

In the course of this study, snow-matching grout I was excluded on the basis of handling properties. Its friability make handling it difficult; it was cut by bandsaw to rough thickness while still in the PVC casting tubes, then carved to the proper diameter with a sharp razor blade. Small gaps at the edges of the sample chamber were filled with powder resulting from the cutting process. (The authors improved a machinist's day by writing a set of shape and tolerance specifications for samples of this material, then opening a casting tube of this material at the machine shop, to find only powder inside.)

4.3 Information from arrival: Hugoniot state calculation

Hugoniot states were calculated using the impedance-match method of Section 2.1 (see Figure 2-1). This calculation requires the shock transit time across the sample (total transit time less transit times across the ringdown plate and the aluminum cup, if applicable), the initial sample density, the projectile velocity and the shock properties of the impactor plate, the cup and the ringdown plate. The 6061-T6 aluminum used for the impactor and the cup was described by: $C_0 = 5.37$ km/s, $S = 1.34$, and $\rho_0 = 2.6978$ gm/cm^3. The tungsten carbide ringdown plate was described by $C_0 = 7.05$ km/s, $S = 0$, and $\rho_0 = 14.9$ gm/cm^3. Hence the only information actually acquired during the shot required here is the projectile velocity and the time of initial acceleration of the ringdown plate free surface.

The resulting states are shown in Table 4.5 and plotted in Figures 4-11 and 4-12. Fit curves included in these figure are based on linear U_S/U_P fits as detailed in the figure, and are valid over approximately $0.4 \leq U_P \leq 2.0$ k/s.

It should be emphasized that these calculations were made under the assumption of steady wave propagation. This may not be a valid assumption for these materials under the present stress regime. In fact, the snow-matching grout II and the lightweight concrete show an apparently unphysical dependence of density on stress for Hugoniot stresses below 1 GPa (lower stress gives higher density). This is an indication that steady wave propagation may not be occurring for these two materials at these stress levels. At higher stress levels, the Hugoniot densities of all three materials are seen to be consistent with the nondistended materials (0.9 gm/cm^3 for the grout, 1.0 gm/cm^3 for the snow, and 2.75 gm/cm^3 for the lightweight concrete).

Table 4.5. Hugoniot properties for snow, lightweight concrete and snow-matching grout II*

Test Number	Impact Vel. km/s	Initial Density gm/cm^3	Time-of Arrival μs	Hugoniot Stress GPa	Hugoniot Density gm/cm^3	Hugoniot Particle km/s	Hugoniot Shock km/s	ρ/ρ_0
Star Facility Tests								
SNW1	0.606(7)	0.51(4)	9.40(10)	0.33(3)	1.05(8)	0.577(6)	1.121(12)	2.06(3)
SNW2	0.899(9)	0.51(4)	7.05(3)	0.66(5)	1.15(9)	0.848(1)	1.523(7)	2.26(3)
SNW3	1.218(8)	0.51(4)	5.05(5)	1.27(9)	1.04(8)	1.127(9)	2.217(24)	2.03(3)
SNW4	1.636(17)	0.51(4)	3.70(5)	2.35(17)	0.97(7)	1.477(22)	3.12(5)	1.90(4)
SNW5	2.155(20)	0.51(4)	3.32(3)	3.48(25)	1.12(8)	1.929(23)	3.54(4)	2.20(4)
SGR1	0.595	0.23(1)	16.60(5)	0.088(4)	1.86(9)	0.582(0)	0.664(2)	8.15(19)
SGR2	0.910(5)	0.24(1)	9.8(2)	0.23(1)	1.21(14)	0.888(5)	1.103(24)	5.13(54)
SGR3	1.230	0.24(1)	6.94(4)	0.45(2)	1.04(5)	1.194(1)	1.558(11)	4.27(11)
SGR4	1.620(10)	0.26(1)	5.16(9)	0.86(4)	0.93(6)	1.56(1)	2.15(4)	3.63(22)
SGR5	2.170(2)	0.23(1)	4.07(3)	1.35(6)	0.90(4)	2.081(5)	2.80(3)	3.90(12)
SGR11	1.453(5)	0.20(1)	5.98(8)	0.52(3)	0.86(10)	1.413(5)	1.84(5)	4.30(47)
SGR12	1.918(6)	0.25(1)	4.36(7)	1.17(6)	0.90(8)	1.838(7)	2.55(7)	3.6(3)
LWC1	0.598	0.77(3)	11.53(4)	0.392(14)	2.04(7)	0.564(1)	0.905(4)	2.66(2)
LWC2	0.972	0.75(3)	8.67(5)	0.834(31)	2.91(11)	0.909(2)	1.225(8)	3.88(8)
LWC3	1.232(2)	0.76(3)	6.45(6)	1.46(5)	2.27(9)	1.129(5)	1.697(17)	2.99(7)
LWC4	1.653(3)	0.73(3)	4.85(5)	2.52(10)	2.04(8)	1.483(7)	2.319(27)	2.77(7)
LWC5	2.126	0.77(3)	4.10(3)	4.02(14)	2.32(8)	1.866(9)	2.794(23)	3.01(6)
Building 808 Gas Gun Facility Tests								
SNW6	0.407	0.47(4)	7.84(9)	0.14(1)	0.96(8)	0.390(1)	0.765(9)	2.04(3)
SNW7	0.756	0.47(4)	5.28(5)	0.39(3)	1.27(10)	0.723(2)	1.148(11)	2.70(5)
SNW8	1.199	0.47(4)	3.25(5)	1.01(8)	1.14(9)	1.125(5)	1.917(3)	2.42(6)
SGR10	0.404	0.24(1)	16.11(23)	0.041(2)	2.42(38)	0.394(0)	0.437(6)	10.2(1.6)
SGR9	0.818	0.24(1)	7.09(25)	0.19(1)	1.13(19)	0.799(0)	1.008(35)	4.8(8)
SGR8	1.239	0.27(1)	3.85(20)	0.57(3)	0.88(13)	1.195(2)	1.73(9)	3.2(5)
LWC6	0.413	0.76(3)	8.11(24)	0.190(9)	1.99(13)	0.393(1)	0.63(2)	2.62(14)
LWC7	0.793	0.79(3)	4.64(3)	0.661(24)	2.30(8)	0.742(1)	1.128(7)	2.92(4)
LWC8	1.244	0.82(3)	3.20(3)	1.55(5)	2.56(10)	1.135(3)	1.669(16)	3.12(8)
KEL1	0.410	2.122	2.008	1.766	2.408	0.315	2.646	1.134

*Values in parentheses denote the uncertainties in the last 1 - 2 digits of the quantity
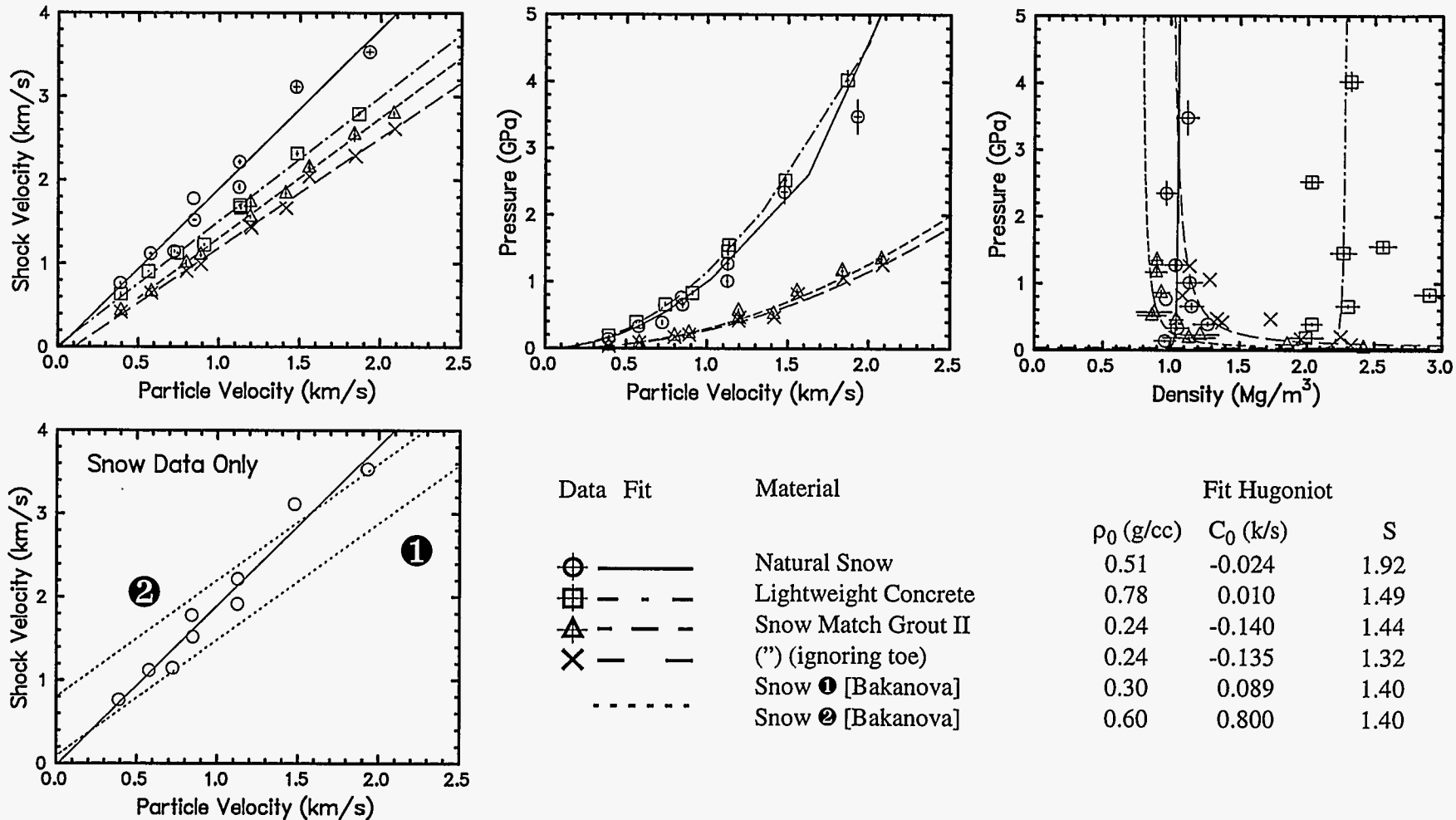
Figure 4-11. Hugoniot states for natural snow, lightweight concrete and snow-matching grout II.
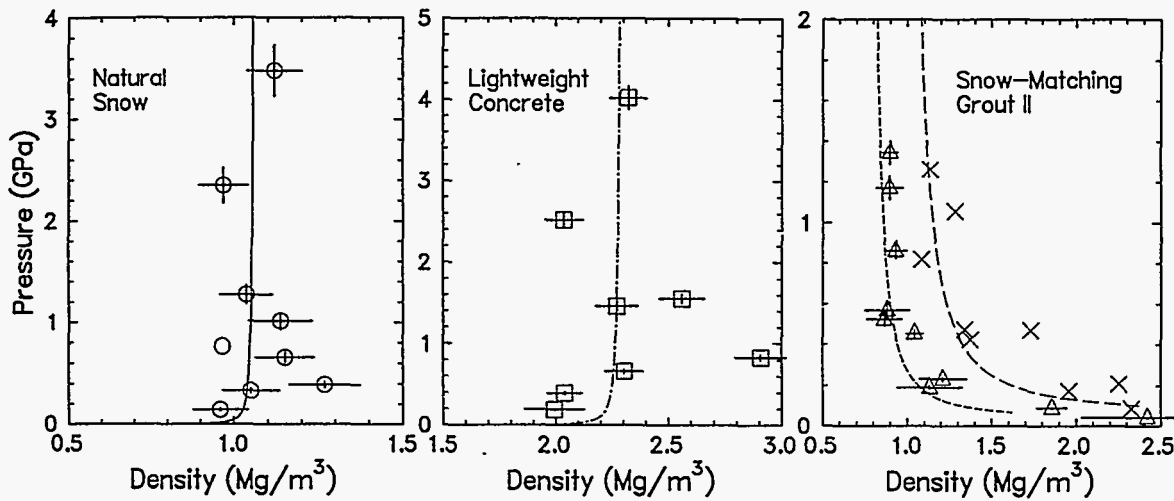
Figure 4-12. Detail of Hugoniot data and fits in pressure-density space.

4.4 Post-arrival information: Reshock, release

The discussion in Section 2.1 outlined two methods for extracting information from wave profiles generated using the present configuration. To recapitulate, the first is useful if discrete steps are observed in the profile, corresponding to the free surface velocity states (4), (6), (8), ... in Figure 2-1. The second is useful if these steps are "smeared out," as in the present study, and uses a variation of $F = ma$ to determine the reshock stress, specifically:

$$P_{Reshock} = \Psi_{RP} \times A_{FreeSurface} \quad \text{where}$$

$P_{Reshock}$ = Reshock Pressure
Ψ_{RP} = Areal density of ringdown plate
$A_{Free\ Surface}$ = Acceleration at free surface

(Eq. 4.1)

The reshock states have been calculated using this method, and are listed in Table 4.6 together with the input parameters used. It should be kept in mind that the primary quantity in this derivation is stress, with the other quantities derived from it. The Hugoniot and reshock states are plotted in pressure/density space in Figure 4-12.

This data set appears to be physically credible, but extremely noisy. There is no easily identifiable trend in the Figure 4-13 plots, which ideally would show a smoothly increasing density with stress. The general magnitudes of the density are correct (1 - 1.5 gm/cm^3 for snow, ~1 gm/cm^3 for most of the snow-matching grout tests, and 2.3 - 3.2 gm/cm^3 for most of the lightweight concrete tests). This is related to the sensitivity of calculated density to several factors: (1) the steady wave assumption (for initial shock as well as reshock), (2) the assumption that edge effects are not significant in the time interval over which the profile slope is measured, (3) the slope measurement itself, and (4) the uncertainties in the Hugoniot state. For such heterogeneous, porous materials, this noisiness is not surprising.

The second-from-last column of Table 4.6 refers to the height of the first "step" which would be found on the velocity profile for a uniform material with this reshock stress delivering a clean single shock to the ringdown plate. For certain tests with fairly well-

Table 4.6. Reshock states for snow, lightweight concrete and snow-matching grout II[1]

Test Number	Initial Density gm/cm^3	Time-of Arrival μs	Profile Slope $mm/\mu s^2$	Reshock σ GPa	Reshock ρ gm/cm^3	Reshock U_P km/s	Reshock U_S km/s	Reshock ρ/ρ_0	Inferred Step[2] $mm/\mu s$	Observed Step[3] $mm/\mu s$
Star Facility Tests
SNW1	0.51	9.40	0.086	1.65	1.40	0.56	2.24	2.75	0.031	0.16
SNW2	0.51	7.05	0.170	3.25	1.64	0.82	2.76	3.21	0.062	0.20
SNW3	0.51	5.05	0.280	5.51	1.45	1.07	3.80	2.83	0.105	0.21
SNW4	0.51	3.70	0.463	9.31	1.32	1.39	5.18	2.60	0.177	0.15
SNW5	0.51	3.32	0.564	11.51	2.08	1.82	3.94	4.08	0.219	0.28
SGR1	0.23	16.60	0.379	7.23	1.99	0.51	7.49	8.74	0.138	0.22
SGR2	0.24	9.8	0.512	9.79	1.32	0.79	9.92	5.58	0.186	0.17
SGR3	0.24	6.94	0.521	10.61	1.19	1.09	8.91	4.87	0.202	0.30
SGR4	0.26	5.16	1.040	20.77	1.02	1.36	15.68	3.98	0.395	0.10
SGR5	0.23	4.07	0.833	16.96	1.14	1.92	9.04	4.95	0.323	0.30
SGR11	0.20	5.98	0.402	8.03	1.09	1.34	6.49	5.41	0.153	0.21?
SGR12	0.25	4.36	0.510	10.01	1.29	1.74	5.66	5.18	0.191	0.35?
LWC1	0.77	11.53	0.128	2.47	2.82	0.54	1.88	3.73	0.047	0.08?
LWC2	0.75	8.67	0.294	5.64	5.21	0.86	1.93	6.96	0.107	0.10
LWC3	0.76	6.45	0.511	9.95	3.18	1.03	3.61	4.18	0.189	0.24?
LWC4	0.73	4.85	0.686	13.89	3.02	1.35	4.13	4.12	0.265	0.31
LWC5	0.77	4.10	0.709	14.36	7.07	1.73	2.57	9.15	0.273	0.52
Building 808 Gas Gun Facility Tests
SNW6	0.47	7.84	0.103	2.10	1.03	0.37	5.52	2.19	0.040	0.04
SNW7	0.47	5.28	0.247	5.01	1.45	0.67	5.39	3.09	0.095	0.15?
SNW8	0.47	3.25	0.467	9.39	1.33	1.04	7.11	2.83	0.179	0.15
SGR8	0.27	3.85	0.494	10.08	0.99	1.10	9.81	3.62	0.192	0.19?
SGR9	0.24	7.09	0.712	14.32	1.18	0.66	18.8	4.98	0.273	0.08?
SGR10	0.24	16.11	0.425	8.62	2.49	0.31	11.36	10.45	0.164	0.09
LWC6	0.76	8.11	0.097	1.97	2.36	0.37	2.39	3.11	0.038	0.07?
LWC7	0.79	4.64	0.254	5.18	3.05	0.69	2.83	3.86	0.099	0.19
LWC8	0.82	3.20	0.477	9.74	3.87	1.04	3.07	4.73	0.186	0.25
KEL1	2.122	2.008	0.161	3.232	2.776	0.284	2.145	1.308	0.062	0.07

1. Derived from Eq. 4.2. See text for interpretation of physical validity
2. Step height (state (4) in Figure 2-1) consistent with this reshock state
3. Question mark indicates step was indistinct or choice of proper bump to use was unclear
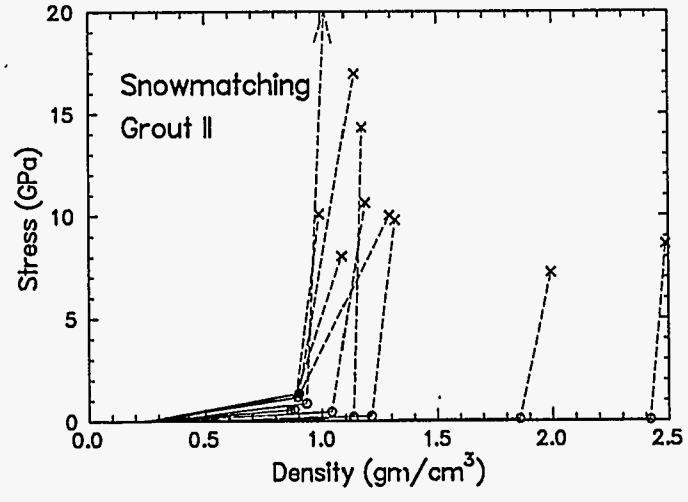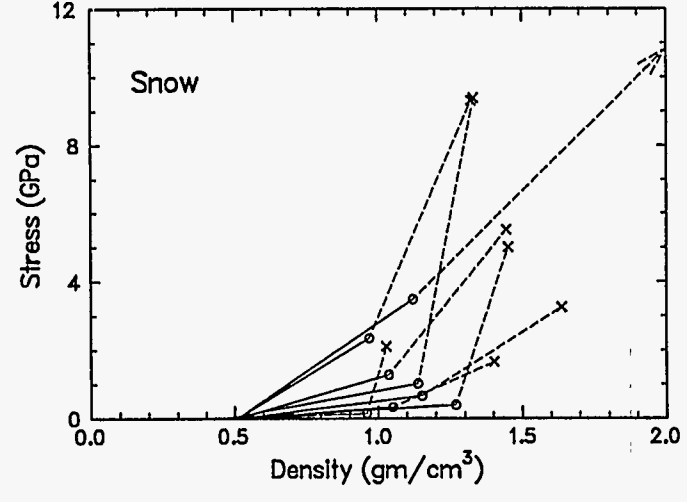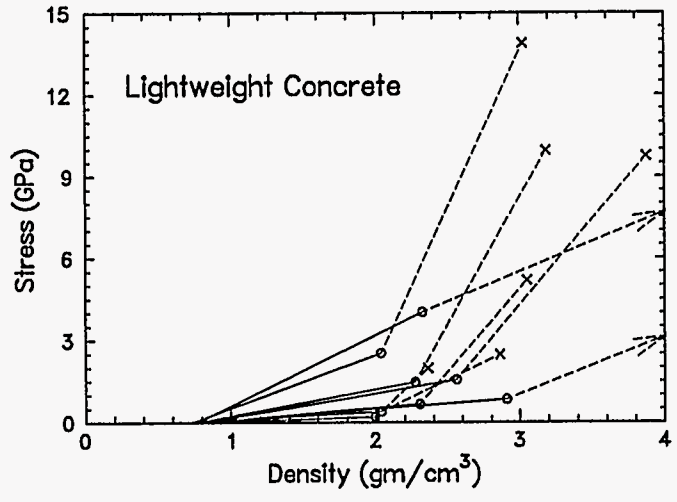
Figure 4-13. Pressure-density representations of the Hugoniot and reshock states for the snow, snow-matching grout II and lightweight concrete.

defined steps, such as Kel-1, LWC-2, SNW-4, and SGR-5, there is reasonable agreement between this value and the observed step positions. A few other profiles, such as SNW-5, several of the SGR profiles, and the higher-stress LWC profiles, show a first major step at 2 - 3 × the predicted height, while a step close to the predicted value is found, but is indistinct.

The release paths are derived through a generalization of Eq. 4.1, specifically

$$\dot{P}_m = P_m \cdot \frac{\sqrt{-\frac{\partial P}{\partial V}\Big|_{P_M}}}{\sigma} \quad \text{where} \quad \ddot{x} = \frac{P_m(t)}{\rho_{RP} T_{RP}}$$

P_m = stress in sample at boundary with ringdown plate

$\rho_{RP} T_{RP}$ = areal density of ringdown plate = σ

V = specific volume of sample

t = time

(Eq. 4.2)

The first half of Eq. 4.2 is essentially a restatement of the modulus definition, while the second half is a statement that $F = ma$.

Applying this to the test Kel-1 provides a good demonstration of how poorly the wave profile constrains the release path of the sample from the reshock state. Consider the illustration of Figure 4-14.

For the example of Figure 4-14, the release curves for the rigid-plate push method are defined by Eq. 4.3 with B_1, B_2 and B_3 chosen nearly zero and B_0 chosen as indicated on the plot.

$$\frac{\delta P}{\delta V} = \frac{-B_0}{V} \left(1 + B_1 \chi + B_2 \chi^2 + B_3 \chi^3 \right), \text{ where } \chi \equiv \frac{P}{P_{max}} - 1$$

(Eq. 4.3)

The WONDY curves are produced by a one-dimensional modeling of the experiment with the Lagrangian wavecode WONDY V [Kipp and Lawrence, 1982], assuming a Mie-Grüneisen equation of state for the Kel-F with $\rho_0 = 2.122$ gm/cm^3, $C_0 = 2.03$ km/s, $S = 1.64$ and $\gamma_0 = 1.0$. The steps are quite clearly delineated in the simulation because of the fine mesh used (67 zones across the ringdown plate) and the Lagrangian nature of the code. This contrasts with the CTH simulations of several of the experiments described in Section 5.

It is seen that a substantial change in the release path in stress - density space corresponds to a very modest change in the observed wave profile. Hence this method does not give tight constraints for the release behavior of these samples. This is by contrast with reverse-ballistic testing (sample in projectile; see Furnish [1993]), which constrains the release paths quite tightly.

For the snow and simulants, the rigid-plate push method is needed because of the lack of well-defined steps in the profiles. We have not performed a comprehensive analysis of all tests by this method, but will discuss analyses of three tests to illustrate. One profile from

each material was chosen. Release paths were constructed using Eq. 4.3, and corresponding ringdown plate motion was calculated using Eq. 4.2.

Test SGR-2 has a prominent step at a level consistent with the slope of the profile (*i.e.* the reshock stress may be calculated from the step level or the profile slope, and the values are consistent). If the portion of the profile corresponding to the release is assumed to begin at the middle of the step, the rigid-plate push method gives the release paths shown in Figure 4-15. Assuming that the entire profile to 800 m/s is available for fitting (an assumption
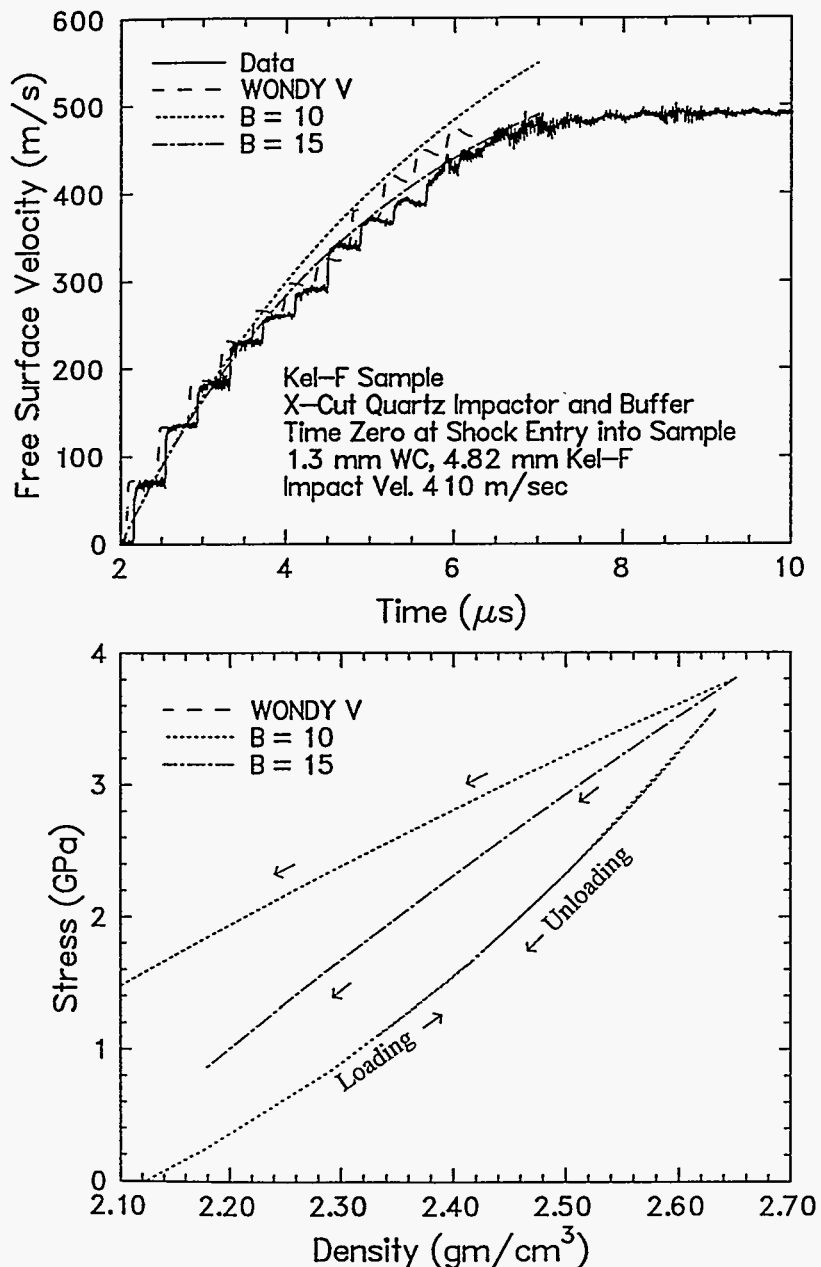
Figure 4-14. Illustrations of modeling test Kel-1. Top plot: Experimental velocity profile, with WONDY modeling and modeling from rigid plate push calculations. Bottom plot: Corresponding release paths in stress-density space.
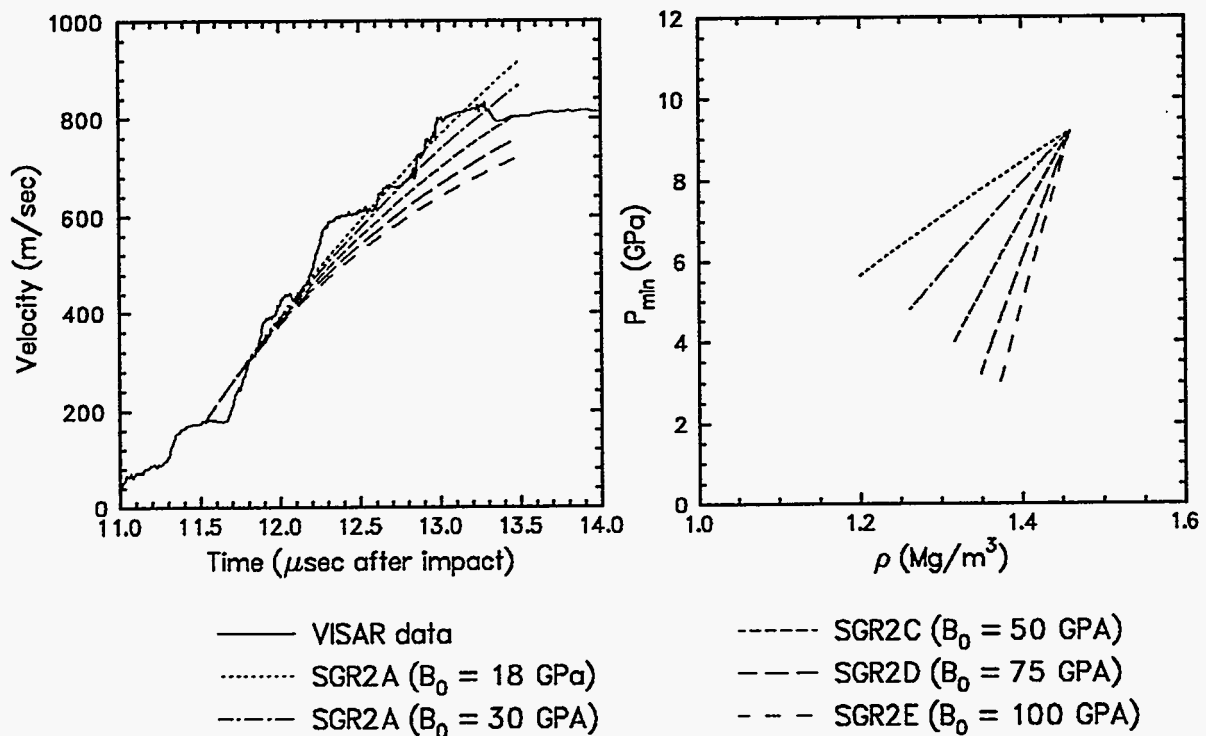
Figure 4-15. Rigid-plate release fitting of test SGR-2 (snow-matching grout II)

to be discussed in the next example), the dotted curve ($B_0 = 18$ GPa) provides the best fit. This is also the curve releasing toward the lowest density (~0.8 gm/cm^3). However, the release path is not very tightly constrained by the data.

Is it most appropriate to begin the plate motion fitting at the middle of the step? This is an ambiguity because the two methods of calculating the release (rigid-plate push and ring-down) are not compatible. Intuitively it seems sensible to either start in the middle of the step and pass through the middle of subsequent steps (as here) or start at the end of the step and pass through the end of subsequent steps.

Test SNW-2 does not have an initial step, possibly because of shock dispersion. A rigid-plate release modeling of this test is shown in Figure 4-16. Only one of the fits seems to release toward a sensible end density (~1), that with $B_0 = 10$ GPa. This fit calls into question the meaning of the profile beyond about 9.8 μs.

In fact, the arrival of the reflected reshock from the cup/sample interface is estimated at 2.5 - 3 μs after first arrival (see point "(B)" in Figure 2-1). This marks the end of the validity of the rigid-plate push model, which does not account for new forward-propagating shocks. Hence the $B_0 = 10$ GPa fit is the most reasonable.

A release fitting of test LWC-1 (Figure 4-17) also illustrates this point. The sensible fits (releases toward densities of 2.0 - 3.0 gm/cm^3) are those which ignore the later portions of the wave profile. This profile does exhibit a step at a level approximately consistent with the profile slope. It also provides an example of how the geometry of the release paths in pressure-density space can be changed through varying B_1, B_2 and B_3. However, the initial slope of the fit to the wave profile (in velocity/time space) is fixed by the reshock stress.

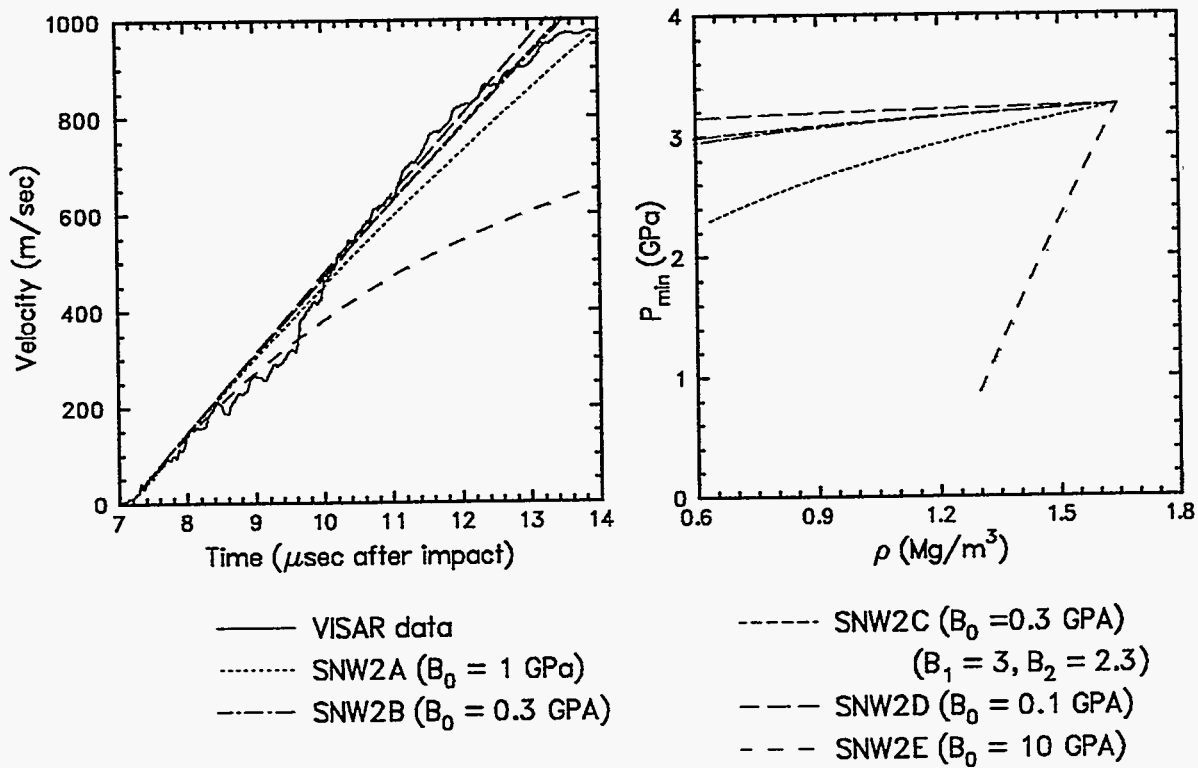37   Experimental Results

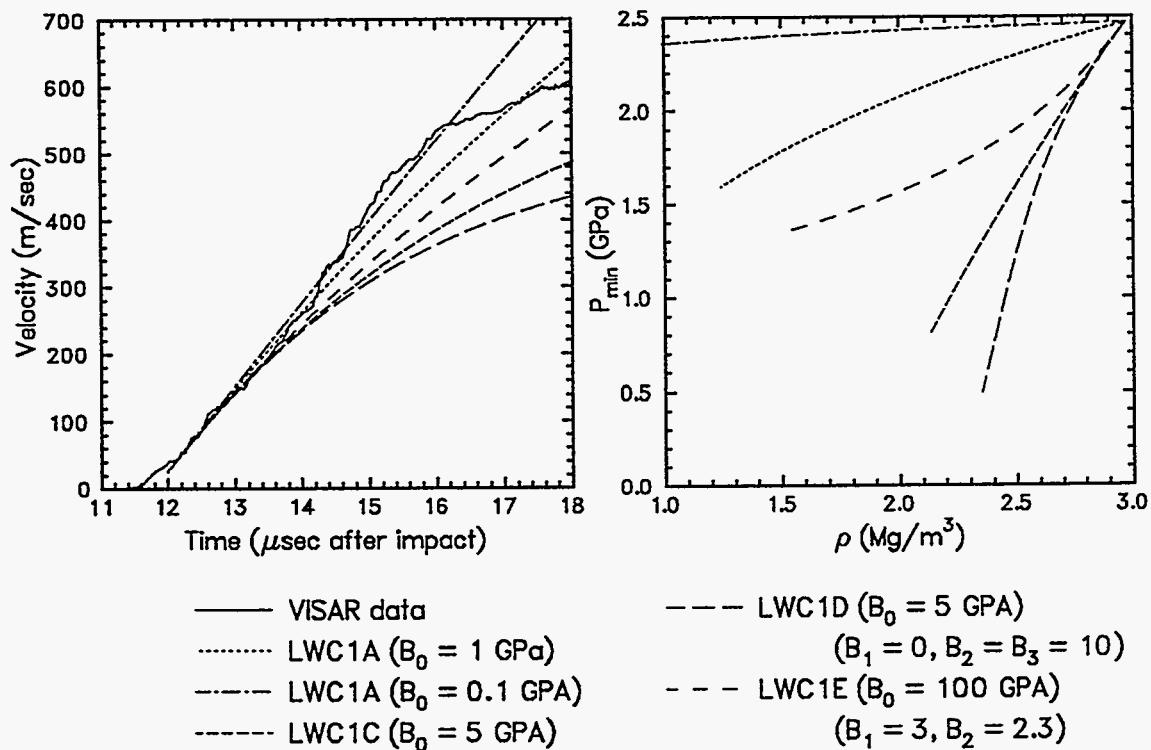Figure 4-16. Rigid-plate release fitting of test SNW-2 (natural snow)

Figure 4-17. Rigid-plate release fitting of test LWC-1 (lightweight concrete)

5.0 CTH Simulations

A careful modeling of representative experiments from this suite has two main purposes:

- As mentioned in Section 2, to assess when two-dimensional effects begin to perturb the wave profiles; and
- To relate some of the present results to material models.

Due to time limitations, we have limited our analysis to modeling three 900 m/s tests, specifically, SNW-2, SGR-2 and LWC-2.

A set of model profiles for experiment SNW-2 is shown in Figure 5-1 to present dimensionality and zone size issues. Equation-of-state issues are raised in Figure 5-2, where the experimental profile is compared with the results of 1-d modelings using three different equations-of-state.

The equation-of-state used for the dimensionality and zone size assessments is a two-phase SESAME description for porous water of density 0.51 gm/cm^3, coded as follows:.

```
MAT3  SESAME EOS=7150 FEOS='seslan'
             R0=0.51 T0=0.023 G0=1.0  TYP=1.2
             CS=3.0E4 CV=2.0E11 PT=1.0E4 BT=1.0E5
             TMAX=0.0235 E0=-3.3377E9
```
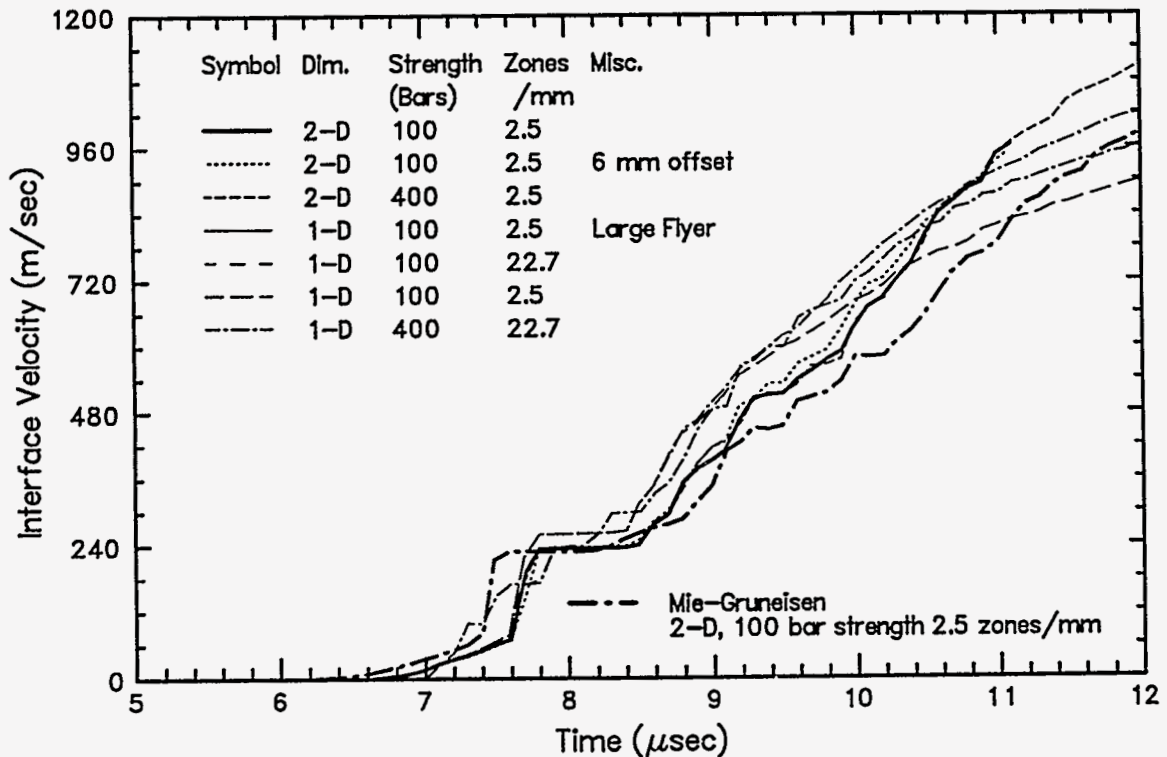

Figure 5-1. CTH model wave profiles for experiment SNW-2 (natural snow, 900 m/s impact). Dimensionality, zone size, and strength varied. Time 0 = impact. Two-phase SESAME EOS for water used except for Mie-Grüneisen run. Experiment not shown.

This corresponds to a model with irreversible pore collapse, a strength of 100 bars, a starting temperature of 0.023 eV (-6 °C), an uncrushed-state sound speed of 300 m/s, a transition modulus (V·δP/δV) of 0.1 GPa, and an initial specific energy of -3.3377E9 dynes/gm. Parameters were varied as shown in Figure 5-1.

An equation of state with porous ice was also employed, identical to the previous model except using SESAME EOS 7151 (tabular ice model).

For comparison, a Mie-Grüneisen model with P-alpha crush-up behavior was used in a run, using the following description of the snow (strength of 100 bars, C_0 = 1.72 km/s, S = 1.657, with a starting density of 0.51 gm/cm^3 and a fully dense density of 1.00 gm/cm^3):

```
* CO, S for water, with porosity added:
  MAT3 MGRUN R0=1.00 CS=1.7168E05 S=1.6575 G0=1.00 CV=2.0E11
            RP=0.51  PS=10.E5  T0=0.0218  PE=1.0E4  CE=3.0E4
```

The results shown in Fig. 5-2 indicate that the porous water model provides a more appropriate representation of snow for Hugoniot stresses in the stress range 0.1 - 1.0 GPa than does porous ice. As well, it matches the older Hugoniot data [Gaffney et al, 1985]. A test run (not shown) confirmed that the effect of varying the initial specific energy between -3.3377E9 dynes/gm and change to the tabular ice model (SESAME EOS 7151) with setting the initial specific energy to zero was negligible.

Hugoniot Points:
X Hugoniot (SNW-2)
+ ✗ Hugoniot (5 lower-stress snow tests)
O Hugoniot (3 higher-stress snow tests)

CTH Calculations
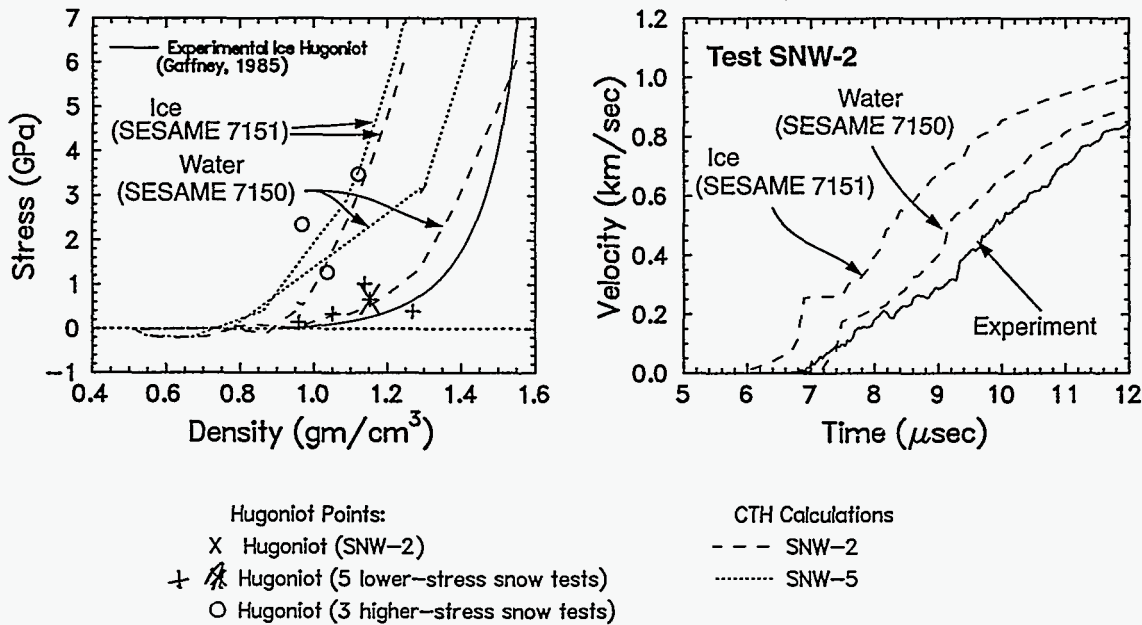- - - SNW-2
········ SNW-5

Figure 5-2. CTH model (1-dimensional) and experimental wave profiles for experiment SNW-2 (natural snow, 900 m/s impact velocity), EOS varied. Time 0 = impact. Thermal effects shift pressure/density path at higher Hugoniot stress, as illustrated for conditions of test SNW-5.

The higher-stress snow tests do not lie on the porous water curve in Figure 5-2; they lie closer to the porous ice curve. Correcting for the increased compressional heating shifts the water curve on the left side of Figure 5-2 as shown. The appearance is still that the porous ice curve is more appropriate for the three higher-stress snow tests (Hugoniot stresses of 1.3 - 3.5 GPa).

Several observations about the profiles in Figures 5-1 and 5-2 (natural snow) are:
- Strength has essentially no effect on the results (note that the 2-D plot for 400 bar strength generally overlies the heavy line representing the corresponding plot for 100 bar strength; the results are similar for perturbing the strength in 1-D).
- Zone size has as much effect on the initial arrival structure as does dimensionality. This arrival structure must therefore be assumed to be a calculational artifact.
- Edge effects may affect waveforms as early as 9.4 μs after impact.
- Arrival time is unaffected by any of the parameters varied for the SESAME equation-of-state.
- For stress levels to 1 GPa, good agreement is found between the SESAME EOS for water (7150), the Mie-Grüneisen EOS and the experimental data. AT higher stress levels, the SESAME EOS for ice (7151) provides better agreement.

Analogous CTH calculations have been made for the snow-matching grout II and the lightweight concrete. Only one EOS was considered, and only for one test per material. Results for both of these materials are shown in Figure 5-3. The overall conclusions for modeling these two materials are similar:
- The problems remain essentially 1-dimensional until at least 2 μs after the wave arrival at the free surface, and
- The calculated waveforms precede the experimental waveforms by 0.5 - 1.0 μs. These suggest that the particular models used (SESAME 2-state models for polystyrene and for tuff, applied respectively for the snow-matching grout II and the lightweight concrete) supply excessively stiff Hugoniot states in the low-stress region modeled here. Altering the uncrushed wave velocity and the transition modulus did not affect this behavior significantly; the final "phase" (crushed material) properties seem to determine gross shape and timing of the waveforms.

The snow-matching grout II is modeled as a 79% porous polystyrene (ANEOS material 7593, initial density $\rho_0=0.236$ gm/cm^3), with irreversible pore collapse. For the lightweight concrete, a 2-state SESAME equation of state developed for tuff (#7122) was applied. Tuff is a moderately quartz-rich extrusive igneous rock, with some hydration and zeolitization. The porosity was taken as 59% to give the proper starting density.

For the snow-matching grout II, the 0.5 - 1.0 μs discrepancy between the calculated and experimental waveforms may be at least partly due to the presence of Portland cement in the snow-matching grout II. The cause of the discrepancy for the lightweight concrete modeled as tuff is less clear, but probably analogous.

The timing discrepancies are probably not due to incorrect uncrushed wave velocity and strength assignments; varying these parameters up to 3 k/s (from ~2 k/s) and 0.1 GPa (from 0.01 GPa) for both materials did not significantly affect the simulated waveforms.

Some differences are observed between the 1-D and 2-D simulations, qualitatively reminiscent of those observed for snow. Specifically, the 1-D simulations predict higher particle (interface) velocities for intermediate times than do the 2-D calculations, but as the interface velocity passes the projectile velocity, the 1-D simulations begin to predict lower particle velocities than do the 2-D simulations.
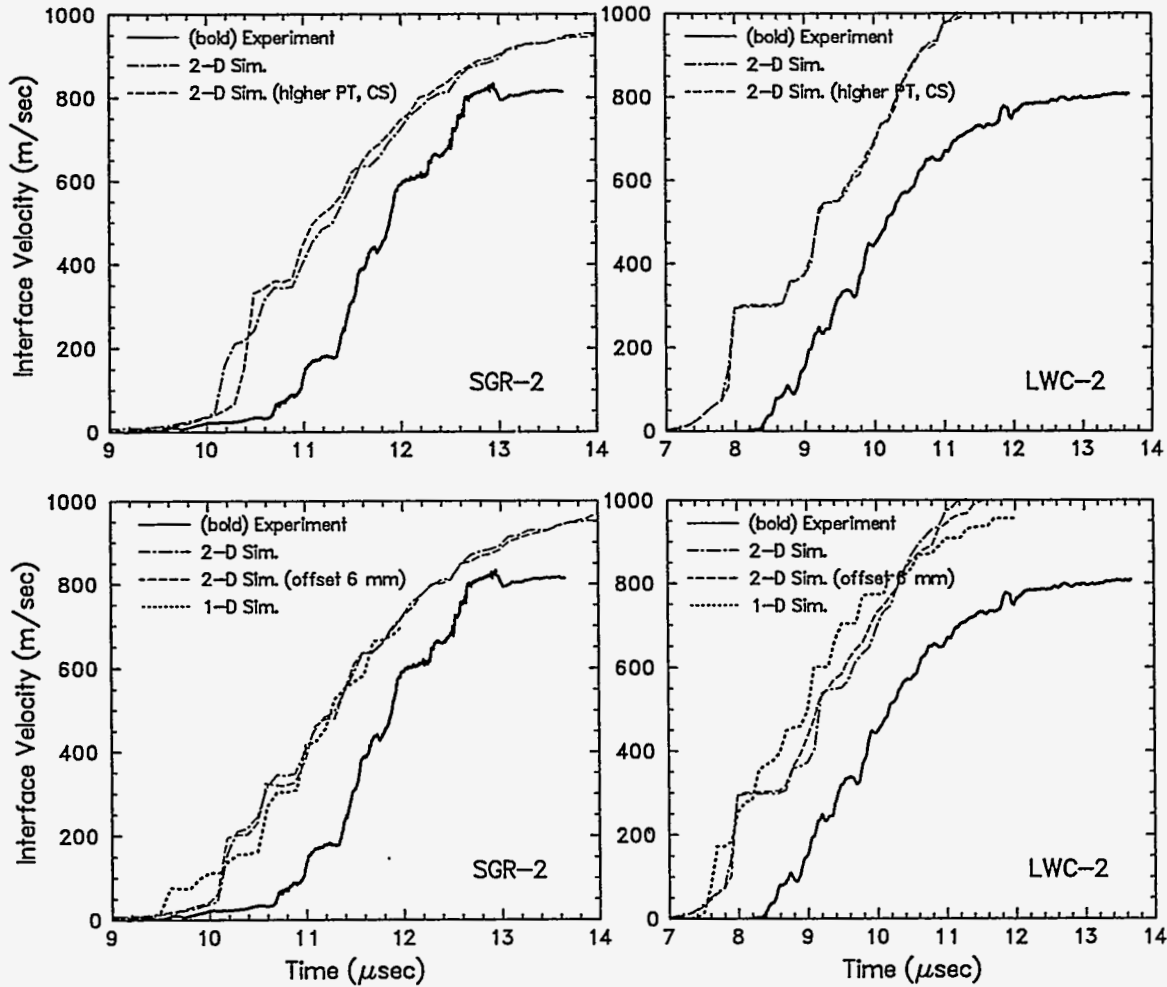

Figure 5-3. CTH model and experimental wave profiles for experiments SGR-2 (snow-matching grout) and LWC-2 (lightweight concrete). Impact velocity ≈900 m/s. "Higher PT, CS" refers to increasing crush pressure (0.01 to 0.1 GPa) and sound velocity (1.6 k/s for tuff, 2.14 k/s for polyethylene to 3 k/s) of uncrushed state

6.0 Conclusions

A family of 36 impact tests was conducted on snow and six proposed snow simulants at Sandia, yielding reliable Hugoniot states, somewhat less reliable reshock states, and limited release property information. Natural snow of density ~0.5 gm/cm^3, a lightweight concrete of density ~0.7 gm/cm^3 and a "snow-matching grout" of density ~0.28 gm/cm^3 were chosen for further study after the initial screening tests, and were the subjects of the majority of these tests. Velocity interferometry was used to measure wave profiles on all of these tests, with PVDF gauges providing supplemental information for 13 tests.

Hydrocode calculations using CTH showed that edge effects had little or no effect on the Hugoniot properties, but may have influenced inferred release properties and possibly reshock properties. The Hugoniot data gathered for the snow, the lightweight concrete and the snow-matching grout were physically plausible except in the lowest-stress region (less than 1 GPa) where unsteady wave propagation may be occurring in the grout.

CTH calculations using a Mie-Grüneisen representation of water ice, with added porosity, provided good agreement with the observed snow wave profiles. As well, a two-phase SESAME equation-of-state for porous water provided good agreement with experimental results for Hugoniot stresses up to 1 GPa. Interestingly, a similar model for ice did not provide such good agreement in this stress range, but provided better agreement for tests with Hugoniot stress levels from 1.3 to 3.5 GPa.

On the other hand, SESAME models of polyethylene, ice and rock with added porosity showed a too-stiff response. These were chosen to model (respectively) the snow-matching grout, the snow and the lightweight concrete.

The present measurements were conducted on samples containing air (pressure of ~0.84 bars), and hence would not be directly applicable to cometary impacts and other in-vacuum events, but could be applied to many terrestrial problems.

Confining ourselves to issues of mechanical shock properties, we suggest that the snow-matching grout II is likely to be a more appropriate simulant for snow than is the lightweight concrete. In the present stress range (up to about 4 GPa), the shocked density of this material is quite close to that of shocked snow (0.9 - 1.2 gm/cm^3, vs. 1.0 - 1.3 gm/cm^3 for the snow). By contrast, the lightweight concrete reaches singly shocked densities of 2.0 - 2.9 gm/cm^3. A counterpoint, however, is that the reshock properties of the snow (density increases of 20 - 60%) are closer to those of the lightweight concrete (density increases of ~50%) than to those of the snow-matching grout (density increases of ~5%).

References

Bakanova, A. A., V. N. Zubarev, Yu. N. Sutulov and R. F. Trunin, Sov. Phys. - JETP 41, 544-548, 1976.

Barker, L. M. and R. E. Hollenbach, Laser interferometer for measuring high velocities of any reflecting surface, *J. Appl. Phys*, 43, 4669-4675, 1972.

Barthel, J. R., An equation of state approach for highly porous materials: I. Application to "snow matching grout," DNA Technical Report DNA-TR-93-87, 1994.

Chhabildas, L. C. and J. M. Miller, Release-adiabat measurements in crystalline quartz, Sandia Laboratories Report, SAND85-1092 (1985). See also L. C. Chhabildas and D.E. Grady, Dynamic material response of quartz at high strain rates, *Mat. Res. Soc. Symp. Proc.*, **22** (Pt. III), pp. 147 - 150 (1984). Earlier credit for ringdown technique due to P. C. Lysne, R. R. Boade, C. M. Percival and O. E. Jones, *J. Appl. Phys.*, **40**. 3786, 1969.

Erlich, D. C. and D. R. Curran, An experimental study of shock wave transmission through snow, a snow simulant, and freon gas, DNA Technical Report DNA-TR-93-000.

Ehrlich, D. C. and D. R. Curran, An experimental technique for studying shock propagation in large-scale samples of snow and other highly-porous materials, pp. 1135-1138 in High-Pressure Science and Technology - 1993, S. C. Schmidt, J. W. Shaner, G. A. Samara and M. Ross (eds.), AIP Conference Proceedings 309, 1994.

Furnish, M. D., Recent advances in methods for measuring the dynamic response of geologic materials to 100 GPa, *Int. J. Impact Engng.*, **14**, 267-277, 1993.

Graham, R. A. and W. P. Brooks. Shock-wave compression of sapphire from 15 to 420 kbar. The effects of large anisotropic compressions, *J. Phys. Chem Solids*, **32**, 2311-2330, 1971.

Holmes, N. C., Equation-of-state measurements of low-density materials, *Rev. Sci. Instr*, **62**, 1990-1994, 1991.

Holmes, N.C., Shock compressibility of low-density foams, pp. 153-156 in *High Pressure Science and Technology -1993*, S. C. Schmidt, J. W. Shaner, G. A. samara and M. Ross (eds.), AIP Conference Proceedings 309, 1994.

Johnson, J. B., J. A. Brown, E. S. Gaffney, G. L. Blaisdell, M. Sturm and S. A. Barrett, Shock wave studies of snow, pp. 107-110 in Shock Compression of Condensed Matter 1991, S. C. Schmidt, R. D. Dick, J. W. Forbes and D. G. Tasker (eds), Elsevier, 1992.

Johnson, J. B., D. J. Solie, J. A. Brown and E. S. Gaffney, Shock response of snow, J. Appl. Phys. 73, 4852-4861, 1993.

Kipp, M. E. and R. J. Lawrence, WONDY V - A one-dimensional finite-difference wave

propagation code, Sandia National Laboratories report SAND81-0930 (1982).

McGlaun, J. M., S. L. Thompson and M. G. Elrick, CTH- A three-dimensional shock-wave physics code, *Int. J. Impact Engng.*, **10**, 351, 1990

Mellor, M., A review of basic snow mechanics, Proc. Int. Symposium on Snow Mechanics, Grindelwald, Int. Assoc. Hydrol. Sci. Publ. 114, 251-291, 1975.

Miller, J. M. and L. C. Chhabildas, A low temperature experimental capability for use with gas guns, Sandia National Laboratories Report, SAND85-0303, 1985.

Solie, D. J., J. B, Johnson and S. A. Barrett, The response of natural snow to explosive shock waves, pp. 1139-1142 in *High-Pressure Science and Technology - 1993*, S. C. Schmidt, J. W. Shaner, G. A. Samara and M. Ross (eds.), AIP Conference Proceedings 309, 1994.

Appendix A
Target Parts and Assembly

Parts and assembly of the target assemblies are summarized below. This only applies to the standard VISAR tests. For tests involving PVDF gauges modifications are necessary to ensure gauge lead survival; it is assumed the interested reader is familiar with appropriate procedures for this case. These specifications apply for a 4" compressed gas gun or a 3.5" powder gun; they should be adapted for other impact systems.

Projectiles are standard aluminum or Z-cut quartz impactors, with impactor thicknesses chosen sufficient to prevent back-surface release from interfering with the experiment. For thicknesses used in the present tests, see Tables 4.2 and 4.3.

Items required for assembly of targets:
- 1 Shot Folder with requested pin settings and any special instructions
- 1 Aluminum Target Fixture (disk approx. 6" diameter, 0.5" thick, with pre-drilled holes for the pins and a pre-machined hole with positioning ledge for the sample cup) For simulants, this piece is monolithic; for snow, it is a welded multi-piece assembly.
- 1 Tungsten Carbide Reverberation Plate (disk 0.05" thick and 2.5" diameter, with faces ground to within 0.00005" of parallelism)
- 1 Aluminum Ring to hold tungsten carbide plate
- 1 Aluminum Reservoir (cylinder without ends) to be attached to rear of target
- 1 Aluminum Retainer Ring to be held against rear of Reservoir by screws connected to Target Fixture
- 1 Circuit board to be mounted to target
- 7 Self-shorting, X-rayed pins (4 as flush pins, 3 as velocity pins) with associated 50 ohm BNC cable (For compressed gas gun tests, these are solid pins, with one serving as ground pin)
- 12 Hex-Head Screws to hold assembly together
- 1 Sample (for most simulant shots)

Directions for assembling targets:

For each of the powder gun targets for the snow and snow simulants, the following needs to be done:
- The target plate and the impact surface of the cup should be lapped.
- (Now superceded) The tungsten carbide plate should be placed in its holder ring, then glued in place. A relatively weak epoxy (eg. 5-minute epoxy) should be used, and should form an airtight seal around the ring. The bead is in the position shown on Figure A-1. Note that the tungsten carbide must be mounted with the correct surface (marked "FS" for "Free Surface") affixed to the ring.

- Clean the cup and the central hole in the target fixture of dust and other foreign matter which might affect positioning of the cup in the target fixture.
- Measure and report dimensions and densities of the sample (if provided), the tungsten carbide plate and the cup (report only thicknesses for the cup).
- The mechanical parts of the target should be assembled (NOT GLUED!) as follows (see also Figure A-1):
  (1) Place appropriate gaskets (2) in the cup and aluminum reservoir, as shown in Figure A-1;
  (2) Place the sample (if provided) in the cup, taking care to ensure that it is seated snugly. Some samples may be brittle or friable.
  (3) Place cup in target fixture in correct orientation (see Figure C-1; the flat surface of the cup - the impact surface - should face the same direction as the impact surface of the target plate, with the recessed edge of the cup fitting against the ledge in the target fixture). The impact surface of the cup will be nearly flush with the impact surface of the target fixture.
  (4) Place the tungsten carbide/holder ring unit atop the cup as shown, with the carbide facing into the cup and the surface marked "FS" facing out;
  (5) Place the Reservoir in position, with the gasketted grove against the holder ring for the tungsten carbide;
  (6) Place the retaining ring against the other end of the Reservoir; and
  (7) Secure the assembly by installing 12 hold-down screws as shown, connecting the retaining ring and the target fixture. The screws should be tightened sufficiently to compress the gaskets to give metal-metal contact, but not excessively. Tighten these screws as with an automobile wheel, working to opposite sides of the target and advancing all screws roughly together to avoid one side being much more tightly screwed down than the other. The screws are at 30 degree angles around the circle.
- Measure and report the projection of the cup from the target fixture at the four points nearest the flush pin holes (3, 6, 9 and 12 o'clock). Accuracy should be about 10 microns. If these readings are found to be significantly unequal (more that 2 mils), the assembly process above should be repeated with the cup rotated until a "best" position is found (readings as closely equal as possible). Report only the final readings.
- Mark the orientation of the cup in the target fixture.
- Set in four x-rayed self-shorting pins in holes at 3, 6, 9, and 12 o'clock so that the contact end of each pin projects from the lapped face of the target plate by an amount equal to the projection of the cup from the target plate near the same point (see "Flush Tilt Pins" in Figure A-1). These will be on the 3.25" bolt circle (pre-drilled), so no drilling of the buffer is required.
- Set in three self-shorting pins ("velocity pins") in the three adjacent holes (see Figure A-1). These will project from the lapped surface by amounts specified on information sheets furnished in the shot folder added to the projection of the cup from the target fixture at a nearby point.
- Measure the positions of all seven pins to 10 micron accuracy.

- Attach circuit board to target plate by standard techniques and wire the pins into this board. Provide BNC cabling from appropriate points on the board (ending in female couplings; may use cables which come attached to self-shorting pins).
- Report all measurements in hard-copy

For each of the gas gun targets for the snow/snow simulant studies, the procedure is the same as for the powder gun targets except that:
- The flush pins are not self-shorting,
- There are two non self-shorting velocity pins and a ground pin replacing the three self-shorting velocity pins. The ground pin is slightly (2-3 mm) longer than the two velocity pins, and
- The larger diameter bolt circle should be used for setting the flush pins, velocity pins and ground pin.
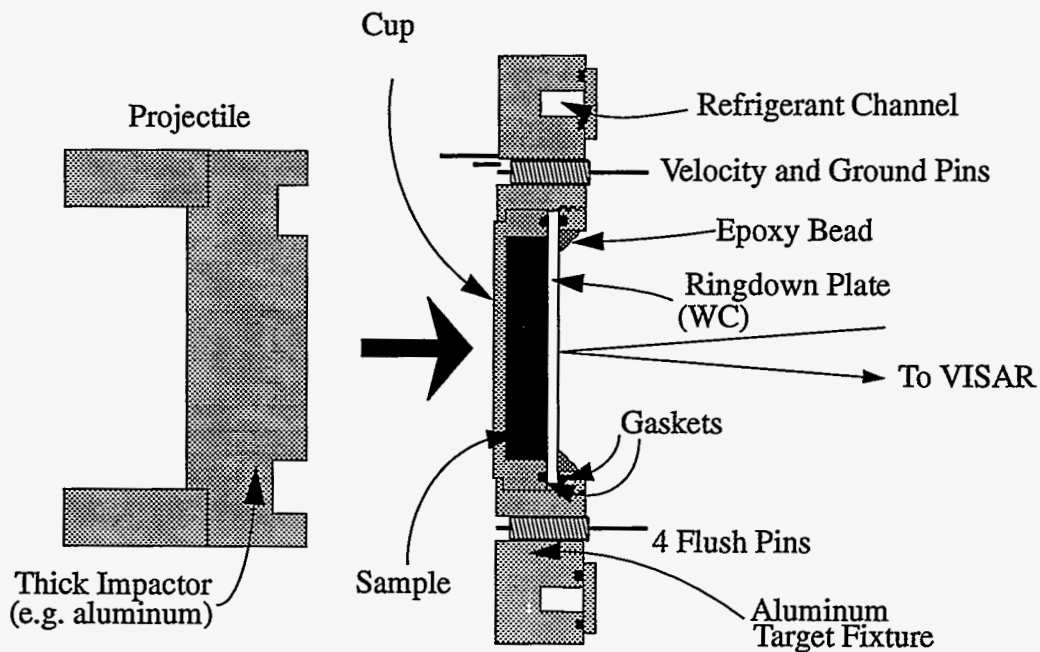
Figure A-1. Target/Projectile Illustration

Appendix B. Establishing impact time relative to wave profile

Wave profiles from the experiments conducted at the STAR Facility for this project were timed relative to impact by means of flush pins on the target. Consider Figure A-1.
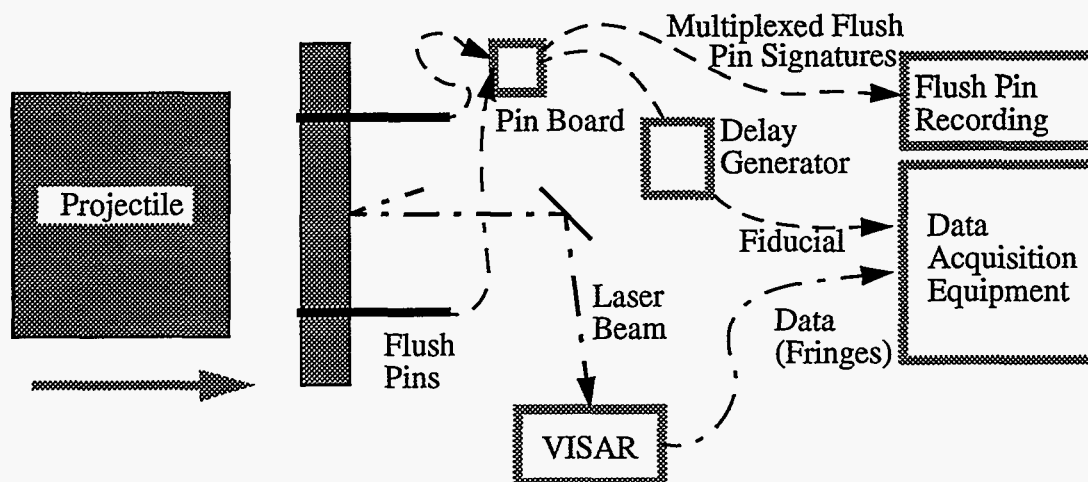

Figure B-1. Schematic of elements in establishing impact time relative to data trace. Dashed lines represent fiducial path; dot-dashed lines represent data path

Upon impact, the flush pins short, lowering or raising voltages at inputs to the pin board. The pin board transmits to the data acquisition equipment a short voltage pulse representing one of the pins which has been chosen as a reference; this pulse appears on the final records as a time fiducial. A delay generator may be added to the system to allow moving the fiducial to a convenient time on the shot record. Simultaneously, the Doppler-shifted laser beam reflected from the target travels to the interferometer (VISAR), which converts the rate of change of the doppler shift to oscillating voltages, which are transmitted over coaxial cables to the data acquisition equipment. The final record of the test is comprised of sets of these oscillating voltage records (fringe data), with the fiducial trace juxtaposed.

The pin board also transmits a separate record of the multiplexed flush pin signatures. This is stored for use in determining relative tilt of the projectile and the target (see below).

In an "ideal" experiment similar to the powder and gas gun tests described for the STAR Facility, all flush pins are truly flush, impacts are totally planar, and data transit time (via laser and electronics) is identical to fiducial transit time (via electronics). Hence setting the delay generator for the fiducial to 7 µs gives a fiducial appearing on the data trace at a position corresponding to 7µs after impact.

To decide what actual time (relative to impact) is represented by the fiducial on a particular data trace, several corrections must be made:

1) "Pin 3 Correction" -- If Flush Pin 3 (which generates the fiducial) protrudes by a dis-

tance x, the fiducial will come sooner than ideal. The correction is to the time which the fiducial marks on the data traces; i.e. a protruding pin gives a positive correction and a recessed pins gives a negative correction. This correction is $(+)x/U_{fp}$, where U_{fp} is the projectile (flyer plate) velocity. This is zero for a rear-surface pin technique, as normally used for 2-stage gun tests.

2) "Planarity Correction" -- Ideally, the impact will be "pancake" (planar). If it is not, the projectile may not impact the target at Pin 3 at the same time as it impacts the center of the target (the best "impact time"). The correction, then, is the difference between the impact time on the target at Pin 3 and the impact time at the center of the target (positive for impacting at the center first). To calculate this correction, all of the flush pin settings must be measured (positive = protruding). This is zero for a rear-surface pin technique. The relative timing of the flush pin firings ("relative FP times," FP_i) is determined from the appropriate digitizer or oscilloscope record. Each of these timings is then adjusted to give a set of relative timings which would have been obtained if the pins had been totally flush ("corrected for settings"). This is accomplished by adding $(+)x_i/U_{fp}$ to the original relative FP times for each of the 4 flush pins. Here, i is a value from 1 to 4 corresponding to the pin in question. The impact at the center is then at a relative time
$0.25 \cdot \Sigma ((x_i/U_{fp}) + FP_i) \equiv t_{corr}$, while that on the target spot at Pin 3 is at a relative time $(x_3/U_{fp}) + FP_3 \equiv t_3$. The timing correction, then, is $t_{corr} - t_3$

3) "Electronic Timing Correction" -- Ideally, data reaches the digitizers or oscilloscopes in zero time, or at least all types of data (in particular, VISAR fringes and fiducials) take the same amount of time to reach the recording instrumentation, except for a settable delay in the fiducial (taken as 7 µs in the example at the beginning of this discussion). In practice, these times differ. In our experiments, the VISAR data must travel at the speed of light from the target to the VISAR, then through the legs of the interferometer. The photomultiplier tubes have a finite response time (about 18 ns), then travel time through cabling to acquisition electronics must also be added to the total travel time. Write this travel time as T_{Data}. The fiducial must travel through a very small circuit board, then through cabling, a delay generator and more cabling. In the powder gun and 2-stage gun tests it then triggers an LED on the VISAR photomultiplier tubes. The signal then travels with the VISAR signals (as an added voltage pulse) to the recording instrumentation. In the gas gun tests, it goes directly into the acquisition electronics. Write this travel time (including the zero-setting delay of the delay generator) as T_{Fid}. Then the timing correction is $T_{Fid} - T_{Data}$.

All of these corrections are added to the dialed-in time of the fiducial delay to calculate an actual time of the fiducial relative to impact. The data trace is then shifted in time so that the observed fiducial occurs at that time.

We have found that one of the most important factors in determining the accuracy of this procedure is the rigidity of the projectile front element. If this element bows during launch, timing accuracy may be degraded by up to 100 - 200 ns; otherwise it will be better than 20 ns.

Appendix C. Discussion of PVDF data

C.1 General comments

In the main body of the report, the detail of the PVDF records has been de-emphasized in the interest of clarity and brevity. The PVDF gauges were used in a exploratory fashion, as there has been very little experience in using this technique in course-grained heterogeneous environments. Using these gauges in combination with VISAR measurements provided a redundant means of extracting information. As it turned out, these records could not be converted to reliable stress/time profiles because of the course-grained heterogeneous nature of the samples. However, the records were still useful in establishing wave profile timing; for the tests at the Building 808 gas gun facility this was the most convenient method. Comparison of timing from gauges in equivalent positions also provided a measure of the uniformity of sample loading.

Section C.2 below discusses the use of PVDF gauges in these experiments. Sections C.3 and C.4 provide a summary of each experiment; the times are given relative to triggering of the digitizers. Section C.3 summarizes the snow and snow simulant experiments, and Section C.4 discusses Kel-F. Section C.5 is comprised of plots from these tests.

C.2 PVDF measurements

Under ideal conditions, when operated in "current mode", piezoelectric PVDF gauges put out a current that is directly related to the time derivative of the normal stress. Time-resolved stress is therefore a monotonic function of the time integral of the measured current. If the time of arrival at a gauge is defined as the steepest part of the shock front, then the first peak in the raw data corresponds to the time of arrival. Time-resolved stresses were determined by integrating the PVDF output signal; however, we believe these stresses are not representative of the average material, but only of its local properties.

When the output gauge signals are integrated, the resulting waveforms are inconsistent with any stress history that would be expected, and are also in disagreement with one another. This observation can be explained by the extremely nonuniform stresses and nonplanar shock wave expected from a material that has heterogeneities (pores and inclusions) on a scale greater than the scale of the 0.025 mm thick, 3-mm wide PVDF gauges. Unlike waves in homogeneous materials, stress waves arriving at the gauge active area may locally be highly inclined, giving rise to erroneous stress measurements. If the stress measurement were accurate, it would still represent only the local conditions of the heterogeneously loaded material. Nevertheless, these PVDF gauges can provide excellent time-of-arrival data. This is best illustrated by experiment 2414 (see next section).

For most tests, two figures are included. The first figure for each experiment contains the measured (current) data for both PVDF gauges. The second figure presents reduced VISAR data plotted on the same time-base as the raw output of the input PVDF gauge (other gauges may also be plotted in this figure). These signals were recorded on the same

digitizer as the VISAR, so the only correction to the timing comes from the difference between the transit times of the PVDF and VISAR signal lines. This correction will shift the VISAR data about 0.12 microseconds to the left (smaller time) relative to the PVDF data.

C.3 Snow and snow simulant experiments

Lightweight Concrete tests

Experiment 2414 Lightweight Concrete 8

The output gauges are inductively coupled to the input gauge, hence all three provide a sharp time mark when the shock wave arrives at the first interface (note the extremely high frequency electrical ringing--this does not show up on the integrated waveform). There is a nearly simultaneous arrival on all three gauges at 2.124 microseconds. This is possibly either a weak elastic wave or an air shock transmitted through interconnected pore space, because there is no evidence for it in the VISAR data.

Experiment 2413 Lightweight Concrete 7

The output PVDF gauges show a very clear inductive coupling to the input gauge, providing an accurate time mark of first arrival. Output gauge 2 shows anomalous behavior at this time--there is no obvious reason it should remain deflected from the baseline. There are two other pulses measured by this gauge, the second (at about 4 microseconds) shows up weakly on gauge 1 as well. A clear arrival appears on gauges 1 and 3 at about 4.6 microseconds.

Experiment 2412 Lightweight Concrete 6

Again, the output gauges show good coupling to the input gauge. All three output gauges in experiment exhibit an unexpected ringing at about 2 microseconds. This high frequency pulse also appears on the input gauge. It does not appear on the integrated waveform, so it is from some noise source external to the gauges. At about 4 microseconds, the three output gauges (but not the input gauge) exhibit a small pulse similar to the elastic or air shock of experiment 2414. Subsequently, the gauges show slow deflections indicating stress loading, with stronger but still spread-out loading a few hundred nanoseconds before free surface arrival.

Snow Matching Grout II tests

Three experiments were originally planned for the snow matching grout on the Building 808 gas gun, but because of a loss of VISAR data on two shots a total of five were performed to obtain a complete set of data. As was done for the light-weight concrete experiments, thick aluminum flyers were launched at nominal velocities of 0.4, 0.8 and 1.2 km/s, impacting the targets which consisted of (nominally) 2 mm thick aluminum driver, 6 to 7 mm thick sample, and 1.4 mm thick tungsten carbide ringdown plate. The snow matching grout samples were slightly thicker than the light-weight concrete samples because of the extreme heterogeneity and large pore sizes in the grout.

The major difference between this and the light-weight concrete test series is in the use of

PVDF gauges. In the previous set, carefully poled "Bauer"-type PVDF gauges were used in current mode, with precision current-viewing resistors. It quickly became apparent from those first three experiments that heterogeneous materials such as these snow simulants are not amenable to time-resolved PVDF stress measurements, and use of Bauer gauges is unnecessarily difficult and expensive if time-of arrival information is all that is provided.

With this in mind, the three "output" gauges (those placed at the sample-WC interface) were replaced by gauges that were not subjected to the Bauer poling process. We continued to use Bauer gages and precision CVRs as the "input" gauges (driver-sample interface).

As before, these signals were recorded on the same digitizer and therefore the only correction to the timing comes from the difference between the transit times of the PVDF and VISAR signal lines. This correction will shift the VISAR data about 0.12 microseconds to the left (negative time). Interpretation of the experiments proceeds by taking the indicated time of the pulse on the input gauge as the time of entry of the shock into the sample.

Experiment 2418 SGR 6

The input PVDF gauge experienced a very sharp arrival. Output gauges 1 and 3 responded to the input gauge arrival via electromagnetic coupling. A long-lasting electrical ringing is present with a period consistent with a reverberation in the data lines (120 ns round trip). The data lines were terminated at the digitizer end, but not at the gauge end. Output gauge 2 appears to have a broken or shorted lead (not surprising--these particular gauges had never been used in our lab before, and are very difficult to install in targets in the configuration provided). At about 4.5 microseconds, gauges 1 and 3 exhibit an arrival, possibly an elastic or air shock. After about 12 microseconds, the output gauges appear to experience arrivals, and output gauge 2 puts out a high frequency ringing. VISAR data was not obtained.

Experiment 2419 SGR 7

Very sharp arrival from the input gauge, with coupling to output gauges 1 and 3. One of the leads for output gauge 2 was broken during assembly; a small inductance loop was attached in an attempt to couple to the broken gauge, without success. Gauge 3 exhibits significant offset from baseline at around 5 microseconds, but without a distinct arrival. After about 9 microseconds, both output gauges exhibit signals consistent with multiple shocks and releases, with no well-defined single arrivals. VISAR data was not obtained.

Experiment 2420 SGR 8

Input PVDF gauge missed arrival due to too long a trigger delay setting. When scope triggered, output gauge 1 was still ringing from inductive pulse received from input gauge. Gauge 1 puts out a sharp pulse at about 1.8 microseconds, and a gradual rarefaction between 5 and 6 microseconds. Output gauge 3 was known to have a broken lead during assembly, and an attached pickup loop did not put out any signal. Output gauge 2 was also apparently damaged during assembly and failed to put out data.

Experiment 2423 SGR 10 (Repeat of 2418)

Very sharp arrival on input PVDF gauge, picked up inductively on all three output gauges. Output gauge 1 was terminated with 50 ohms at the gauge end, and gives a much cleaner signal than the other two (unterminated) gauges. Sharp pulse with high-frequency ringing indicative of inductive pickup is seen simultaneously at all three output gauges at about 2.3 microseconds. Possible source could be an input gauge lead breaking resulting in a sudden change in input gauge current (this may be the cause of simultaneous ringing on output gauges for shot 2412 as well). As observed before, output gauges experience no sharp arrivals.

Experiment 2424 SGR 9 (Repeat of 2419)

Very sharp arrival on input PVDF gauge, picked up by two output gauges. Output gauge 2 failed. As before, only ragged arrivals on output gauges.

Natural Snow tests

The targets for the natural snow experiments were more complicated than those for the simulants, because it was necessary to 1) cryogenically cool the sample to prevent it from melting, 2) continuously monitor the temperature of the sample, and 3) purge the space adjacent to the VISAR reflector to avoid frost buildup. We chose to build these targets with only one "output" PVDF gauge, because 1) the increased complexity of the targets and 2) the lack of consistent data from multiple "output" gauges for the simulant shots.

The PVDF signals were recorded on the same digitizer as the VISAR, so the only correction to the timing comes from the difference between the transit times of the PVDF and VISAR signal lines. This correction shifts the VISAR data about 0.12 microseconds to the left, as has been the case for all shots for this project.

Experiment 2429 SNOW 6 (0.4 km/s)

Bauer gauges were used for both input and output. The input gauge experienced a sharp arrival, providing an excellent timing fiducial. Subsequent arrivals appear at the input gauge at later times. The output gauge responded to the input gauge arrival via electromagnetic coupling. The setting was not sensitive enough to record any clear arrivals.

Experiment 2425 SNOW 7 (0.8 km/s)

Uncalibrated PVDF gauges were used in both positions. Sharp arrival from the input gauge, with coupling to the output gauges, yielded a good timing mark. Multiple sharp arrivals at the input gauge, presumably from reflections off of the tungsten carbide, demonstrate that under certain conditions the PVDF gauges can yield rich additional information. This data can be used to determine multiply-shocked states. The output gauge recorded weak evidence for various arrivals.

Experiment 2430 SNOW 8 (1.2 KM/s)

Bauer gauges were used. Very sharp arrival on input gauge was observed, picked up by output gauge for good timing. Subsequent burst of noise on output gauge integrates to show arrival of compressional wave at that time.

C.4 Kel-F Test 1 (808 shot #2438) wave profiles.

Figure C-1 presents an impedance-match diagram for test Kel-1 together with measured stress-time wave profiles from a PVDF gauge at the sample/cup interface (solid line trace originating at 2 μs; this gauge is referred to as the "input gauge" because the shock is input here) and two ("output") gauges at the sample/ringdown plate boundary.

Symbols KEL-F, WC, Al and Z stand for the Hugoniots for Kel-F (sample), tungsten carbide (ringdown plate), 6061-T6 aluminum (cup) and Z-cut quartz (impactor), respectively.

State 2 is produced at the cup/sample interface, and is in good agreement between the impedance-match diagram and the wave profile.

States 3, 5, and 7 are produced at the sample/ringdown plate interface, and again are in good agreement between the impedance-match diagram and the wave profile.

For reference, the VISAR samples the particle velocities for states 4, 6, 8, 10, ...

The jump observed in the input gauge at about 5.3 μs is due to arrival of the backward traveling reshock from the ringdown plate. This should correspond to the transit to state 5', although an apparent relaxation or attenuation has caused the observed stress here to be far lower than predicted (2.4 GPa vs. 4.6 GPa).

For test Kel-1 (Kel-F sample, Z-cut quartz target, impact ~400 m/s), stress-time profiles were deduced and are presented along with an impedance-match diagram for interpretation.

C.5 Figures for the PVDF experiments

The following figures present the PVDF gauge records superposed on one another and/or on VISAR velocity records for each of the tests conducted using PVDF gauges, i.e. those performed at the Building 808 gas gun facility.
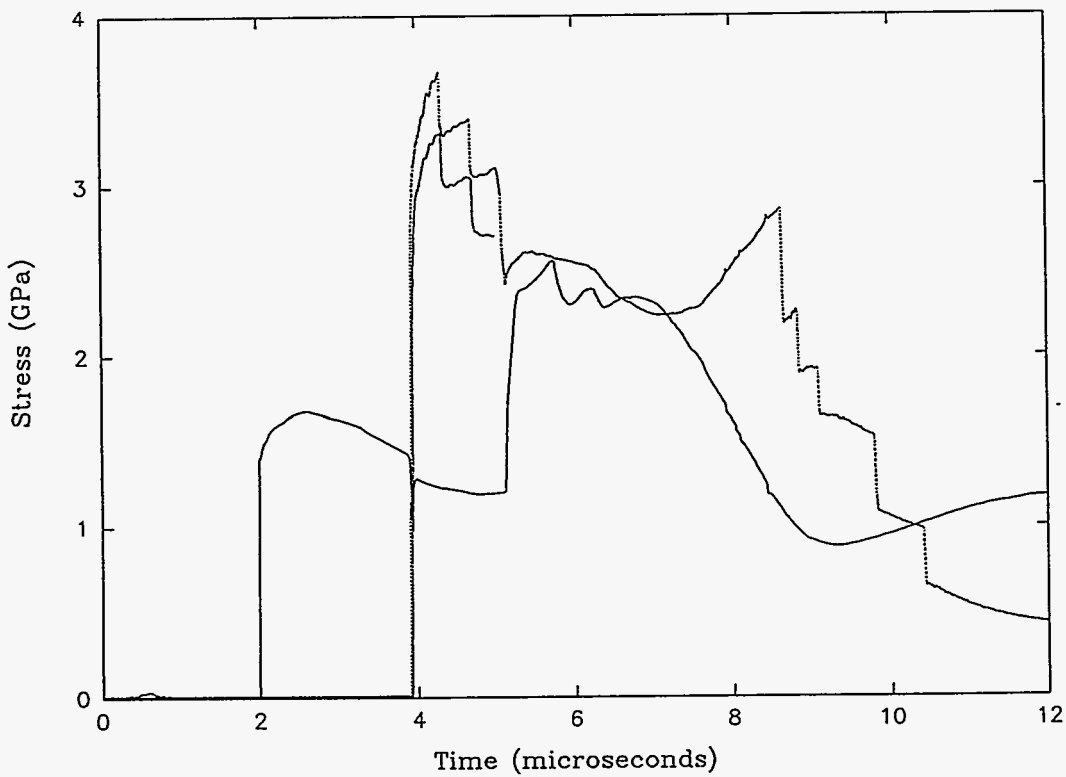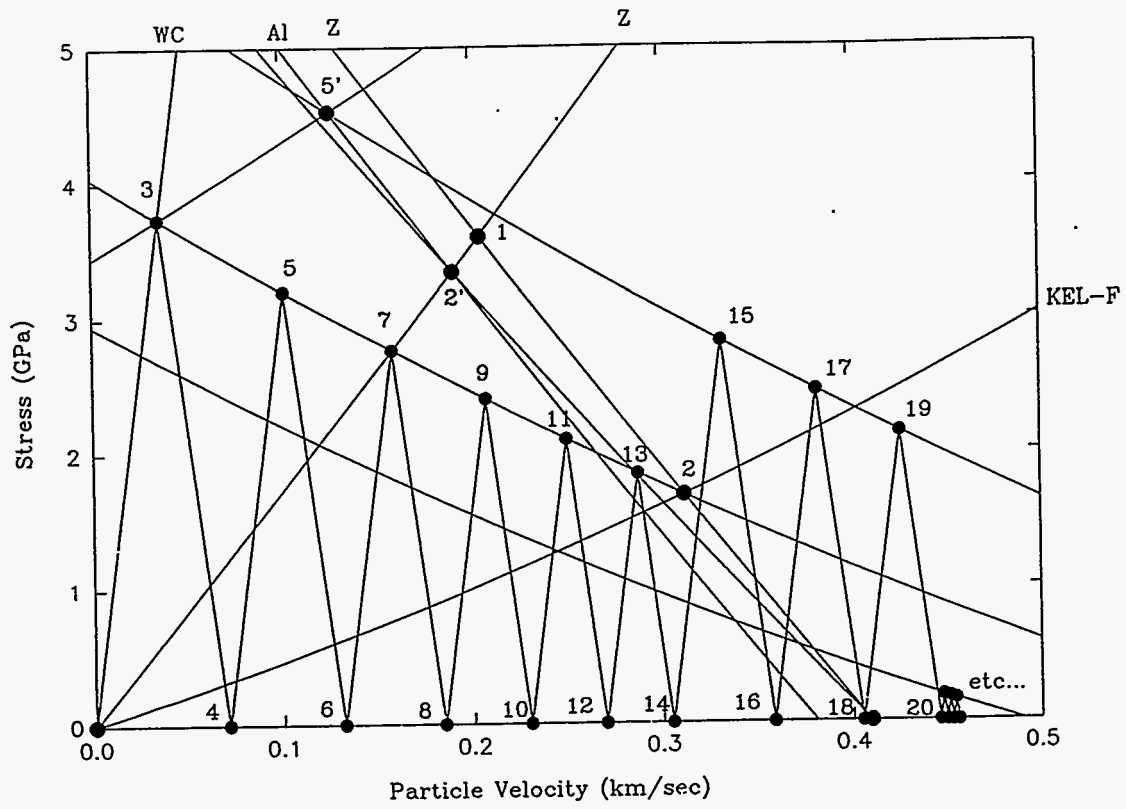
Figure C-1. Kel-1 impedance match diagram (top) and observed stress histories (bottom)
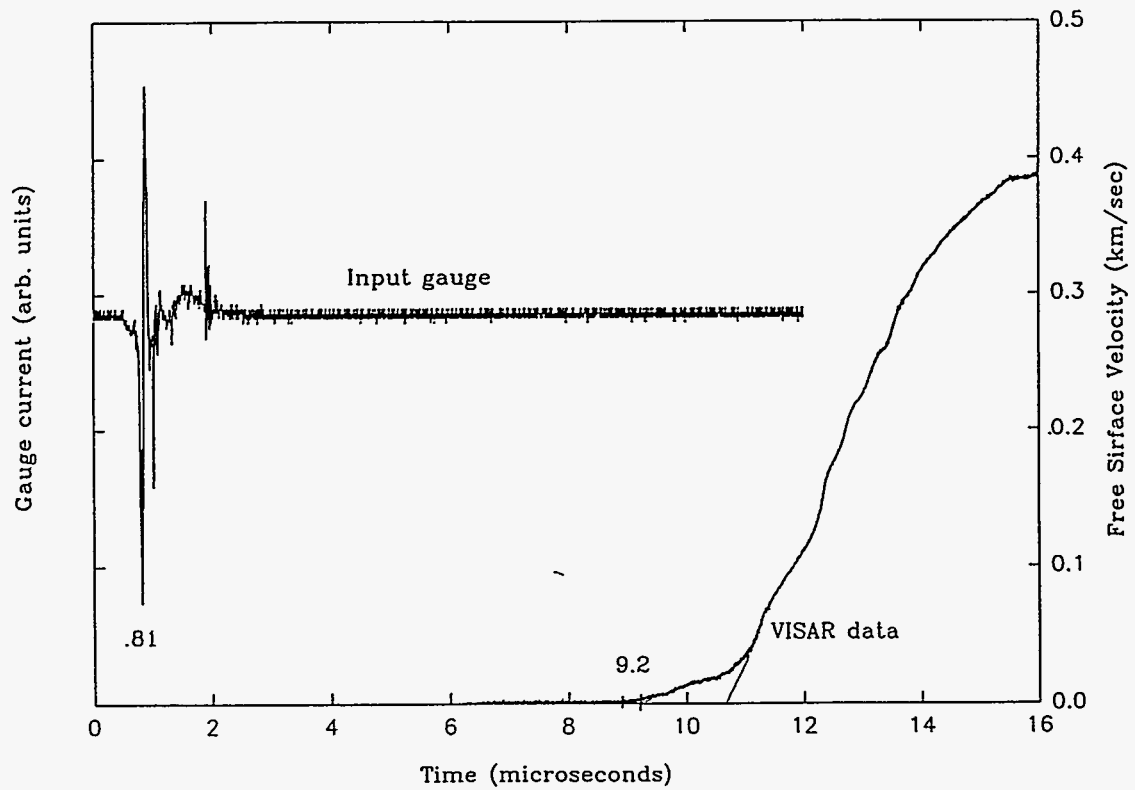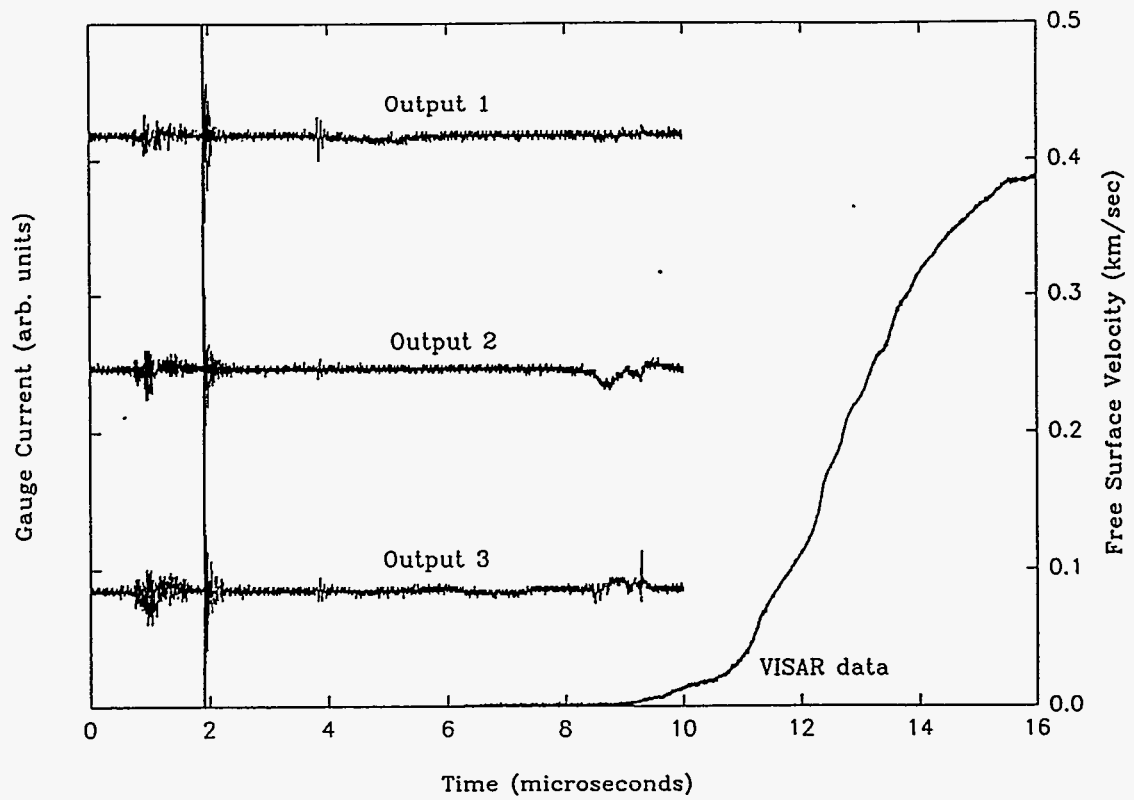
Figure C-2. PVDF and VISAR records for test LWC-6. See text for interpretation.

Appendix C
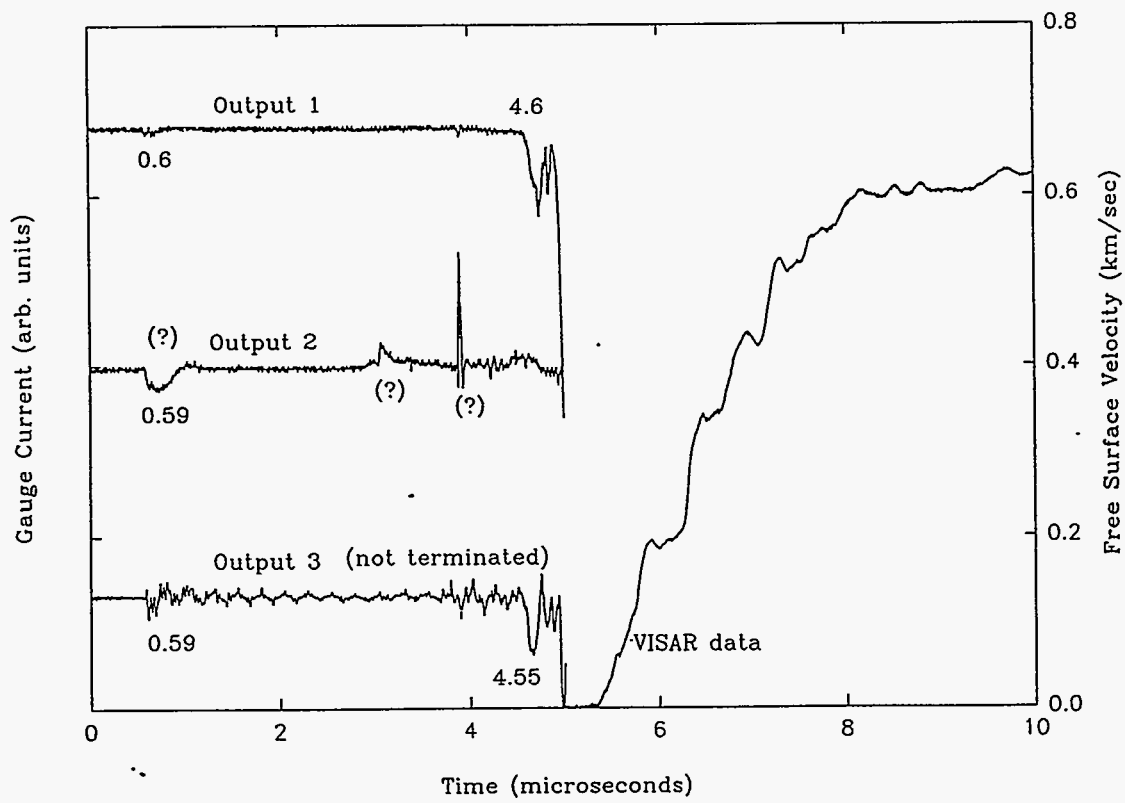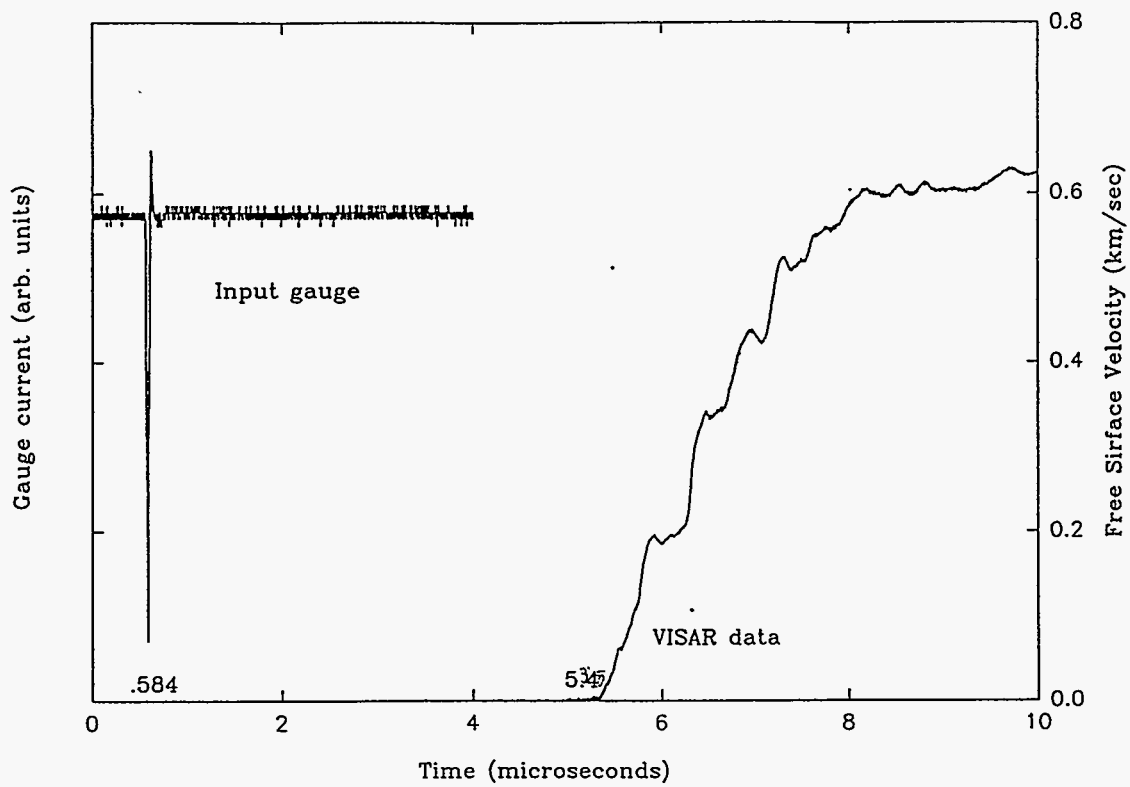
Figure C-3. PVDF and VISAR records for test LWC-7. See text for interpretation.
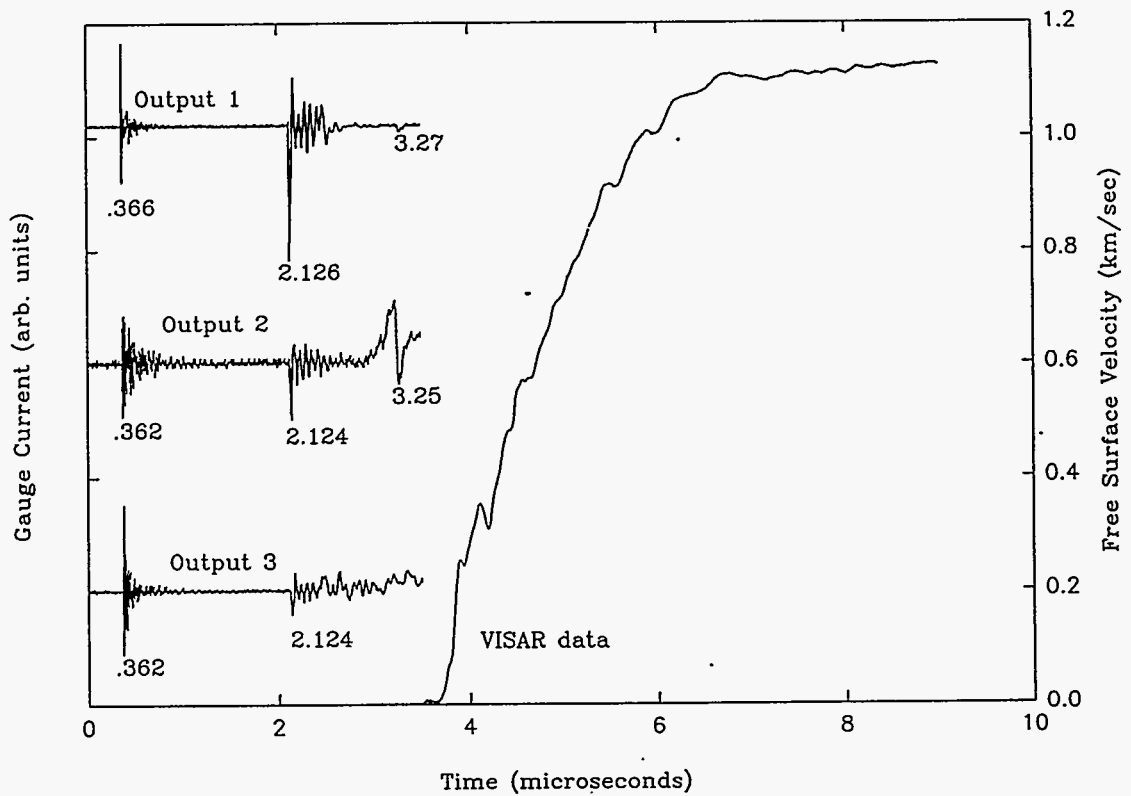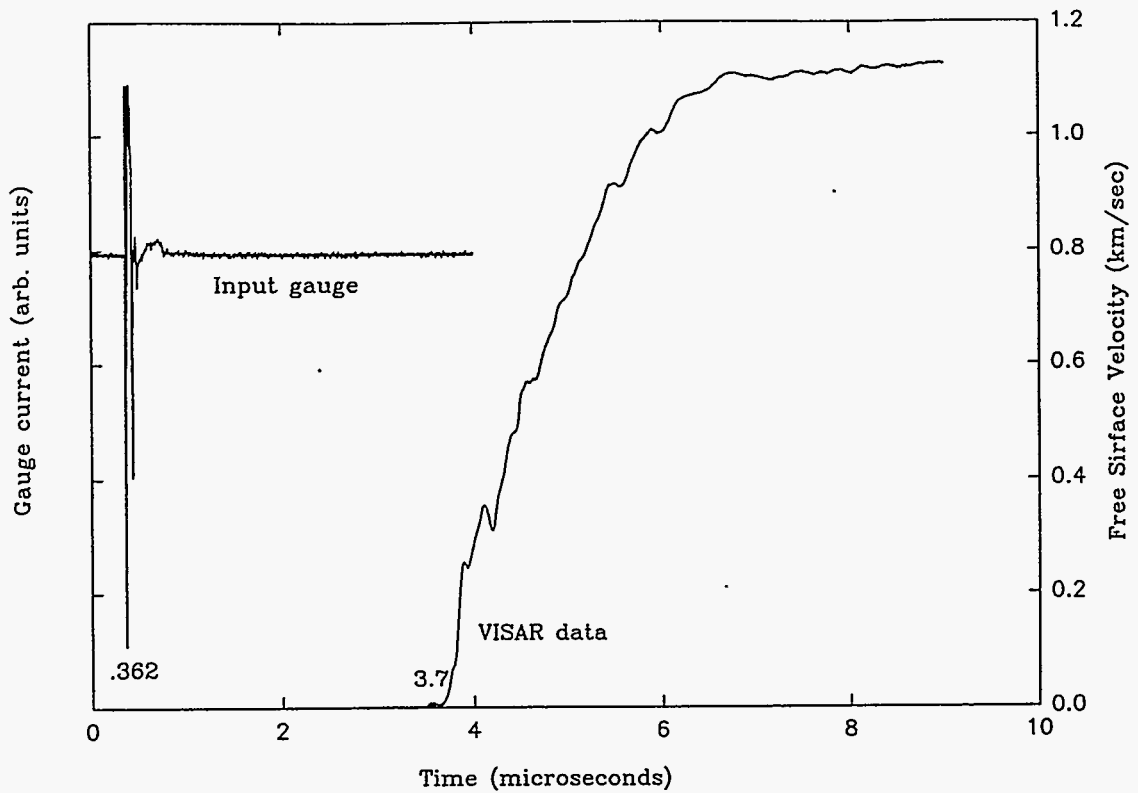
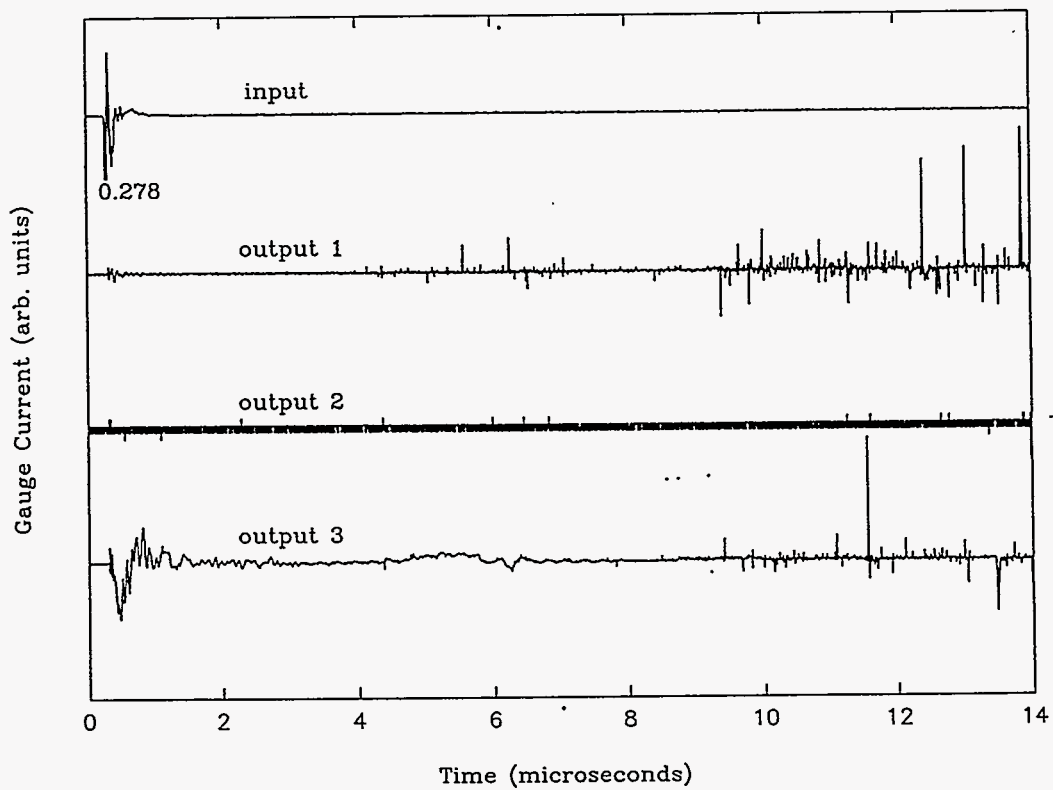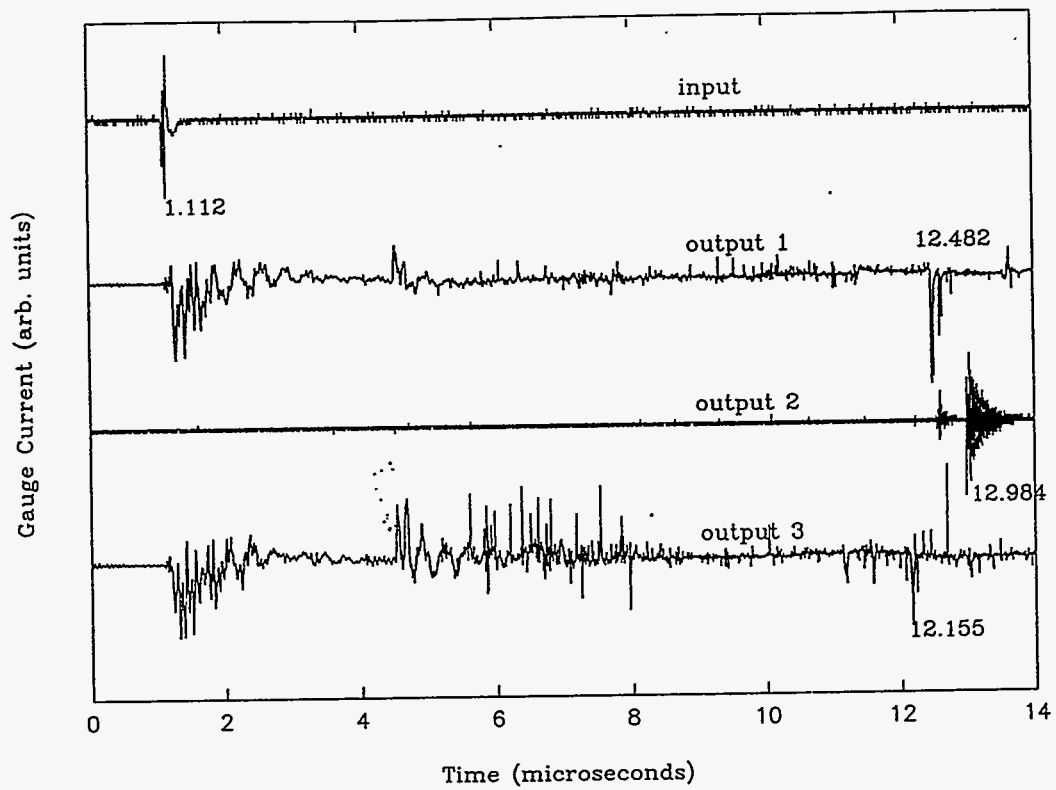Figure C-4. PVDF and VISAR records for test LWC-8. See text for interpretation.

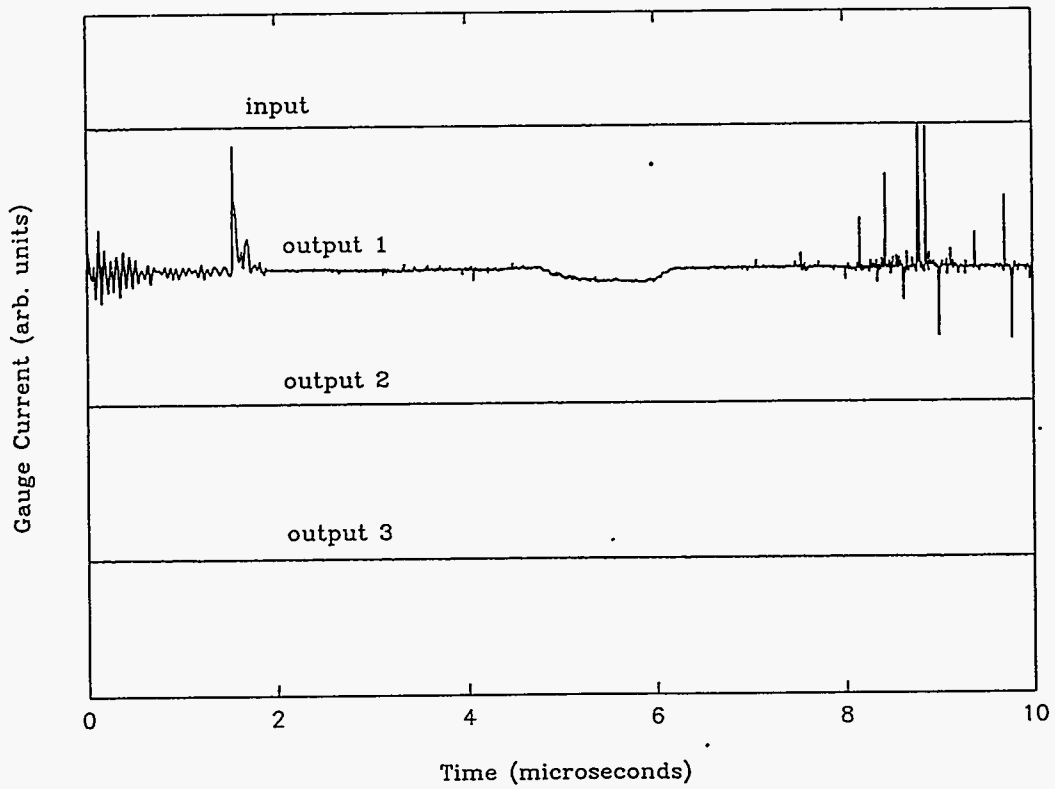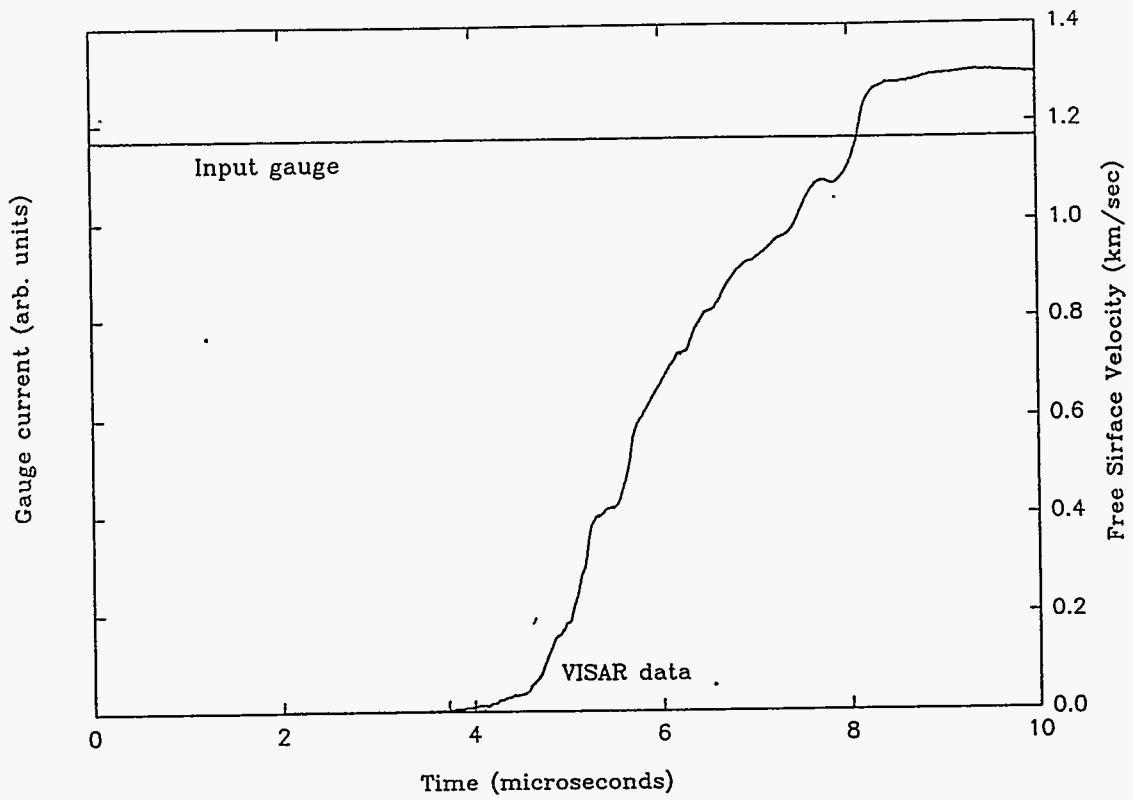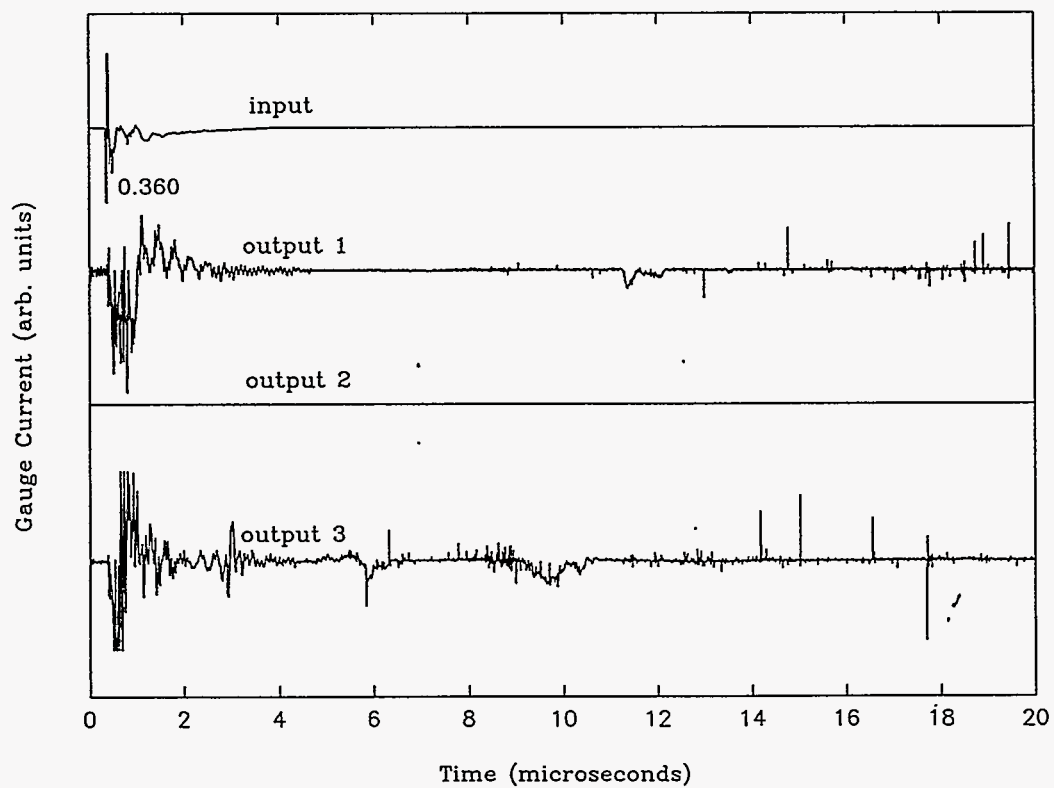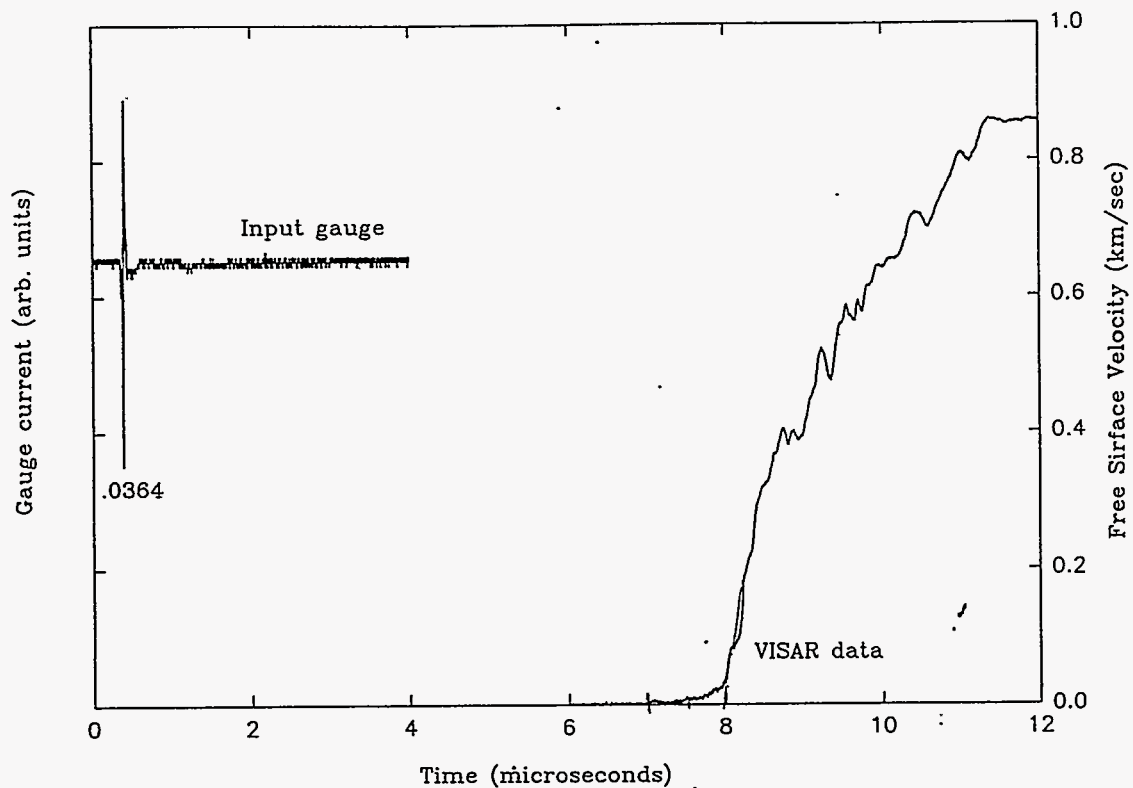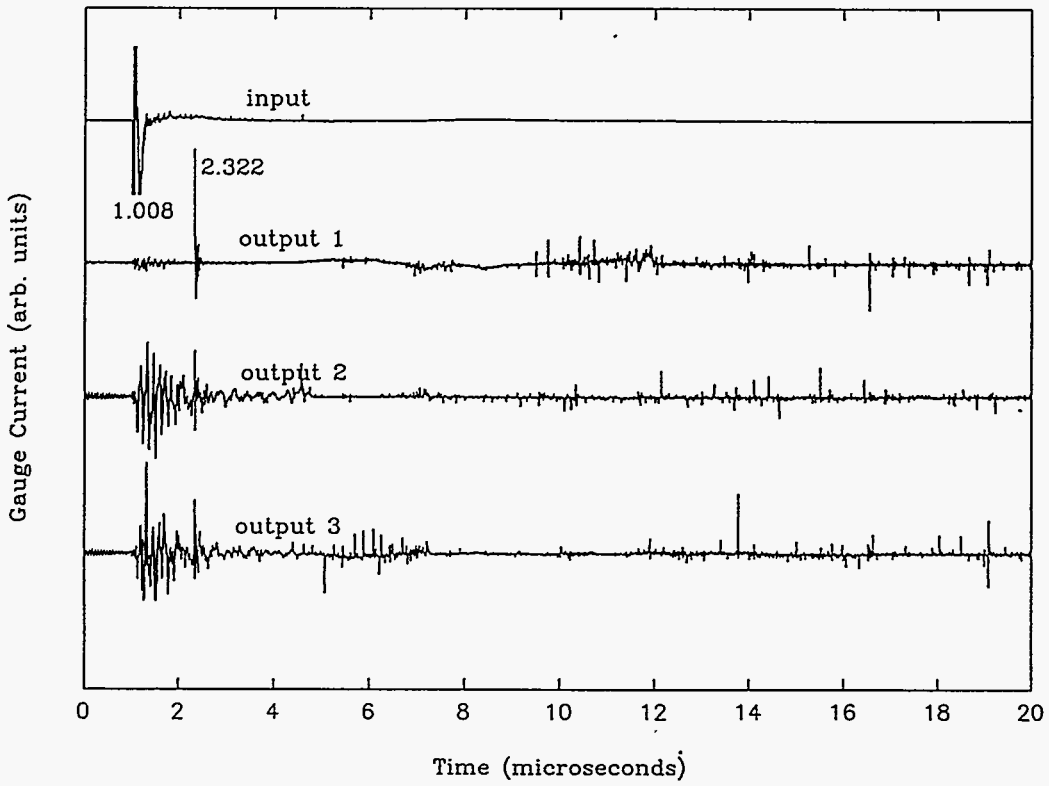Figure C-5. PVDF records for tests SGR-6 and SGR-7. See text for interpretation.

Figure C-6. PVDF and VISAR records for test SGR-8. See text for interpretation.
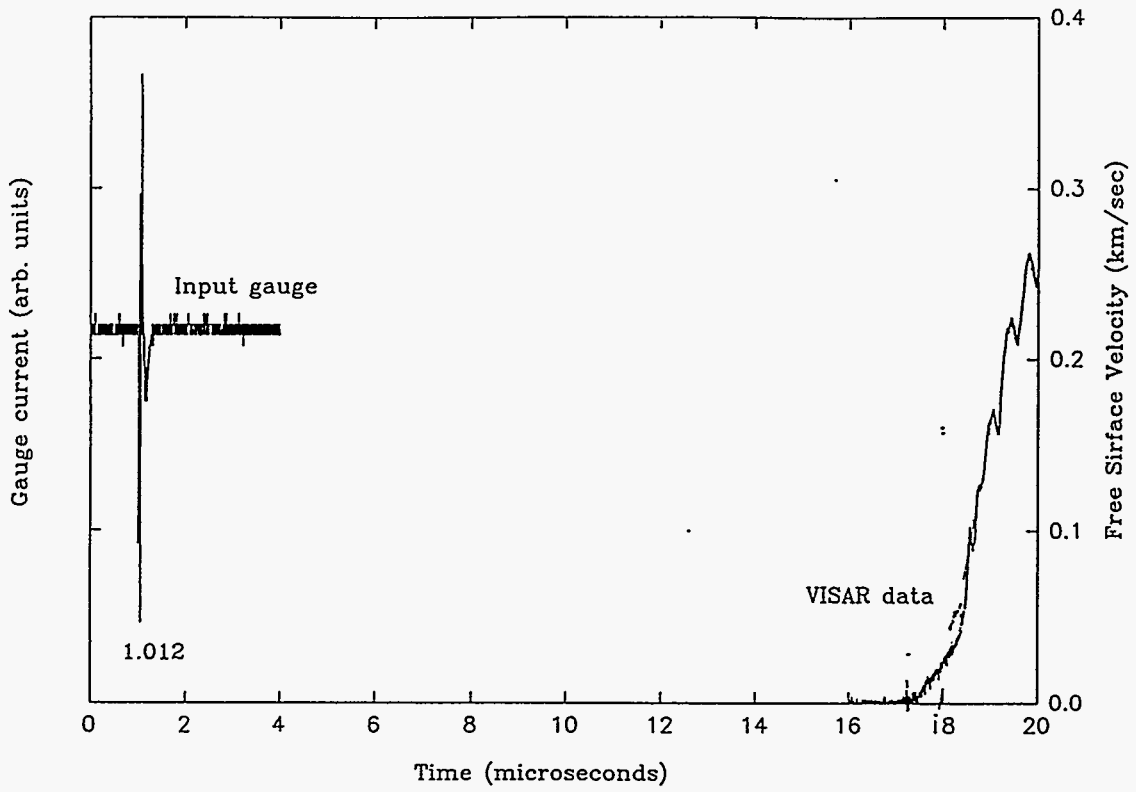
Figure C-7. PVDF and VISAR records for test SGR-9. See text for interpretation.

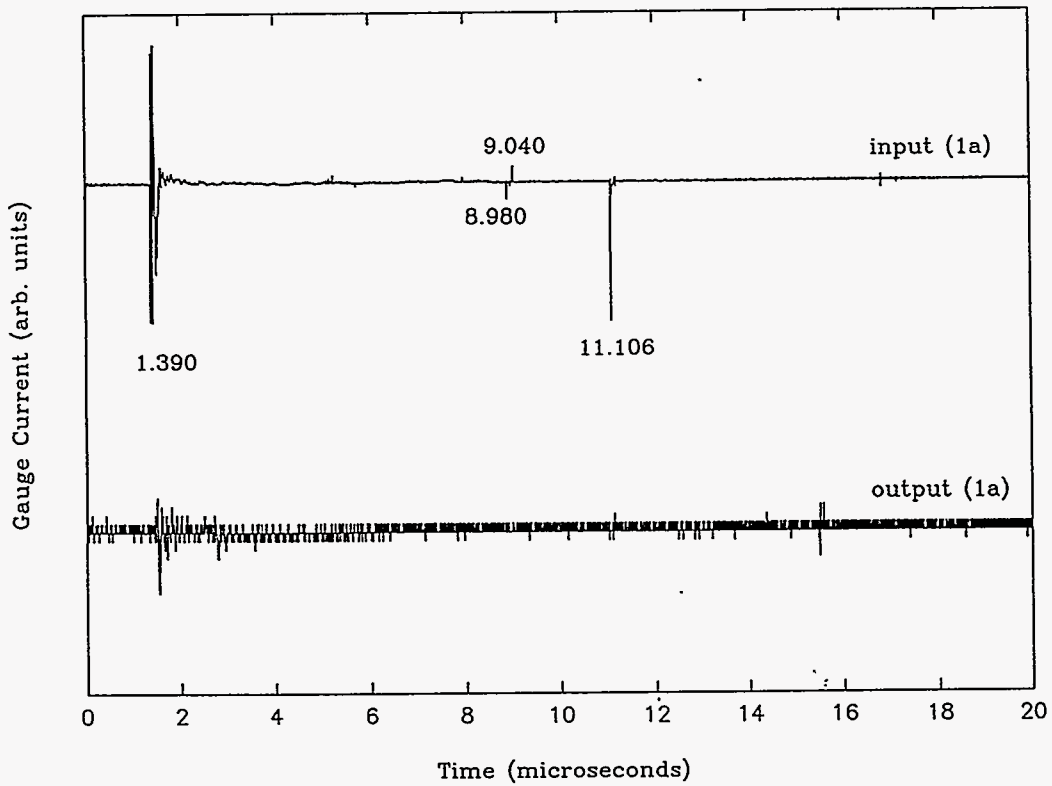Figure C-8. PVDF and VISAR records for test SGR-10. See text for interpretation.
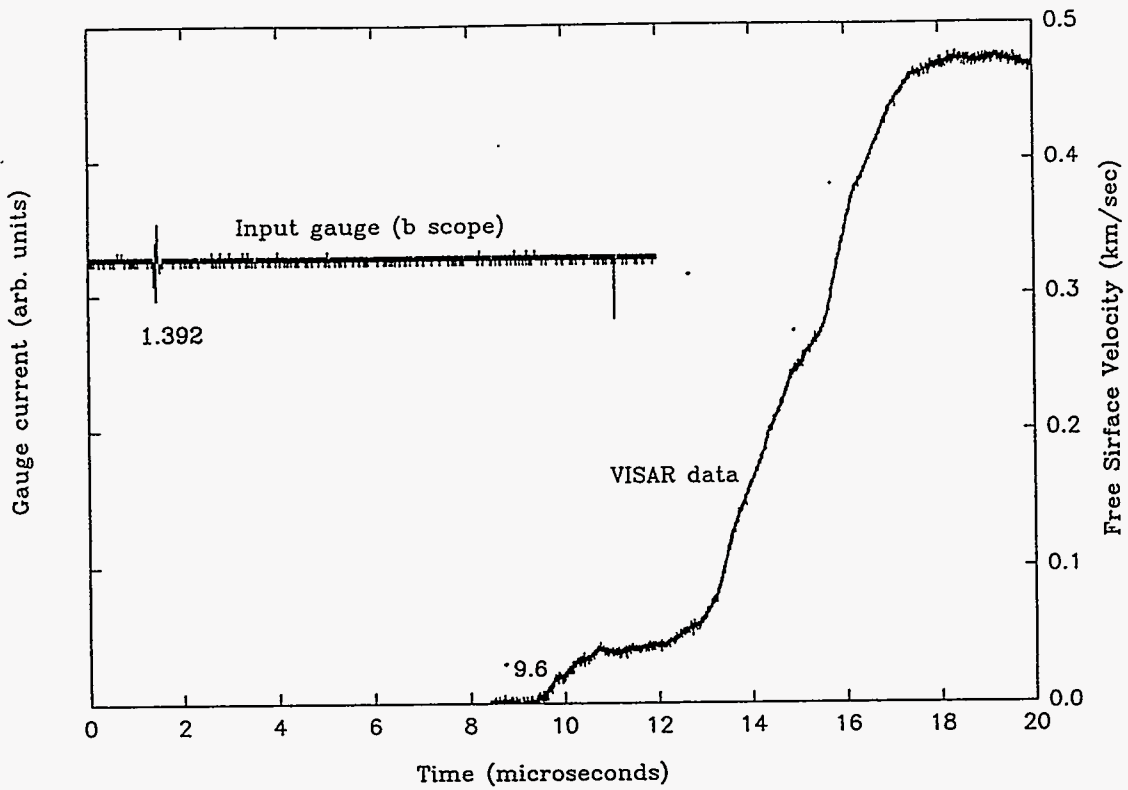
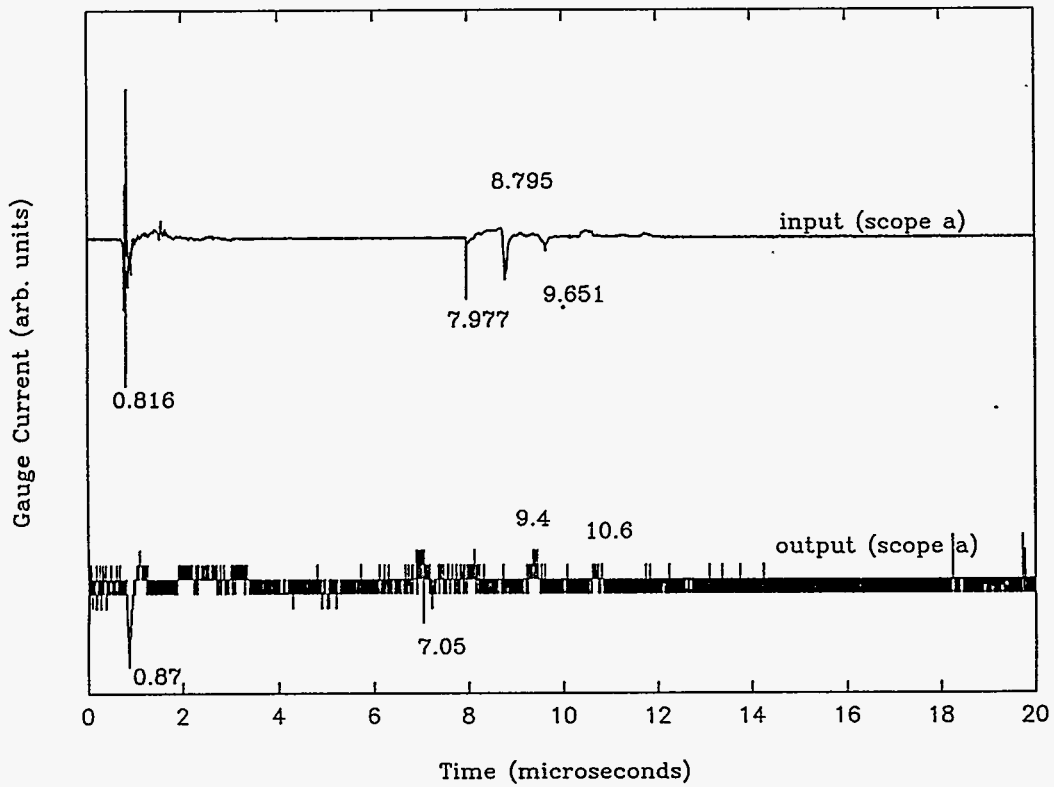Figure C-9. PVDF and VISAR records for test SNW-6. See text for interpretation.
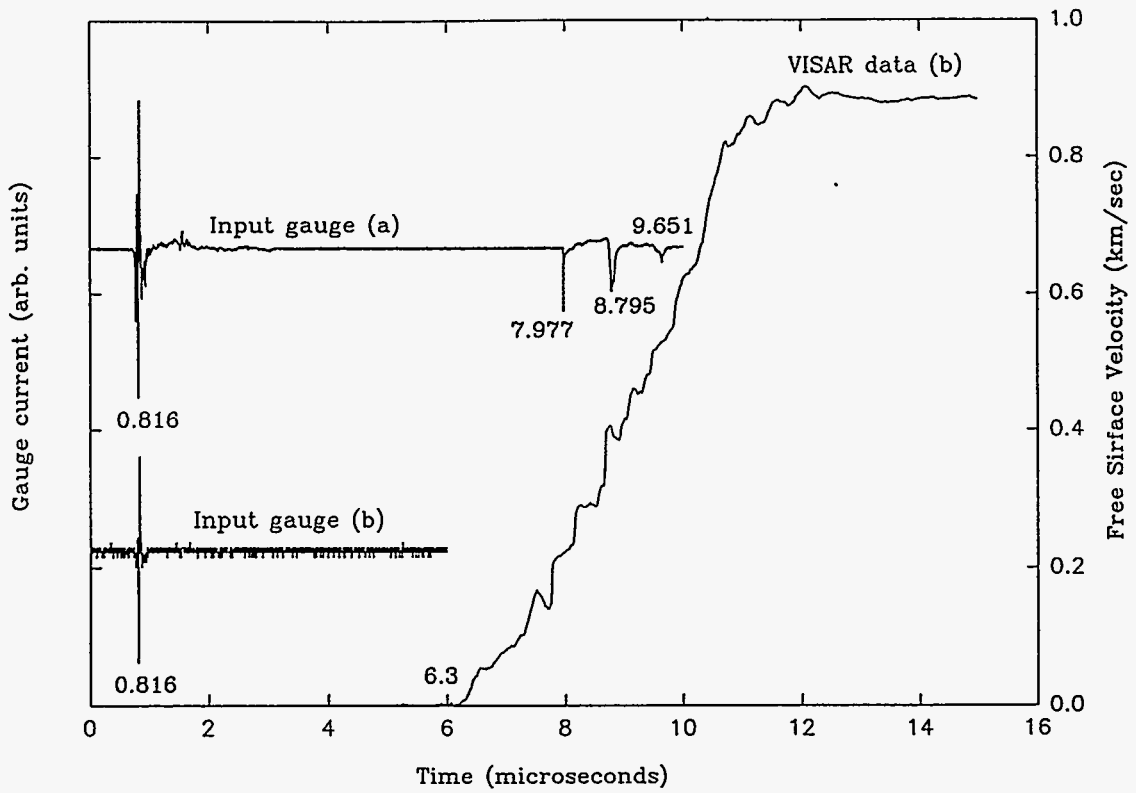
Figure C-10. PVDF and VISAR records for test SNW-7. See text for interpretation.
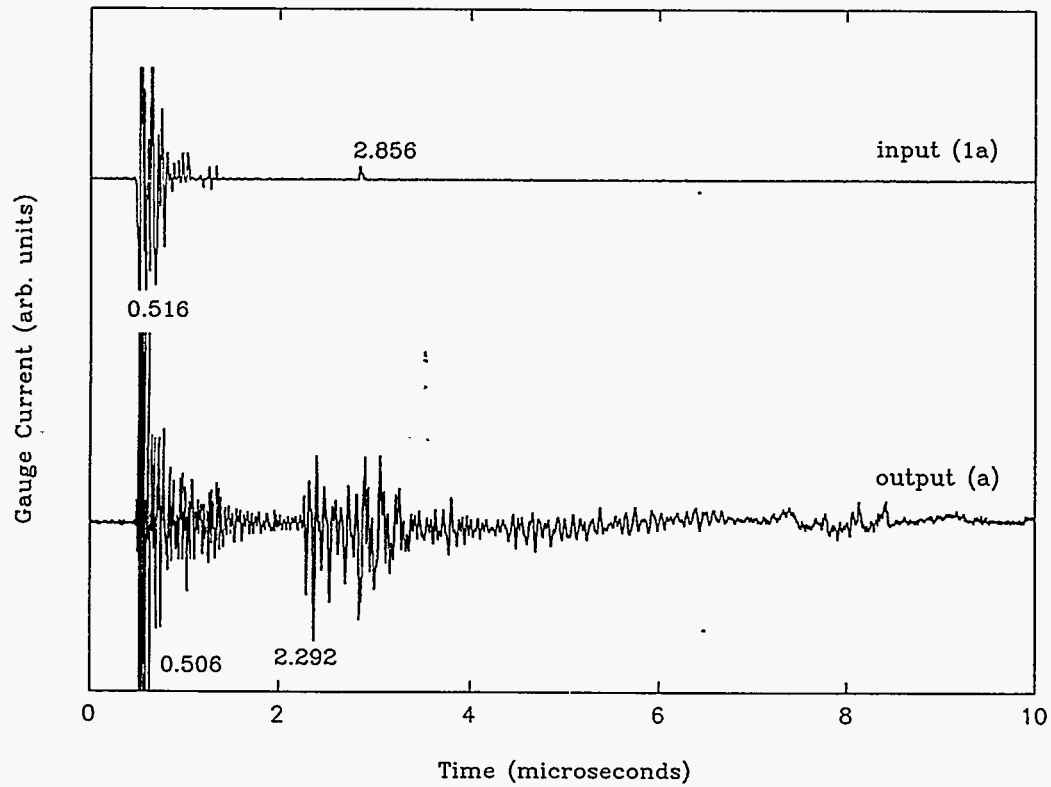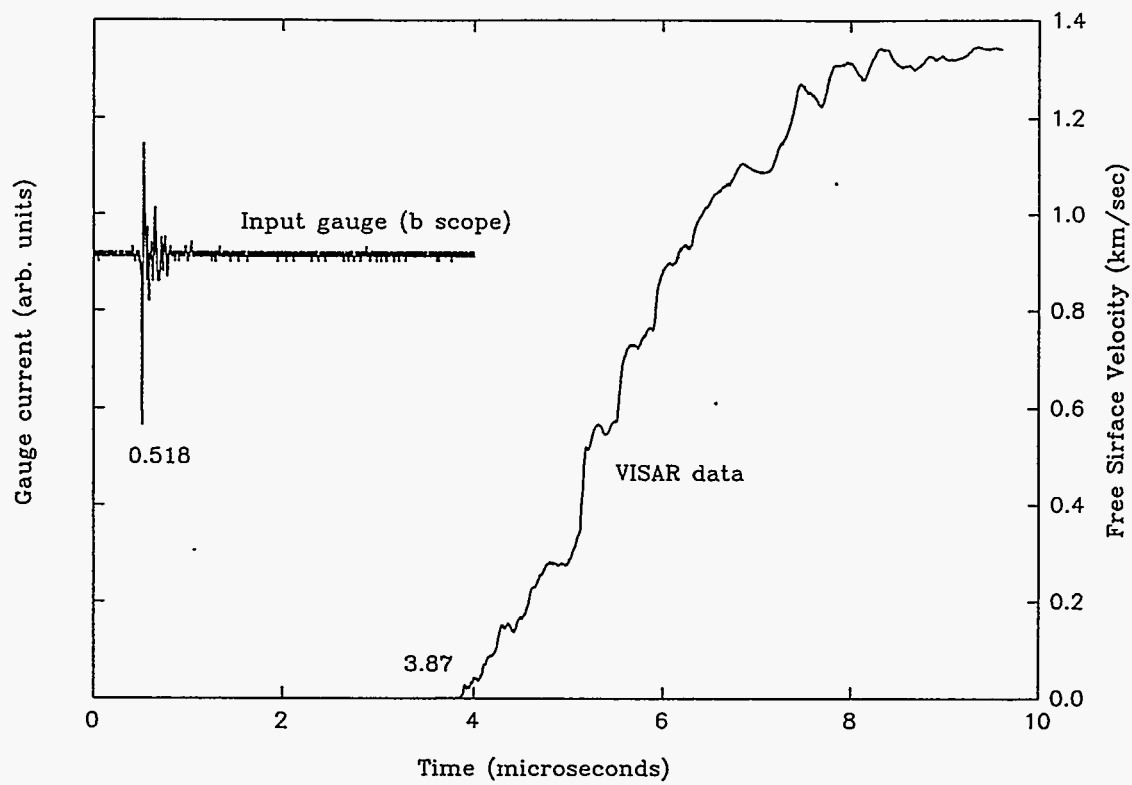
Appendix C

Figure C-11. PVDF and VISAR records for test SNW-8. See text for interpretation.

Figure C-12. PVDF and VISAR records for tests KEL-1,2. See text for interpretation.
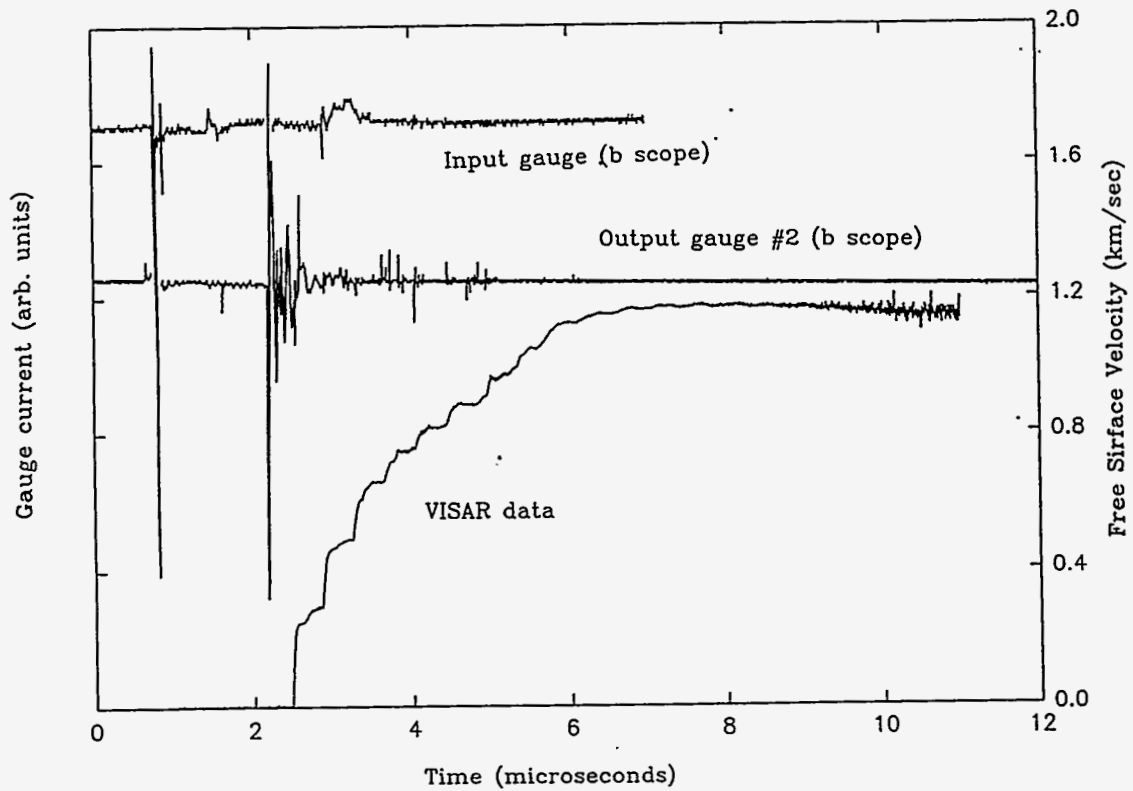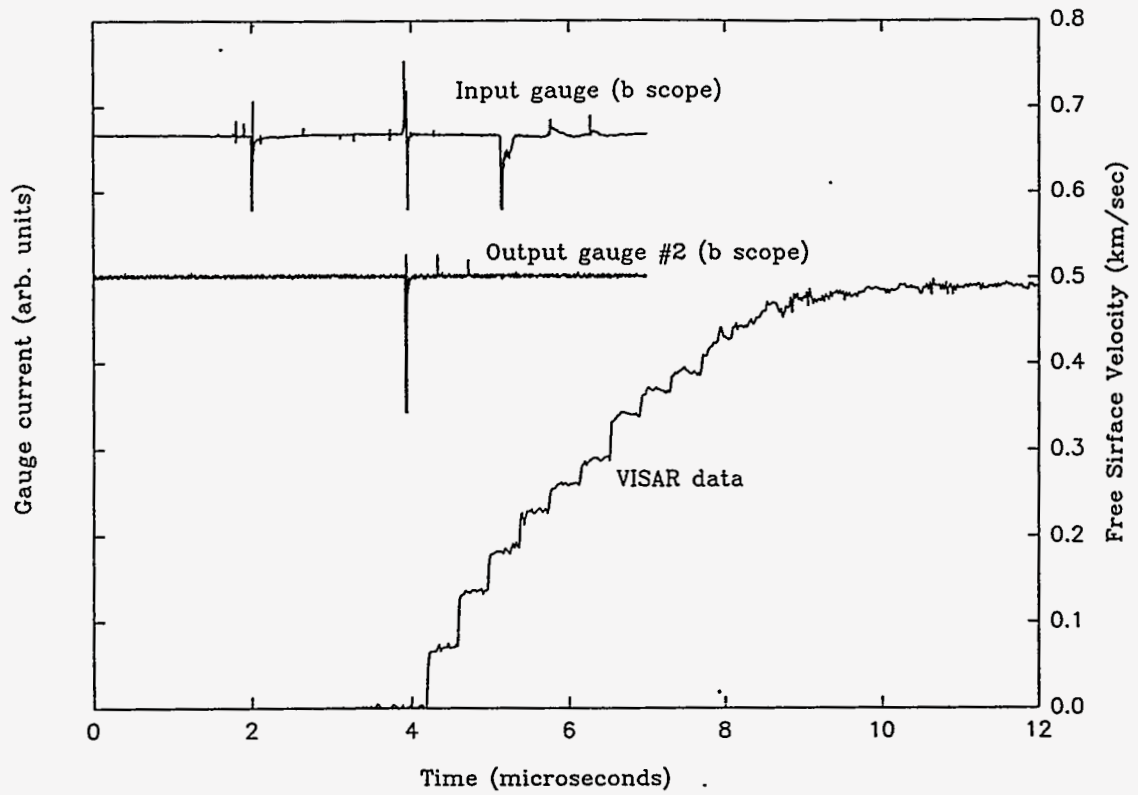
Appendix C

Distribution

External Distribution:

HQ/DNA
6801 Telegraph Road
Alexandria, VA 22310-3398
Attn:
Josephine B. Wood, ISST (2)
Kent Peterson, SPWE
Dave Myers, SPWE
Don Linger, DFTD
Fran Rensvold, DFTD
SSTS (2)

FCDNA/FCTTS
1680 Texas St SE
Kirtland AFB, NM 87117
Attn:
George Baladi, FCTTS
Mike O'Brien, FCTO
George Lu, FCTI
Audrey Martinez, FCTTS
Eric Rinehart, FCTTS
Bob Reinke, FCTTS
Byron Rystvit, FCTTS

CEWES-SD
Waterways Experiment Station
3909 Halls Ferry Road
Vicksburg, MS 39180
Attn:
John Boa
Tony Bombich
Ed Jackson
Joe Zelasko

S-Cubed, A Division of Maxwell
        Laboratories, Inc.
3398 Carmel Mountain Road
San Diego, CA 92121
Attn:
Jim Barthel
Jim Baker
Charles Needham
Steve Peyton

S-Cubed, A Division of Maxwell
        Laboratories, Inc.
3398 Carmel Mountain Road
San Diego, CA 92121
Attn:
Norton Rimer

Logicon R&D Associates
P.O. Box 9377
Albuquerque, NM 87119
Attn:
Gary Ganong
Larry Germain
Barbara Killian

Logicon R&D Associates
6053 West Century Blvd.
Los Angeles, CA 90045
Attn:
Binky Lee

Titan Research and Technology
9410 Topanga Canyon Blvd #104
Chatsworth, CA 91311-5758
Attn:
Anne Cooper
Sheldon Schuster

Lawrence Livermore National Laboratory
P.O. Box 808
Livermore, CA 94550
Attn:
Armand Attia, Mail Stop L-200
Dave Erskine, Mail Stop L-417
Lewis Glenn, Mail Stop L-200
Bill Moran, Mail Stop L-200
Kurt Sinz, Mail Stop L-200

Los Alamos National Laboratory
Los Alamos. NM 87545
Attn:
Thomas Dey, EES-5 M/S F665
Jon Boettger, T-1, M/S B221
James D. Johnson, T-1 M/S B221
James N. Johnson, T-1 M/S B221

SAIC/Pacifica Technology
10260 Campus Point Drive, MS 62
San Diego, CA 92121
Attn:
Martin Fogel
Dan Patch
Mike McKay
Jack Klump

SRI International
333 Ravenswood Ave.
Menlo Park, CA 94025
Attn:
Don Curran
Paul deCarli
Dave Erlich

Thomas J. Ahrens
Seismological Laboratory
Division of Geological and Planetary
    Sciences
California Institute of Technology
Pasadena, CA 91125

Tom Duffy
Carnegie Institution of Washington
Geophysical Laboratory
5251 Broad Brach Road, NW
Washington, D. C. 20015-1305

U. S. Army Corps of Engineers
Cold Regions Research and Engineering
    Laboratory
Fort Wainwright, AK 99703
Attn:
S. A. Barrett
J. B. Johnson
D. J. Solie

U. S. Army Corps of Engineers
Cold Regions Research and Engineering
    Laboratory
72 Lyme Road
Hanover, NH 03755-1290
Attn: G. Blaisdell

Sandia Internal Distribution:

MS 1554	1554	L. J. Weirick
MS 0427	2101	R. McIntosh
MS 0458	5132	J. R. Asay
MS 1033	6111	J. L. Wise
MS 0751	6117	W. R. Wawersik
MS 0437	9162	E. P. Chen
MS 1109	9202	R. J. Pryor
MS 1110	9204	W. J. Camp
MS 1110	9204	J. A. Ang
MS 0318	9215	G. S. Davidson
MS 1111	9221	S. Dosanjh
MS 1110	9222	R. C. Allen
MS 1110	9223	D. Greenberg
MS 1109	9224	A. L. Hale
MS 0441	9225	P. L. Stanton
MS 1111	9226	G. Hefelfinger
MS 0819	9231	J. M. McGlaun
MS 0819	9231	L. C. Chhabildas
MS 0819	9231	D. E. Grady
MS 0820	9232	P. Yarrington
MS 0820	9232	M. Boslough (10)
MS 0820	9232	D. Crawford
MS 0820	9232	A. Farnsworth
MS 0820	9232	M. E. Kipp
MS 0820	9232	F. R. Norwood
MS 0820	9232	W. Reinhart
MS 0439	9234	D. R. Martinez
MS 0820	9322	M. D. Furnish (20)
MS 1160	9322	T. K. Bergstresser
MS 0312	9814	M. J. Forrestal
MS0100	7613-2	Document processing for DOE-OSTI (2)
MS 9018	8523-2	Central Technical Files
MS 0619	12615	Print Media
MS 0899	13414	Technical Library (5)